CERN, January 2009

RD50 Status Report 2008

Radiation hard semiconductor devices for very high luminosity colliders

Centro Nacional de Microelectrónica (IMB-CNM, CSIC), Barcelona, Spain
Juan Pablo Balbuena, Daniela Bassignana, Francesca Campabadal, Sergio Díez, Celeste Fleta, Manuel Lozano, Giulio Pellegrini, Joan Marc Rafí, Miguel Ullán

Dipartimento Interateneo di Fisica & INFN - Bari, Italy
Donato Creanza, Mauro De Palma,Francesca Fedele, Norman Manna

Brookhaven National Laboratory, Upton, NY, USA
Jim Kierstead, Zheng Li

National Institute for Materials Physics, Bucharest - Magurele, Romania
Manuela Buda, Sorina Lazanu, Lucian Pintilie, Ioana Pintilie, Andreia-Ioana Popa

University of Bucharest, Faculty of Physics, Romania
Ionel Lazanu

CERN, Geneva, Switzerland
Paula Collins, Manuel Fahrer, Maurice Glaser, Christian Joram, Katharina Kaska, Alessandro La Rosa, Julien Mekki, Michael Moll[*]*, Nicola Pacifico, Heinz Pernegger*

Universitaet Dortmund, Lehrstuhl Experimentelle Physik IV, Dortmund, Germany
Claus Goessling, Reiner Klingenberg, Jens Weber, Renate Wunstorf

CiS Institut für Mikrosensorik gGmbH, Erfurt, Germany
Ralf Roeder, Dieter Stolze, Hartmut Uebersee

Fermilab, USA
Selcuk Cihangir, Simon Kwan, Leonard Spiegel, Ping Tan

INFN Florence – Department of Energetics, University of Florence, Italy
Mara Bruzzi[†]*, Ettore Focardi, David Menichelli, Monica Scaringella*

University of Freiburg
Michael Breindl, Simon Eckert, Michael Köhler, Susanne Kuehn, Ulrich Parzefall, Liv Wiik

CERN-LHCC-2010-012 / LHCC-SR-003
15/09/2010

[*] Co-spokesperson
[†] Co-spokesperson

Dept. of Physics & Astronomy, Glasgow University, Glasgow, UK
Richard Bates, Andrew Blue, Craig Buttar, Freddie Doherty, Lars Eklund, Alison G Bates, Lina Haddad, Sarah Houston, Grant James, Keith Mathieson, J. Melone, Val OShea, Chris Parkes, David Pennicard

Institute for Experimental Physics, University of Hamburg, Germany
Peter Buhmann, Doris Eckstein, Eckhart Fretwurst, Frank Hönniger, Vladimir Khomenkov, Robert Klanner, Gunnar Lindström, Uwe Pein, Ajay Srivastava

Helsinki Institute of Physics, Helsinki, Finland
Jaakko Härkönen, Katri Lassila-Perini, Panja Luukka, Teppo Mäenpää, Eija Tuominen, Esa Tuovinen

Ioffe Phisico-Technical Institute of Russian Academy of Sciences, St. Petersburg, Russia
Vladimir Eremin, Igor Ilyashenko, Alexandr Ivanov, Evgenia Kalinina, Alexander Lebedev, Nikita Strokan, Elena Verbitskaya

Institute of Physics PAS and Institute of Electronics Technology, Warszawa, Poland
Adam Barcz

Institute of Electronic Materials Technology, Warszawa, Poland
Andrzej Brzozowski, Pawel Kaminski, Roman Kozlowski, Michal Kozubal, Zygmunt Luczynski, Marius Pawlowski, Barbara Surma, Jaroslaw Zelazko

University of Karlsruhe, Institut fuer Experimentelle Kernphysik, Karlsruhe, Germany
Wim de Boer, Alexander Dierlamm, Martin Frey, Frank Hartmann, Valery Zhukov

Institute for Nuclear Research of the Academy of Sciences of Ukraine, Radiation PhysicDepartments
L. Barabash, A. Dolgolenko, A. Groza, A. Karpenko, V. Khivrich, V. Lastovetsky, P. Litovchenko, L. Polivtsev

Department of Physics, Lancaster University, Lancaster, United Kingdom
Duncan Campbell, Alexandre Chilingarov, Harald Fox, Gareth Hughes, Brian Keith Jones, Terence Sloan

Lappeenranta University of Technology, Department of Electrical Engineering, Lappeenranta, Finland
Nino Samadashvili, Tuure Tuuva

Department of Physics, University of Liverpool, United Kingdom
Anthony Affolder, Phillip Allport, Themis Bowcock, Gianluigi Casse, Joost Vossebeld

Jožef Stefan Institute and Department of Physics, University of Ljubljana, Ljubljana, Slovenia
Vladimir Cindro, Irena Dolenc, Gregor Kramberger, Igor Mandic, Marko Mikuž, Marko Zavrtanik, Dejan Zontar

Université catholique de Louvain, Institut de Physique Nucléaire, Louvain-la-Neuve, Belgium
Eduardo Cortina Gil, Ghislain Grégoire, Vincent Lemaitre, Otilia Militaru, Krzysztof Piotrzkowski

Belarusian State University, Minsk
Nikolai Kazuchits, Leonid Makarenko

Groupe de la Physique des Particules, Université de Montreal, Canada
Sébastien Charron, Marie-Helene Genest, Alain Houdayer, Celine Lebel, Claude Leroy

State Scientific Center of Russian Federation, Institute for Theoretical and Experimental Physics, Moscow, Russia
Andrey Aleev, Alexander Golubev,, Eugene Grigoriev, Aleksey Karpov, Alxander Martemianov, Sergey Rogozhkin, Alexandre Zaluzhny

Max-Planck-Institut fuer Physik, Munich, Germany
Ladislav Andricek, Michael Beimforde, Anna Macchiolo, Hans-Günther Moser, Richard Nisius, Rainer Richter

Department of Physics and Astronomy, University of New Mexico, Albuquerque, NM, USA
Igor Gorelov, Martin Hoeferkamp, Jessica Metcalfe, Sally Seidel, Konstantin Toms

The National Institute for Nuclear Physics and High Energy Physics (NIKHEF)
Fred Hartjes, Els Koffeman, Harry van der Graaf, Jan Visschers

University of Oslo, Physics Department/Physical Electronics, Oslo, Norway
Andrej Kuznetsov, Lars Sundnes Løvlie, Edouard Monakhov, Bengt G. Svensson

Dipartimento di Fisica and INFN Sezione di Padova, Padova, Italy
Dario Bisello, Andrea Candelori, Alexei Litovchenko, Devis Pantano, Riccardo Rando

I.N.F.N. and Università di Perugia - Italy
Gian Mario Bilei, Daniele Passeri, Marco Petasecca, Giorgio Umberto Pignatel

Universita` di Pisa and INFN sez. di Pisa, Italy
Jacopo Bernardini, Laura Borrello, Suchandra Dutta, Francesco Fiori, Alberto Messineo

Institute of Physics, Academy of Sciences of the Czech Republic, Praha, Czech Republic
Jan Bohm, Marcela Mikestikova, Jiri Popule, Petr Sicho, Michal Tomasek, Vaclav Vrba

Charles University Prague, Czech Republic
Jan Broz, Zdenek Dolezal, Peter Kodys, Alexej Tsvetkov, Ivan Wilhelm

Czech Technical University in Prague, Czech Republic
Dominik Chren, Tomas Horazdovsky, Zdenek Kohout, Stanislav Pospisil, Michael Solar, Vít Sopko, Bruno Sopko, Josef Uher

Paul Scherrer Institut, Laboratory for Particle Physics, Villigen, Switzerland
Roland Horisberger, Valeria Radicci, Tilman Rohe

Purdue University, USA
Gino Bolla, Daniela Bortoletto, Kim Giolo, Jun Miyamoto, Carsten Rott, Amitava Roy, Ian Shipsey, SeungHee Son

University of Rochester, USA
Regina Demina, Sergey Korjenevski

Santa Cruz Institute for Particle Physics, USA
Alexander Grillo, Hartmut Sadrozinski, Bruce Schumm, Abraham Seiden, Ned Spencer

SINTEF ICT, Blindern, Oslo, Norway
Thor-Erik Hansen

Experimental Particle Physics Group, Syracuse University, Syracuse, USA
Marina Artuso, Alessandra Borgia, Gwenaelle Lefeuvre

Tel Aviv University, Israel
J. Guskov, Sergey Marunko, Arie Ruzin, Tamir Tylchin

Fondazione Bruno Kessler - FBK, Povo, Trento, Italy
Maurizio Boscardin, Gian - Franco Dalla Betta, Paolo Gregori, Claudio Piemonte, Sabina Ronchin, Mario Zen, Nicola Zorzi

IFIC, joint research institute of CSIC and Universitat de Valencia-Estudi General, Valencia, Spain
Carmen Garcia, Carlos Lacasta, Ricardo Marco, Salvador Marti i Garcia, Mercedes Minano, Urmila Soldevila-Serrano

Institute of Materials Science and Applied Research, Vilnius University, Vilnius, Lithuania
Eugenijus Gaubas, Arunas Kadys, Vaidotas Kazukauskas, Stanislavas Sakalauskas, Jurgis Storasta, Juozas Vidmantis Vaitkus

Contents

1. Introduction
2. Executive Summary
3. Defect and Material Characterization
4. Defect Engineering
5. Pad Detector Characterization
6. New Structures
7. Full Detector Systems
8. Resources

1 Introduction

The objective of the CERN RD50 Collaboration is the development of radiation hard semiconductor detectors for very high luminosity colliders, particularly to face the requirements of a possible upgrade scenario of the LHC to a luminosity of $10^{35}cm^{-2}s^{-1}$, corresponding to expected total fluences of fast hadrons above $10^{16}cm^{-2}$ at a bunch-crossing interval of ~25 ns [1, 2]. This document reports the status of research and main results obtained after the sixth year of activity of the collaboration.

Presently, RD50 counts a total of 247 members with 47 participating institutes. This comprises 38 institutes from 17 different countries in West and East Europe, 8 from North America (USA, Canada) and one from middle east (Israel). During the sixth year of activity two workshops and collaboration board meetings have been held to discuss the recent results and co-ordinate the research activities of RD50: Ljubljana, Slovenia, 2-4 June, 2008 and November 10-12, 2008 at CERN. Each workshop has registered a quite high rate of participation, counting an average of 55 participants with about 25 talks. Additionally a dedicated "RD50 workshop on defect analysis in radiation damaged silicon detectors" was held at DESY, Hamburg, 17-19 April focussing on the progress of the RD50 WODEAN project on the investigation of microscopic defects in silicon. More details including all electronic versions of the presentations can be found on the collaboration web-site [3].

Review papers describing the common research activities of the RD50 collaboration have been published in 2003 to 2007 [4-13] and in 2008 [14]. As in the previous years, the research activity of RD50 has been presented in form of oral contributions at several international conferences and workshops [15]:

- 10th International Conference on Instrumentation for Colliding Beam Physics, Budker Institute of Nuclear Physics, Siberian Branch of Russian Academy of Science, Novosibirsk, Russia, February 28 - March 5, 2008 [16]
- 4th NoRHDia Workshop at GSI, Darmstadt, June 2008 [17]
- 1st LHeC Workshop, Divonne les Bains, France, September 1-3, 2008 [18]
- IEEE NSS Special focus Workshop, October 19, 2008 [19]
- Radiation Interaction with Material and its use in Technologies 2008, Kaunas, Lithuania, September 24-27, 2008 [20]
- CMS Upgade Workshop, FNAL, 19-21 November [21]

The scientific organization of RD50 is structured in five research lines as shown in Table 1-1. The management of the research lines is assigned to members of RD50 of proven relevant experience (conveners). In the framework of the research activity of each research line, working groups are active with specific tasks. Each working group is composed of few institutes, which are directly involved in the research program and co-ordinated by an RD50 member. Table 1-1 lists working groups and common activities within each project, with the corresponding co-ordinator.

Besides working groups, common activities were continued or have been started on subjects of common interest. Some of these activities are partially supported with the RD50 common fund. Examples are the common purchase of FZ and MCZ silicon wafers that could only be purchased in big quantities or the expensive processing of a batch of detectors in a 6" processing line with a RD50 common mask.

	Project Convener	Main Research Activity	Working groups and common acitivities
Spokespersons Mara Bruzzi (INFN and Uni. of Florence) and Michael Moll (CERN)	**Defect/Material Characterisation** Bengt G. Svensson Univ. Oslo, Norway	Characterisation of the microscopic properties of standard-, defect engineered and new materials, pre- and post-irradiation.	(1) WODEAN – Workshop on Defect Analysis in Silicon (G.Lindstroem)
	Defect Engineering Eckhart Fretwurst Univ. of Hamburg, Germany	Development and testing of defect engineered silicon: Oxygen enriched FZ (DOFZ), High res. Cz, MCZ, Epitaxial, Si enriched with Oxygen dimers	(1) RD50 wafer procurement (M.Moll)
	Pad Detector Characterisation Gregor Kramberger, Ljubljana Univ., Slovenia	Characterisation of macroscopic properties of heavily irradiated single pad detectors in different operational conditions.	(1) Standardisation of macroscopic measurements (A.Chilingarov) (2) New materials (E.Verbitskaya)
	New Structures Richard Bates Univ. of Glasgow, UK	Development of 3D, semi-3D and thin detectors and study of their pre- and post-irradiation performance.	(1) 3D (M.Boscardin) (2) Semi-3D (Z.Li)
	Full Detector Systems Gianluigi Casse Univ. of Liverpool, UK	- Systematic characterisation of segmented (microstrips, pixels) LHC-like detectors. - Links with LHC experiments	(1) Pixel detectors (D.Bortoletto and T.Rohe) (2) Micron 6” production (H.Sadrozinski, SCIPP)

Table 1-1.: Organisation structure of the research activity in RD50.

In the next section our scientific work is reviewed in an executive summary. This section is followed by five sections describing the status of the research activities of each individual research line. Finally a resource request for 2009 is given.

References for Chapter 1

[1] R&D Proposal - DEVELOPMENT OF RADIATION HARD SEMICONDUCTORDEVICES FOR VERY HIGH LUMINOSITY COLLIDERS, LHCC 2002-003 / P6, 15.2.2002.

[2] RD50 Status Report 2004 – Radiation hard semiconductor devices for very high luminosity colliders, CERN-LHCC-2004-031 and LHCC-RD-005, January 2005

[3] RD50 collaboration web site: http://www.cern.ch/rd50/.

[4] **Michael Moll** on behalf of the CERN RD50 collaboration, “Development of radiation hard sensors for very high luminosity colliders - CERN - RD50 project – “Nucl. Instr. & Meth. in Phys. Res. A 511 (2003) 97-105.

[5] **Mara Bruzzi** on behalf of the CERN RD50 Collaboration, “Material Engineering for the Development of Ultra-Radiation Hard Semiconductor Detectors”, Nucl. Instrum. & Meth. A 518, 1-2, 2004, 336-337.

[6] **Panja Luukka** on behalf of the CERN RD50 Collaboratin “Status of Defect Engineering Activity of the RD50 Collaboration” Nucl. Instrum. & Meth. A 530, 1-2, 2004, 152-157.

[7] **Michael Moll et al. (RD50 Collaboration)**, "Development of radiation tolerant semiconductor detectors for the Super-LHC", NIMA 546 , 99-107 (2005).

[8] **M. Bruzzi et al. (RD50 Collaboration)**; "Radiation-hard semiconductor detectors for SuperLHC"; NIMA, 541, 189-201 (2005).

[9] **F.Fretwurst et al. (RD50 Collaboration)**, "Recent advancements in the development of radiation hard semiconductor detectors for S-LHC"; NIMA 552, 7-19 (2005).

[10] **Andrea Candelori** on behalf of the CERN RD50 collaboration, "Radiation-hard detectors for very high luminosity colliders"; NIMA, 560, 103-107, (2006).

[11] **Michael Moll** on behalf of the CERN RD50 collaboration, "Radiation tolerant semiconductor sensors for tracking detectors"; Michael Moll; NIMA, 565, 202-211, (2006).
[12] **Panja Luukka,** "Recent progress of CERN RD50 Collaboration";; Trans. Nonferrous Met. Soc. China, 16, s133-s136, (2006).
[13] **Gregor Kramberger,** "Recent results from CERN RD50 collaboration"; NIMA, 583, 49-57, (2007).
[14] **David Menichelli**, "Recent developments of the CERN RD50 collaboration"; David Menichelli; NIMA, 596, 48-52, (2008).
[15] Electronic versions of the talks are available on the RD50 www-page under http://www.cern.ch/rd50/doc/
[16] Gianluigi Casse, Liverpool, "Overview of the recent activities of the RD50 collaboration on radiation hardening of semiconductor detectors for the SLHC", 10th International Conference on Instrumentation for Colliding Beam Physics, Budker Institute of Nuclear Physics, Siberian Branch of Russian Academy of Science, Novosibirsk, Russia, February 28 - March 5, 2008
[17] Michael Moll, CERN, "Radiation Tolerant Silicon Sensors - Some recent RD50 results -", 4th NoRHDia Workshop at GSI, Darmstadt, June 2008
[18] Michael Moll, CERN, "Recent RD50 Developments on Radiation Tolerant Silicon Sensors",1st LHeC Workshop, Divonne les Bains, France, September 1-3, 2008
[19] Mara Bruzzi and Michael Moll (Workshop chairs), Special Focus Workshop "Detector Developments for the SLHC", Sunday 19 October in framework of IEEE NSS MIC 2008 conference, Dresden
[20] Juozas Vaitkus," Development of radiation tolerant silicon detectors for the superLHC and defect properties in highly irradiated Si (CERN RD50 collaboration).", Vilnius, Lithuania, Radiation Interaction with Material and its use in Technologies, Kaunas, Lithuania, September 24-27, 2008
[21] Panja Luukka, Helsinki Institute of Physics, CMS Upgade Workshop, FNAL, 19-21 November 2008

2 Executive Summary

2.1 Defect and Material Characterization (DMC)

- The DMC core activities have been performed since 2006 in a closely coordinated manner through the *WODEAN (Workshop on Defect Analysis)* network, representing an RD50 subgroup. In total three Workshops dedicated only to Defect and Material Characterization only have been taken place. Only the key findings of 2008 are reported in this status report while further results can be found on the RD50/Wodean websites.

- *Cluster related defects* have been extensively studied by TSC and DLTS. Irradiation experiments with 1 MeV neutrons and 23 GeV protons have revealed that particular cluster related defects have a direct impact on the device characteristics at operating temperature. The defect centers H(116K), H(140K) and H(152K) were shown to be acceptor type levels in the lower part of the band gap. Their defect parameters (zero field emission rates and position in band gap) were precisely measured. It was found that these defects are responsible for the reverse annealing. The cluster related defects E4, E5 and E205 were found to be responsible for a part of the leakage current observed after irradiation. A surprising feature of the E4 and E5 defects was detected. After the thermal annealing of the defects at elevated temperatures an injection of 1A in forward bias conditions reproduced the defects. In a following isothermal annealing at 80ºC the defects disappeared again and could then be reproduced again by an injection of 1A. They thus show a bistable behavior that can be exploited to perform more detailed studies on the defect parameters and their impact on the detector leakage current.

- *Photo-induced transient spectroscopy (PITS)* measurements have been performed on neutron irradiated FZ and MCZ silicon sensors. Contrary to the DLTS method, measurements can be performed with this method also after exposing the samples to very high irradiation levels. Defect spectra were obtained on samples irradiated up to 3×10^{16} n/cm^2. Several defect levels could be identified and their annealing behavior was studied in an isochronal annealing study up to 240ºC.

- *Photoconductivity spectra* were obtained on MCZ and FZ sensors after exposure to neutron irradiation and in a consecutive isochronal annealing study. Optical activation energies for either the excitation of free electrons from the filled deep center or the generation of free holes by excitation of electrons from the valence band to the empty local defect level were obtained. The most shallow level observed was 0.5 eV and the deepest about 1.11 eV.

- *Recombination and generation lifetime measurements* were performed on neutron irradiated MCZ silicon sensors. It was found that the recombination lifetime decreases nearly linearly with the increasing neutron fluence.

2.2 Defect Engineering (DE)

- *Epitaxial silicon (EPI):* New epitaxial silicon layers of 100 and 150 μm thickness on 100 mm wafers were grown and transformed into detector structures using different processing technologies. Standard processes (EPI) and new processing technologies (EPI-DO) allowing to modify the oxygen content in the epitaxial layers were used. With a special SIMS

(Secondary Ion Emission Spectroscopy) technique the oxygen depth profiles of the epitaxial detectors (EPI and EPI-DO) were investigated in detail. The results can now on the one hand be used to tailor the oxygen profile in the EPI-DO material according to our needs and on the other hands to get a deeper understanding on the impact of oxygen on the defect kinetics after irradiation.

- The *formation of shallow donors* in EPI- and MCZ- silicon was investigated using the *Thermally Stimulated Crurrent* (TSC) method. It is demonstrated that the shallow donors (denoted bistable donors BD) are generated in the EPI and EPI-DO materials and in a much lower concentration also in the used MCZ material. The donor character of the BD center could be proved by measuring the Poole-Frenkel effect on the two observed transitions $BD^{(0/++)}$ and $BD^{(+/++)}$. Furthermore, a detailed investigation on the E(30K) defect revealed that also this defect has a donor character and thus contributes positive space charge to the effective doping concentration. The increase of the concentration of BD and E(30K) in an isothermal annealing at 80ºC leads to the conclusion that these defects might be responsible for the so-called short term annealing.

- *Hydrogenation of silicon:* As hydrogen is more difficult to be detected by the SIMS method than deuterium, in a first 'hydrogenation' experiment deuterium was used. 710 keV deuterons were implanted into FZ silicon and the concentration depth profile was measured using the SIMS method directly after implantation as well as after several annealing steps. It could be shown that the out diffusion of deuterium is limited when a nitride layer is deposed on the silicon surface. In a second experiment 5.5 MeV protons were implanted into EPI detectors from the substrate layer side. The energy was chosen to implant the hydrogen up to about 10 μm away from the substrate epilayer interface. During the following annealing at 500 to 600ºC part of the hydrogen could be diffused into the epi layer. However, the radiation damage produced by the implantation and annealing procedure had changed the electrical properties of the diodes beyond an acceptable level. Therefore, one has to search for other techniques avoiding any radiation damage or reducing the damage as much as possible.

- *Pre-irradiated silicon:* Neutron Transmutation Doped (NTD) as well as pre-irradiated FZ silicon diodes were investigated with respect to their charge collection efficiency (CCE) loss during irradiation with neutrons. It was demonstrated that the charge loss for the NTD and pre-irradiated diodes is slightly less than the one observed for standard FZ silicon diodes after exposure to the same neutron fluence.

2.3 Pad Detector Characterization (PDC)

- *Review of damage parameters:* A detailed review of damage parameters obtained for the various silicon diode materials used in RD50 has been performed and is presented in this status report. Following the so-called 'Hamburg model' damage parameters for the effective doping concentration and the leakage current have been evaluated (see section 5.1). Parameterizations for effective trapping times are given in section 5.2. and Charge Collection measurements (CC) are summarized in section 5.3. Data are provided for neutron, proton and partly also for pion irradiations over a wide fluence range.

- *Mixed irradiations:* Detectors at LHC and SLHC will be exposed to different mixtures of fast charged hadrons and neutrons. It was previously shown that charged hadron and neutron irradiation can lead to significantly different detector degradations in some silicon materials (e.g. MCZ silicon). Consequently the question rises if damage produced by two different irradiation particles simply adds together or if 'mixed' irradiations lead to new unexpected effects. Mixed irradiations performed with protons, pions and neutrons demonstrate that for the radiation induced leakage current the damage can be regarded as additive and following the 1-MeV neutron equivalent fluence. The radiation induced change of the effective doping

concentration was also found to be additive. For the particular case of MCZ silicon this means that for example proton or pion induced positive space charge is compensated by the negative space charge produced during neutron irradiation.

2.4 New Structures (NS)

- *Thin planar detectors* were produced in form of segmented sensors on epitaxial and SOI wafers. Test structures to prove the isolation features on the n-side of the wafer, using homogeneous and moderate p-spray techniques, have been produced and irradiated. The interstrip capacitance and resistance remain acceptable up to the tested dose of 1MRad.

- The characterization of *single type column 3D detectors* produced by FBK has been concluded with a testbeam at CERN. The incomplete charge collection due to ballistic deficit was demonstrated and the detection efficiency as function of position of the incident beam across the detectors surface was mapped.

- *Double-sided 3D devices* have been fabricated by both FBK and CNM-IMB. Results from those from CNM-IMB operating as pixel and strip sensors have been obtained, including charge collection after irradiation. A testbeam has taken place with double-sided detectors from both FBK and CNM-IMB in 2008 and the analysis is ongoing.

- Extensive *simulation work on 3D sensors* has been performed in order to better understand the electric field distribution and charge collection as well as to optimize the detector geometry.

2.5 Full detector Systems (FDS)

- The Alibava readout system which is based on the 40 MHz LHC-Beetle analogue chip is ready for distribution among the RD50 member institutes. First results obtained with this system are already given in this report.

- Several results of charge collection efficiency after very high fluences of proton and neutron irradiations have been shown, bringing the CCE measurements with segmented planar silicon sensors over the remarkable limit of $2x10^{16}$ n_{eq} cm^{-2}.

- Several measurements on important parameters to qualify the performances of irradiated detectors, like interstrip capacitances and resistance after irradiation, have been measured. These parameters are especially important for the n-side readout detectors in order to determine if the inter-electrode isolation (p-spray, p-stop or combination of both) is sufficient to guarantee proper operations of the segmented detectors.

- Extensive studies of segmented n- and p-type detectors processed on both FZ and MCZ wafers are reported. A very good result was obtained with segmented n-type MCz detectors with n-side readout, however further tests are required in 2009 to consolidate these findings.

- Thin sensors of 140 μm showed significant advantages against 300 μm thick sensors at extreme fluences of $1x10^{16}$ n_{eq} cm^{-2}.

- Correlation studies on neutron irradiated segmented and pad sensors between the depletion voltage obtained from C-V measurements and from CCE measurements showed that the C-V method can be used to give an estimate of the collected charge (if the trapping is estimated correctly).

3 Defect and Material Characterization

3.1 Introduction

During 2008 the activity in the DMC research line has been mainly focused on cluster related defects which are considered to be responsible not only for the reverse current but also for the long term development of the effective doping concentration and charge carrier trapping in silicon particle detectors. Especially charge carrier trapping is considered to be the most crucial limitation for applications of silicon detectors in the innermost tracking area of all experiments at S-LHC but the identity of the main responsible defects is so far not clarified.

Since the fall of 2006 the DMC core activities are performed in a closely coordinated manner through the network WODEAN (WOrkshop on DEfect ANalysis), a subgroup inside RD50. The transparencies of all three workshops can be found under http://rd50.web.cern.ch/rd50/ (WODEAN (Defects)).

In this report recent results on cluster related defects investigated by DLTS, TSC, PITS and photoconductivity will be summarized as well as new studies on lifetime measurements.

3.2 Cluster related defects studied by TSC and DLTS

Irradiation experiments with 1 MeV neutrons and 23 GeV protons have revealed that several cluster related defects are created having a direct impact on the device characteristics at operating temperature. These defects are discussed below.

i) _H(116K), H(140K) and H(152K)_ centers are traps for holes with acceptor type levels in the lower part of the band gap [1]. As coulombic centers, their emission rates depend on the local electric field. The parameters for the zero field emission rates as reported in Ref. [1] are: $\sigma_p^{116K} = 4\cdot10^{-14}$ cm^2 and ΔH_a^{116K} = 0.33eV, $\sigma_p^{140K} = 2.5\cdot10^{-15}$ cm^2 and ΔH_a^{140K} = 0.36eV and $\sigma_p^{152K} = 2.3\cdot10^{-14}$ cm^2 and ΔH_a^{152K} = 0.42eV. These centers were first detected after irradiation with 1 MeV neutrons by means of the TSC technique [1] and later after irradiation with 23 GeV protons (see Fig. 3.2.1). The TSC signals resulting from these deep acceptors centers are increasing with annealing time. As they are located in the lower part of the gap, these hole traps contribute fully with negative space charge to the effective doping concentration N_{eff} and are responsible for the long term annealing as seen by the increase of the depletion voltage (so called *"reverse annealing"*).

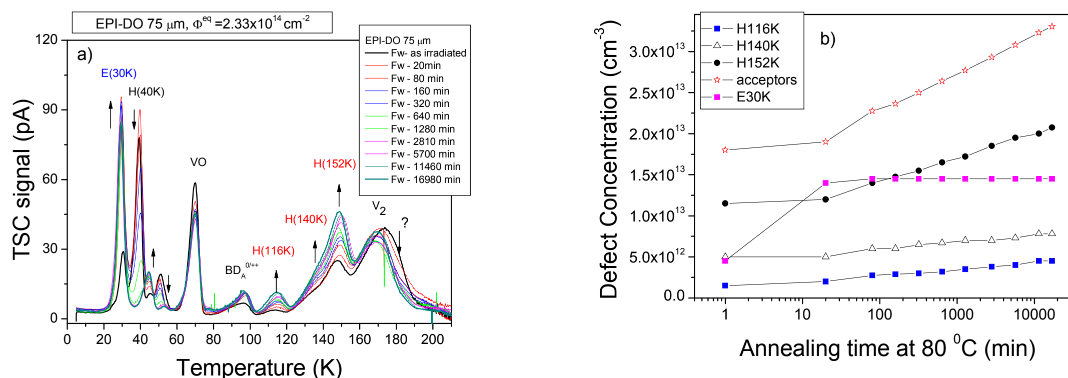

Fig. 3.2.1 EPI-DO diode, after irradiation with 23 GeV protons, fluence $\phi_{eq} = 2.33\cdot10^{14}$ cm^{-2}: a) TSC spectra corresponding to a forward injection at 5K, and different annealing time at 80^{0}C; b) Concentration of the defects H(116K), H(140K), H(152K) and E(30K) versus annealing time at 80^{0}C.

ii) _E(30K) defect_ is acting as a trap for electrons. It is generated mainly during the first 20 min at 80^{0}C after irradiation (see Figs. 3.2.1) and in a much higher concentration after irradiation with protons than

with neutrons [2]. The TSC investigations have shown that it is a defect with enhanced-field-emission described by the Poole-Frenkel effect (see Fig.3.2.2) indicating thus that it has a donor level in the upper part of the gap. The parameters for the zero field emission rate describing the experimental results are: $\sigma_n^{30K} = 2.3\cdot10^{-14}$ cm^2 and $\Delta H_a^{30K} = 0.1$eV from the conduction band. This center contributes in its full concentration with positive space charge to N_{eff} and consequently is partly responsible for the so called *"beneficial annealing"* effect.

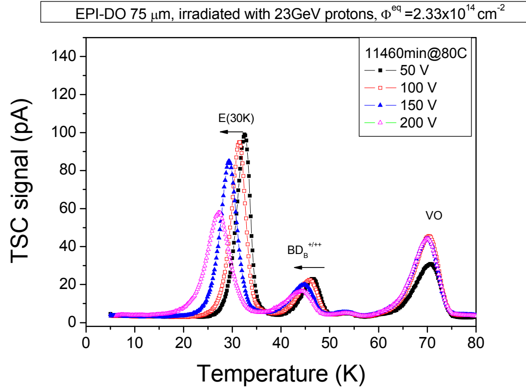

Fig. 3.2.2 Temperature shift of the E(30K) peak with reverse bias (Poole-Frenkel effect) indicating the donor activity of the E(30K) center.

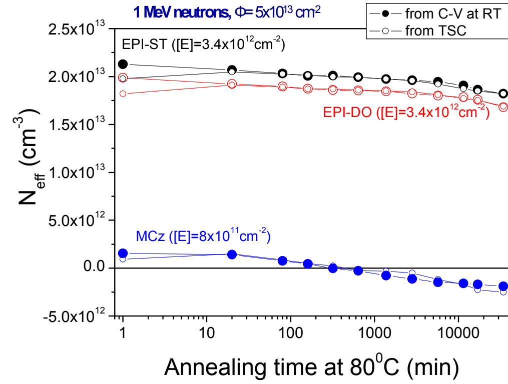

Fig. 3.2.3 N_{eff} determined at 293K from C-V measurements (filled symbols) and calculated change of N_{eff} due to the space charge introduced by H(116K), H(140K), H(152K), BD, E(30K) and E(VP) centers (open symbols).

The TSC defect investigations were used to predict the annealing effects of N_{eff} and to compare the results with values determined from C-V measurements at room temperature (see e.g. Fig.3.3). The evolution of defect concentrations with time after irradiation describes fully the annealing of N_{eff} as determined from C-V measurements. In the calculations also the VP complex (the E center) was considered and the estimated values are given in Fig.3.2.3. The space charge sign inversion (SCSI) effect during annealing is also nicely described by the "microscopic" findings, as can be seen in case of MCz diodes. It is for the first time when a direct correlation between the annealing behavior of hadron irradiated silicon diodes as seen at "macroscopic scale" can be understood by the "microscopically" investigated formation of defects.

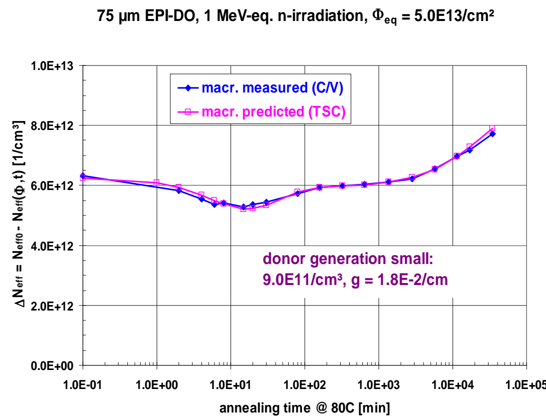

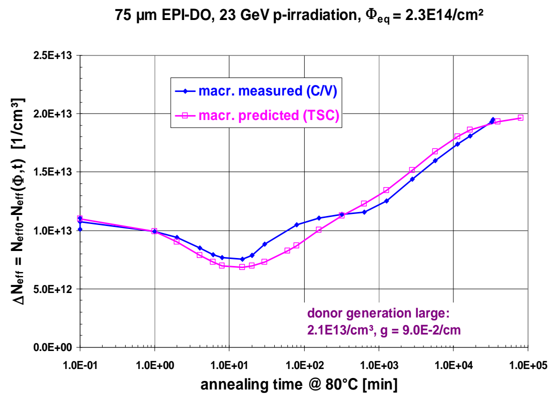

Fig. 3.2.4 Isothermal annealing of ΔN_{eff} determined at 293K from C-V measurements (filled symbols) and calculated change of ΔN_{eff} due to the space charge introduced by H(116K), H(140K), H(152K), BD, E(30K) and E(VP) centers (open symbols) in EPI-DO diodes after irradiation with: left) 1 MeV neutrons, $\phi_{eq} = 5\cdot10^{13}$ cm^{-2}; right) 23 GeV protons, $\phi_{eq} = 2.33\cdot10^{14}$ cm^{-2}.

Similar correlations were also observed after 23 GeV proton irradiations. The results, in terms of the N_{eff} change due to irradiation and subsequent annealing at 80^{0}C, are presented in Fig. 3.2.4 for EPI-DO diodes irradiated with neutrons and protons. The most obvious difference between the two types of irradiation is given by the introduction rate of donors. The donor generation rate after neutron irradiation is g = 0.018 cm $^{-1}$ while after proton irradiation a value of 0.09 cm^{-1} was obtained. This

difference is mainly due to the E(30K) defect, generated with much larger concentration after proton irradiation than after neutron irradiation.

iii) The cluster related defect levels E4 and E5 [3] are generated during irradiation and detectable with DLTS and TSC after injecting electrons into the diode volume. One example of the obtained DLTS spectra is shown in Fig. 3.2.5. While the levels E4 and E5 decrease even at moderate temperatures and vanish after annealing of 30 minutes at 100 °C the defect complex E205a is more stable and anneals in the temperature range between 100 °C and 200 °C.

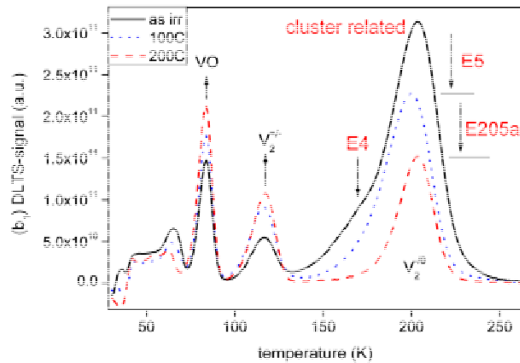

Fig. 3.2.5 DLTS spectra of a neutron irradiated MCz-diode after electron injection. The annealing steps were performed for 30 minutes each. E4 and E5 are not detectable after 100°C while E205a anneals in the temperature range of 100 °C to 200 °C.

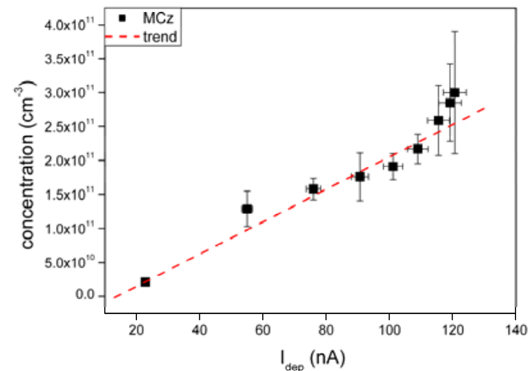

Fig. 3.2.6 Correlation of defect concentrations and leakage current of a neutron irradiated MCz-sample. The values were obtained during the isochronal annealing in steps of 20 °C and normalized to the starting values directly after irradiation. The concentrations of the defect levels E4, E5 and E205a were taken into account.

The concentrations of the cluster related defects cannot be obtained directly from the DLTS spectra, due to their overlap with the singly charged state of the divacancy. Therefore, difference spectra during the annealing process were analyzed. Fig. 3.2.6 shows the correlation of the defect concentration with the leakage current, taken during the isochronal annealing in 20 °C steps with the annealing time of 30 minutes each. The defects which were taken into account are the levels E4, E5 and E205a. Both the concentrations of defects as well as the leakage current were normalized to the starting values, taken directly after irradiation. It is clearly seen, that the leakage current and the cluster related defect concentrations are correlated. The dashed line indicates a possible linear correlation.

Recently Fleming et. al. found the bistability of the cluster related defect levels E4 and E5 [4]. This bistability can be used to track cluster related defects to higher temperatures. In the past it was seen that these defects anneal out after 120 minutes at 80°C. Now they can be tracked to annealing temperatures of more than 300°C. It is possible to recover their concentration by injecting a high forward current into the diode.

Measurements of MCz- material after the annealing at 200°C confirm the correlation between cluster related defects and the reverse current. Fig. 3.2.7 shows the recovery of the reverse current and the concentration of the defect levels E4 and E5 after the injection of 1A forward current and the subsequent annealing at 80°C after the injection, respectively.

Furthermore the bistability of E4 and E5 was used to follow the annealing of cluster related defects to high annealing temperatures in order to find a possible relation to vacancy or interstitial related defects. Fig. 3.2.8 presents the results of the measurements on oxygen rich MCz material. We observe the simultaneous annealing out of V_2 and the cluster related defects. The similarity in the annealing behavior between E4, E5 and the V_2 supports the assumption that E4 and E5 are vacancy related defects, both located in the disordered region. Additional measurements have been performed on oxygen lean FZ and EPI-ST-samples. The study has not been finished yet, but shows a similar trend.

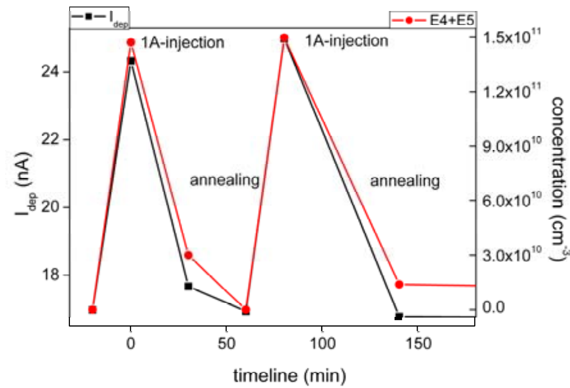

Fig. 3.2.7 Comparison of the change in the reverse current with the concentration of E4 and E5 due to the bistable effect. Data were taken during two injections of 1 A forward current and the subsequent annealing at 80 °C at the same isochronal annealing step of 200 °C. The used material was MCz 300 µm after irradiation with reactor neutrons and a fluence of $3x10^{11}$ n/cm^2.

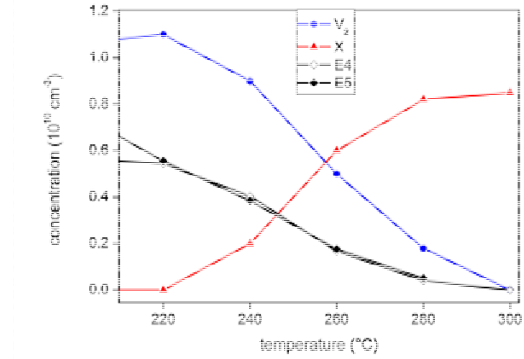

Fig. 3.2.8 Annealing behaviour of E4 and E5 at high temperatures compared to divacancy and X defect for a MCz –sample irradiated with reactor neutrons and a fluence of $3x10^{11}$ n/cm^2.

The formation of all these cluster related defects is not affected by the oxygen content or Si growth procedure suggesting that they are complexes of multi-vacancies and/or multi-interstitials located inside extended disordered regions.

3.3 Neutron induced defects studied by PITS

We show the results obtained by the photo-induced transient spectroscopy PITS for the following materials:

- Okmetic MCz <100> silicon wafers, *n*-type, 1 kΩcm, 300 µm thick, [O] = 5.0×10^{17} cm^{-3}, [C] = ≤ 5×10^{15} cm^{-3}
- FZ <111> silicon wafers, #ST-Wf03, *n*-type, 2 kΩcm, 290 µm thick, [O] = $(0.5\text{-}1)\times10^{16}$ cm^{-3} [C] = ≤ 1.0×10^{15} cm^{-3}

The neutron irradiations were performed at the TRIGA reactor in Ljubljana. The fluences under investigation are: 1×10^{13}, 1×10^{14}, 3×10^{14}, 1×10^{15}, 3×10^{15}, 1×10^{16}, and 3×10^{16} cm^{-2}

Apart from the PITS spectra, we show the temperature dependence of the electron mobility and lifetime product ($\mu\times\tau$) for FZ and MCz samples directly after neutron irradiation (Fig. 3.3.1-3.3.2)and after isochronal annealing at temperatures 80, 160 and 240 ^{0}C (see Fig. 3.3.3-3.3.4). The $\mu\times\tau$ product was determined from the measurement of the amplitude of the photocurrent pulse as function of temperature. The studies show how the high neutron fluence results in a reduction of the lifetime and an increase of the trap concentrations. The amplitudes of the spectra are normalized with respect of the mobility and lifetime product, so the defect concentration is proportional to the height of the peak in the PITS spectrum. The trap parameters determined from the Arrhenius plots are given in Table 3.3.1.

The measurements revealed 8 traps with activation energies ranging from 25 to 510 meV. The shallow traps TSD (25 meV) and T3 (80 meV) are observed only in MCz-Si. Both for the FZ-Si and MCz-Si samples irradiated with a neutron fluence of 1×10^{16} cm^{-3}, significant changes in the traps concentrations are seen after annealing at 160 ^{o}C. However, the temperature dependences of the $\mu\times\tau$ product after annealing at 160 ^{o}C for FZ and MCz materials are significantly different. This effect is probably due to much higher oxygen concentration in the MCz samples. In the case of the FZ material, after annealing at 240 ^{o}C, the concentration of the shallow trap T2 (60 meV) is approximately equal to the concentration of deep trap T7 (510 meV). For the MCz material, after annealing at 240 ^{o}C, the concentration of the shallow trap T3 (80 meV) is by the order of magnitude higher than the concentration of deep trap T7 (510 meV).

Table 3.3.1 Parameters of defect centers obtained from the PITS studies for MCz Si and FZ Si irradiated with high fluences of 1-MeV neutrons. * E_a and A - the activation energy and pre-exponential factor in the Arrhenius formula $e_T=AT^2exp(-E_a/kT)$

Trap label	E_a^*(meV)	A^* ($K^{-2}s^{-1}$)	T (K) at e_T= 3000 s^{-1}	Tentative identification
TSD	25±2	(4-7)×10^3	~45	shallow donor
T1	40±5	(1-2)×10^3	~65	interstitial aggregate (I_4) ?
T2	60±5	(3-5)×10^3	~80	interstitial aggregate (I_3) ?
T3	80±7	(6-9)×10^3	~90	interstitial aggregate (I_2) ?
T4	330±15	(2-7)×10^6	~210	IO_i
T5	410±20	(1-3)×10^7	~250	$V_2^{-/0}$
T6	430±20	(5-7)×10^8	~275	$V_2O^{-/0}$
T7	510±30	(3-8)×10^7	~295	vacancy aggregate (V_3, V_4, V_5)

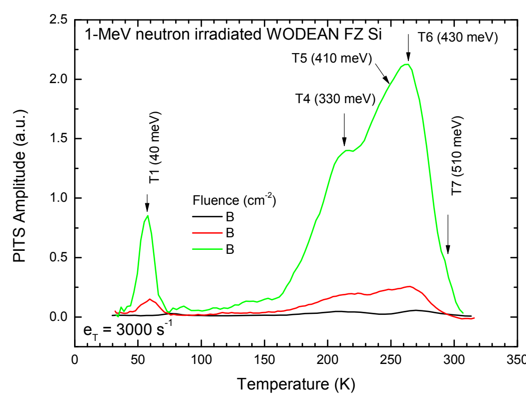

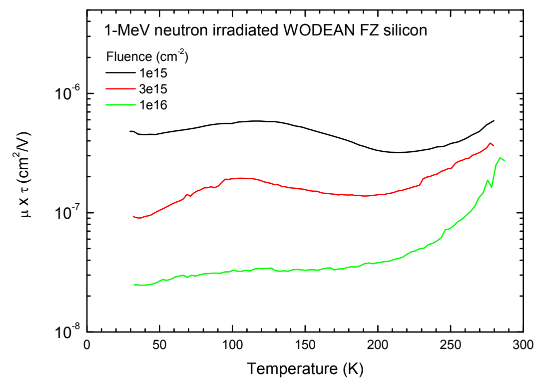

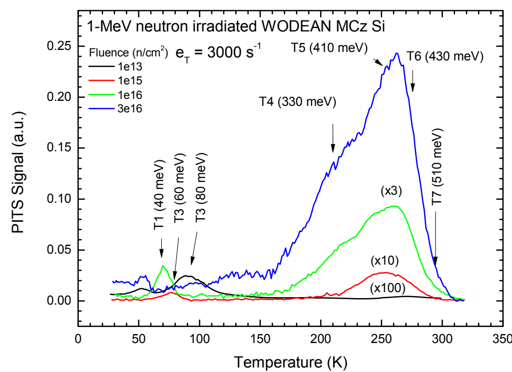

Fig. 3.3.1 PITS spectra obtained for FZ (top) and MCz (bottom) Si samples for different fluences. Emission rate window e_T = 3000 s^{-1}.

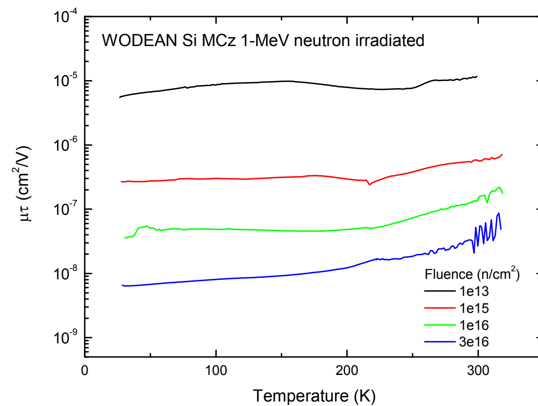

Fig. 3.3.2 Temperature dependence of charge carrier mobility-lifetime product for FZ (top) and MCz (bottom) samples irradiated to various fluences.

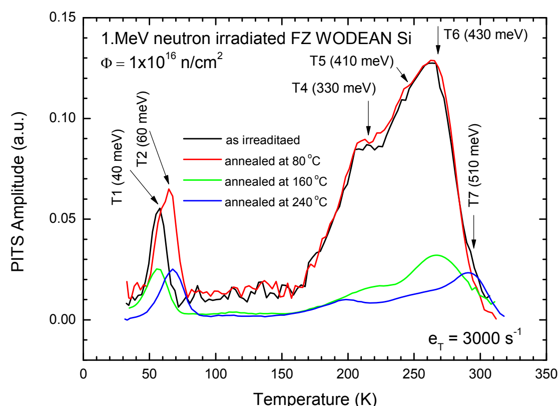

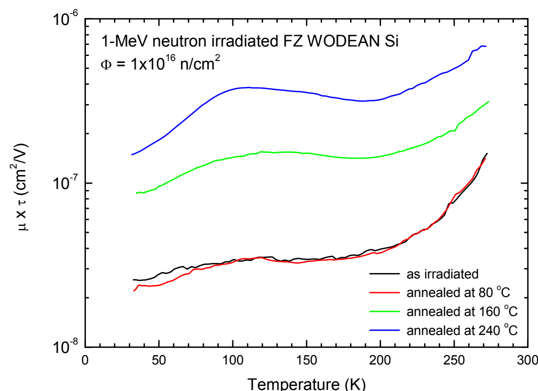

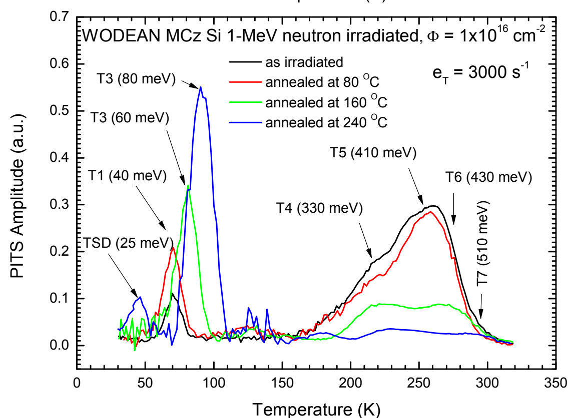

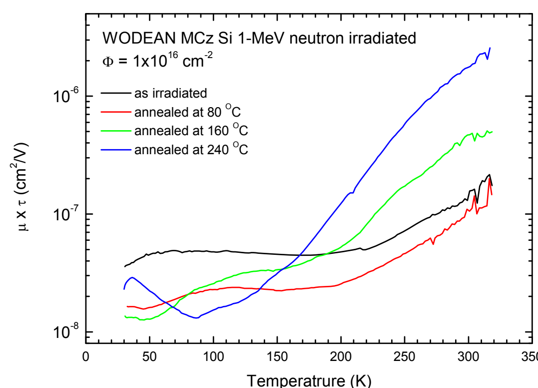

Fig. 3.3.3 Isochronal annealing effect on PITS spectra obtained for FZ (top) and MCz (bottom) Si samples for a fluence of 1×10^{16} cm^{-2}. Emission rate window e_T = 3000 s^{-1}.

Fig. 3.3.4 Isochronal annealing effect on the temperature dependence of charge carrier mobility-life time product for FZ (top) and MCz (bottom) samples irradiated to a fluence of 1×10^{16} cm^{-2}.

3.4 Photoconductivity spectra and deep levels in neutron irradiated pad-detectors

It is well known that the photoconductivity method allows the investigation of deep defect levels in semiconductors and many works were devoted to analyze the deep levels in silicon [5, 6]. In this work the photoconductivity spectral dependence is used for the demonstration of deep level dependence on irradiation and thermal treatments in highly irradiated p+-n-n+ Si detectors.

Samples and methods

The p^+-n-n^+ diodes fabricated on magnetic Czochralski silicon (MCZ) were investigated. The samples were irradiated with neutrons at the TRIGA reactor in Ljubljana with fluences in the range from 10^{13} to 1×10^{16} cm^{-2}. The isochronal annealing procedures for 15 h were performed by varying the temperature in the range of 80 – 180^{0}C. The I-V characteristics were measured at room temperature by an electrometer HP 4140B. The photoconductivity spectra were measured by using double prism monochromator DMR-4. The sample was placed in closed cycle He cryostat (ARS Cryo) and its temperature was measured by the controller Scientific Instruments 9700. The data were processed by PC with GPIB interface. The main measurements were performed at a bias voltage of 50 V. At this bias the low fluence irradiated samples were near to the full depletion regime. It was controlled by C-V measurement (at room temperature and at 18 K). For the samples irradiated with the highest fluence the I-V characteristics were near to linear. Therefore, the photoconductivity was caused by extracted non-equilibrium carriers in low irradiated samples. The photoconductivity of highly rradiated samples was dependent on the free carrier lifetime. The different regimes of photoconductivity in differently irradiated samples allow only an extraction of qualitative results, and only a very preliminary

comparison with quantitative data is possible. The measurements were performed by increasing the photon energy and afterwards by decreasing it. The difference of these results showed the role of non-equilibrium carrier induced by the persistent current. The decay of the persistent current was caused by the generation current and injection of carriers. The photoconductivity spectra were analyzed by using the deep center model with δ-potential (Lukovsky model) [7]. The cross section of photo-ionization was simulated by the formula [7]:

$$I \sim m \times \Delta E_M^{0,5}(h\nu - \Delta E_M)^{1,5}/(h\nu)^3),$$

where ΔE_M is the optical activation energy of deep centers, hν is the photon energy, m is the concentration of filled deep centers in case of electron excitation and the concentration of empty deep centers in case of hole excitation.

Results

The activation energy of the dark reverse current ΔE and the TSC in the high temperature region (near to RT) was slightly dependent on the irradiation in case of the non-treated samples, but a different dependence was observed for the isochronally treated devices (Fig.3.4.1).

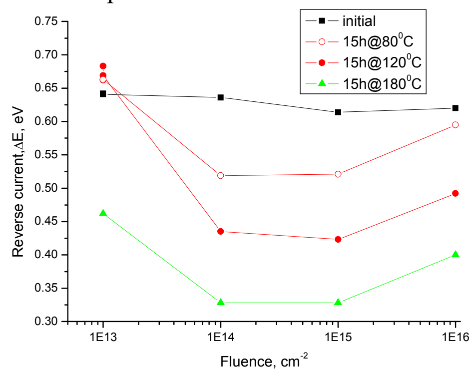

Fig. 3.4.1 Dependence of dark current activation energy ΔE on neutron fluence. Bias voltage 50 V.

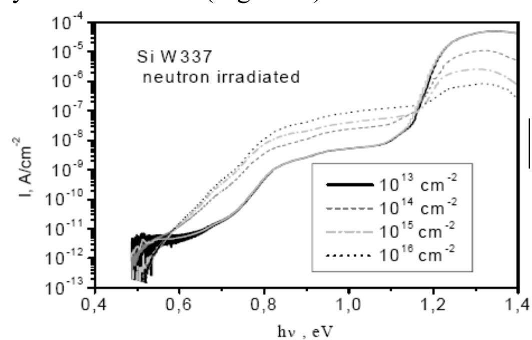

Fig. 3.4.2 The dependence of photoconductivity spectrum on neutron fluence. (fluence values given in the inset).

The activation energy, if to account a dependence of density of state on temperature, is very similar to the intrinsic generation lifetime activation energy and shows the thermal activation energy of compensated deep centers or the band gap. The dependence of activation energy on the thermal treatment indicates the changes in the structure of the defects.

The measurement of spectral dependence of photoconductivity allows the determination of the optical activation energy as the generation of carriers directly depends on the photo-ionization cross-section. The signal also depends on the deep level concentration and the regime of photoconductivity measurement. These measurements revealed a peculiarity that the photocurrent measured by increasing and decreasing the photon energy was approximately the same at temperature higher than 125 K but at lower temperatures the persistent current was observed. At lower temperature the persistent current was absent for photon energy less than 0.8 eV. If the photon energy was increased then the photocurrent was larger compared to that measured during decreasing the photon energy and the persistent current was observed. The decay time constant of this current at 18 K was a few hundred seconds. The results of the spectra measured by increasing the photon energy had been used for an analysis of deep levels. The irradiation by neutrons changes the shape of the photoconductivity spectrum (see Fig.3.4.2).

The decrease of photocurrent in the region of intrinsic absorption (1.2-1.3 eV) is caused by a decrease of free carrier lifetime. The increase of the neutron fluence caused an increase of the extrinsic photoconductivity in the region 0.65-1.1 eV and a decrease in the region at 0.5 eV. The decrease of the steady state lifetime is similar to the increase of the total impurity photoconductivity at lower fluences. It shows that these centers are responsible for the decrease of the steady state lifetime (Fig.3.4.3).

The deviation from the coincidence of these dependences at higher fluence can appear due to the two step excitation of electron-hole pair. Therefore, the decrease of lifetime influences the absolute value of the extrinsic photoconductivity.

Low temperature annealing changes the spectrum of deep levels and their contribution to the photoconductivity. Fig.3.4.4 shows the spectra of a neutron irradiated sample with a fluence of 10^{15} cm^{-2} and demonstrate the changes of the main deep levels during the isochronal annealing. The results of a detailed analysis of the impurity spectrum by using the Lukovsky model approximation are shown in the Fig.3.4.5.

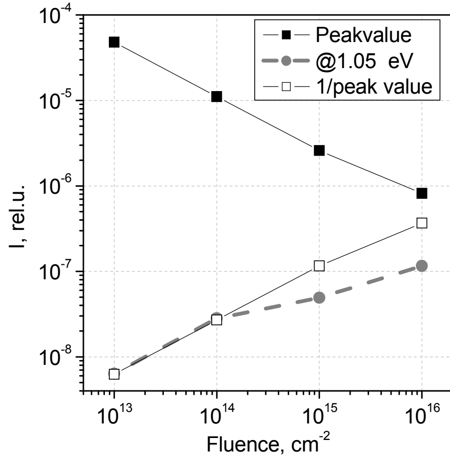

Fig.3.4.3 The dependence of the photoconductivity peak value and the main impurity band on the neutron fluence.

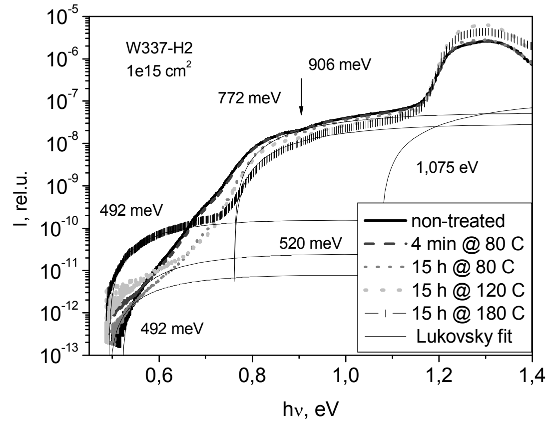

Fig. 3.4.4. The photoconductivity spectrum in neutron irradiated Si at fluence 10^{15} cm^{-2} after isochronal annealing. The thin lines correspond to fits of the Lucovsky model to the experimental data, the fitting parameters (deep level energies) are given in the insets.

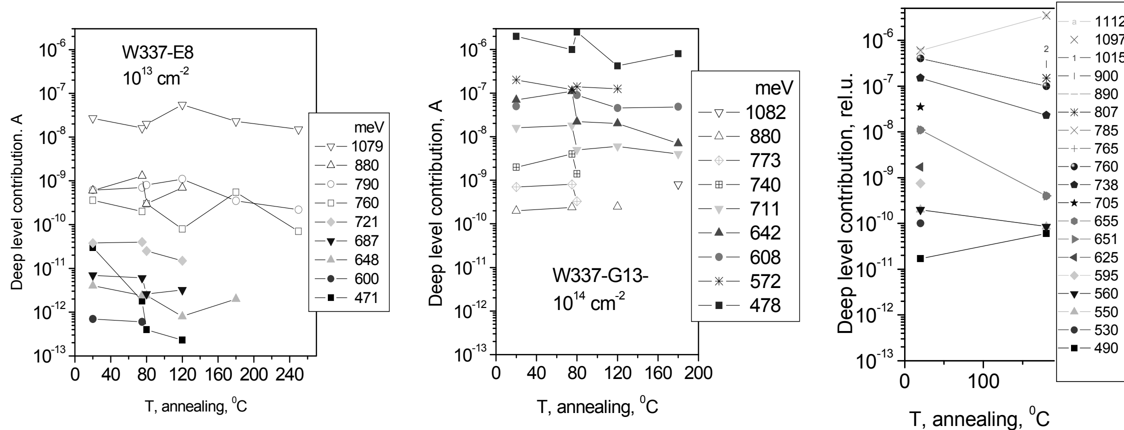

Fig.3.4.5 The deep level effective concentration dependence on isochronal annealing in neutron irradiated samples. a) – fluence 10^{13} cm^{-2} , b) – fluence 10^{14} cm^{-2}, c) – fluence 10^{15} cm^{-2}. Deep level optical activation energies are given in the insets. Double points at 80^0C correspond to the 4 min treatment (left) and 15 h (right).

Discussion

The optical activation energy measured by the spectral dependence of photoconductivity can be related to the excitation of free electrons from the filled deep center or the generation of free holes by excitation of electrons from the valence band to the empty local level. The observed most shallow level was at 0.5 eV that corresponds to the local levels near to the Fermi level. During annealing two groups of near to instantaneous distribution of levels were observed: in the range of more deep levels in the region of optical activation energies in a range of 0.52-0.57 eV and 0.59-0.75 eV below the conduction band. These levels, due to the large variation, are probably related to deep levels in the environment of clusters, and the variation of the activation energy is related to the defect potential barrier. A possibility of the existence of different local levels follows from the simulation of the introduction of vacancy cluster by neutrons [8]. Most clearly observed deep levels are at 0.77-0.81 eV. Less visible but well seen deep levels are at 0.88-0.91 eV. The deepest levels (1.02-1.11 eV) are near

to the valence band levels and the activation energy varies from 50 to 150 meV. Probably they are related to the disordered regions around the clusters. The irradiated and annealed samples can be characterized by a change of deep level concentrations and an appearance or quenching of additional ones, but these dependences develop in a non-gradually way. It can be explained as a statistical process involving different defect complexes. This result does not confirm the observed changes in DLTS and TSC measurements where the different defect concentrations change gradually. This is probably caused by different active volume in DLTS, TSC and photoconductivity measurements.

The Frank-Condon shift for a few deep levels in Si was evaluated in [6], and the obtained value is 40-50 meV. It allows to compare the deep level parameters measured by thermal activation [2] and in this work using optical excitation. Using this approximation it is possible to conclude that the levels related to the clusters at E_V +330 meV and at E_V +360 meV belongs to the main local levels responsible to the intrinsic photoconductivity. The centers E_V +420 meV and E_C -545 meV belongs to the group of levels at 0.59-0.75 eV, given above.

The comparison of the dependence of the measured steady state lifetime and photoconductivity decay time constant [9] shows the different fluence dependence. The steady state lifetime depends on irradiation with a square root of fluence dependence, and the photoconductivity decay constant exhibits a linear dependence on the fluence. It shows that the increase of defects during irradiation enhances the trapping of carriers, that recombines much slower and do not influence the main part of the decay constant.

Conclusions

The spectral dependence of photoconductivity is a sensitive method to analyze deep levels in neutron irradiated silicon. The neutron irradiation induces a set of deep levels and it changes with increasing fluence and during the low temperature treatment.

Furthermore, samples with Ohmic contacts are needed to perform quantitative measurement of deep level concentrations.

3.5 Annealing dependence of recombination and generation lifetime in neutron irradiated MCz silicon

Free carrier lifetime is one of the most important operational parameters of the Si particle detectors after high fluence irradiation [10]. High concentrations of the radiation induced carrier traps in detectors made of pure initial Si material also restrict applications of the most sensitive and elaborated characterization techniques, such as DLTS and TSC, for an evaluation of the carrier decay features [11, 12]. Therefore, direct methods for the control of the carrier recombination, trapping and transport are preferential.

Samples and measurement techniques

The magnetic Czochralski (MCZ) grown Si samples irradiated by reactor neutrons with fluences in the range from 10^{12} to $3\cdot10^{16}$ n/cm^2 have been examined. The wafer surfaces were passivated with thermal oxide. The isochronal annealing for 24 h was performed by varying the temperature in the range of 80 – 420^{0}C. Characteristics of the carrier recombination and trapping/generation were examined after each step of heat treatment.

In this work, carrier recombination and diffusion parameters have been examined by the non-invasive technique of microwave probed photoconductivity (MW-PC) transients [13], combining the photo-ionization spectroscopy [14] and measurements of the lifetime-temperature characteristics [15] in samples irradiated with different fluences and after several annealing steps.

The transient shape, constitution and characteristic lifetimes of different decay components dependent on fluence and annealing temperature have been examined at fixed excitation wavelength of 1062 nm (using 500 ps laser pulses) at room temperature (RT).

The measurements of the lifetime-temperature characteristics have been performed on samples treated at elevated temperatures (≥160^0 C), to separate recombination and trapping components. These characteristics are recorded by varying the temperature in the range of 20^0 C – 120^0 C. Such a measurement cycle takes around an hour.

Experimental results and discussion

Recombination lifetime, evaluated from transients showing a single-exponential decay in as-irradiated material, when measured at RT and at fixed 1062 nm excitation wavelength, is determined by the dominant defect center. This recombination lifetime decreases nearly linearly with increasing neutron fluence in a double logarithmic presentation (see Fig. 3.5.1).

Post-irradiation heat treatment induces variation of the constitution of transients and characteristic lifetimes of carrier decay components. The changes of characteristic lifetimes of the initial (τ_R) and asymptotic (τ_{trapping}) decays appear to be different for various irradiation fluences. Two components within carrier decay transients are caused by a competition of recombination and trapping centers, induced by annealing, in redistribution of excess carrier capture flows.

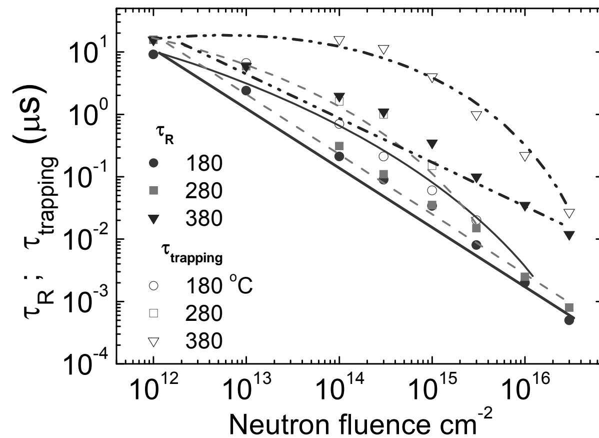

Fig.3.5.1 Fluence dependent variations of decay components and lifetimes under isochronal 24 h annealing at different temperatures.

The lifetime-temperature characteristics enable one to evaluate activation factors of each component resolved within carrier decay transients [15]. These characteristics measured in samples irradiated with different fluences before and after heat treatment are illustrated in Fig. 3.5.2.

It can be noticed that the recombination component is characterized by a rather weak dependence on temperature and can be approximated by a power function of T with an exponent 1.2-1.9 in the lower temperature range.

At higher temperatures the increase of the lifetime can be approximated by activation energy 0.13-0.16 eV in irradiated samples and this activation of the lifetime disappeared in the annealed samples. An additional constituent appears only in the annealed samples irradiated with fluences > 10^{13} n/cm^2. This decay component can be related to the thermal excitation from deep traps. It has a peak-like dependence on reciprocal thermal energy [15], which is evident for the annealed sample irradiated with 10^{16} n/cm^2 and occurs at lower temperature in less irradiated samples (Fig.3.5.2).

The step-like spectral variations of the photo-conductivity amplitude $U_{MW\text{-}PC}$ probed by microwaves occurs due to the spectral variation of the cross-section of the photon-electron coupling associated with deep levels (Fig. 3.5.3). These steps, simulated by the model of Lucovsky [7], enable one to evaluate optical activation energy E_i ascribed to different levels [5]. It is possible to choose the parameters of deep levels to fit the experimental data, but it is necessary to propose that the excitation of levels with optical activation energy at 465 meV and 745 meV induce the quenching of photoconductivity. The lines in Fig.3.5.3 correspond to fits with the parameters of deep levels given in Table 3.5.1.

As-irradiated Annealed (24 h 80 -380^{0}C)

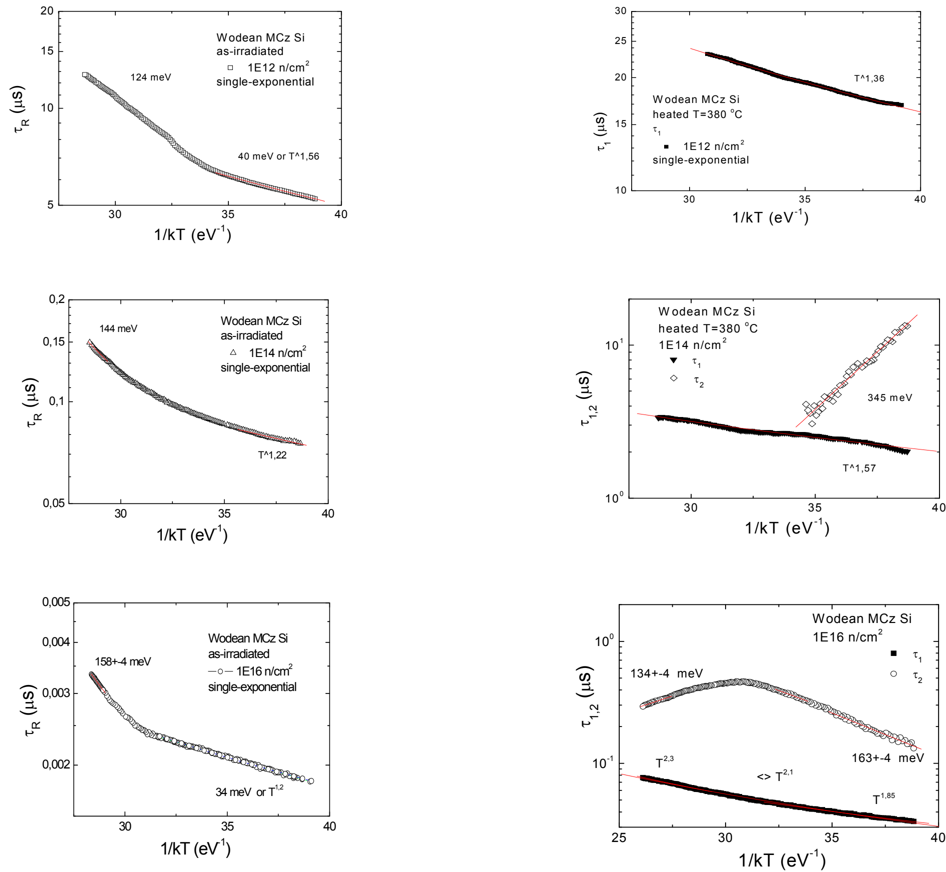

Fig. 3.5.2 Lifetime – temperature characteristics in the as-irradiated and annealed MCZ Si samples.

Table 3.5.1 Activation energies and effective concentrations after different fluences and thermal treatments.

Activation energy [meV]	Effective concentration [rel. units]			Remarks
	10^{12} cm^{-2}	10^{12} cm^{-2} treated	10^{16} cm^{-2} treated	
235	0.003	0.006	0.006	
315	0.08	0.08	0.08	(E_1)
445	2.5	2.5	22.5	(E_2)
465	0.04	0.35	1.2	Quenching E_C-E = 0.655 eV
580	9	6	80	
652		5	100	
688		1		
745	11.8	4000	20	Quenching E_C-E= 0.375 eV
790	30		1100	E-E_V= 0.33 eV
826	20	5	600	E-E_V= 0.294 eV
900			3000	E-E_V= 0.22 eV
980	2400	900	120	E-E_V= 0.14 eV

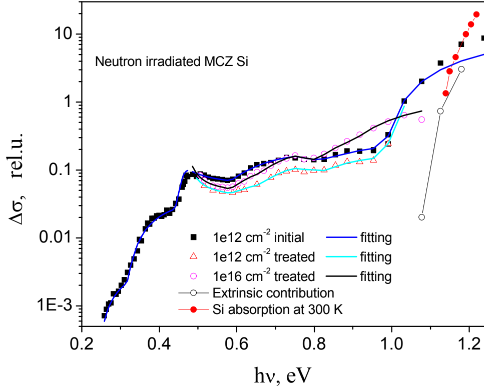

Fig. 3.5.3 Comparison of deep level spectra for as-irradiated and isochronally annealed samples at 280 °C for 24 h, irradiated with 10^{12} n/cm^2 (square, triangle) and 10^{16} n/cm^2 (open circle). Simulated spectral steps for E_1=0.31, E_2=0.40, E_3=0.50 and E_4=0.62 eV levels are represented by lines.

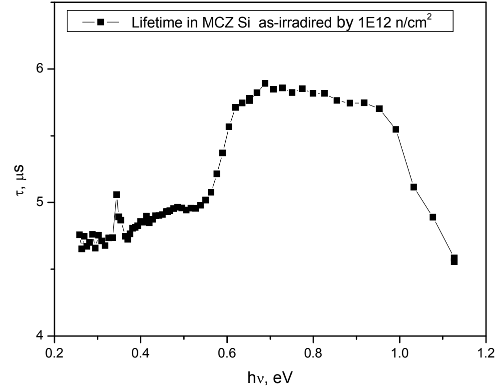

Fig.3.5.4 Spectral dependence of the lifetime in MCZ Si irradiated with 10^{12} n/cm^{-2}.

For as-irradiated Si samples, the deep levels with activation energies of 0.31 ± 0.01 (E_1), 0.40 ± 0.02 (E_2) as measured by DLTS and TSC techniques [11, 12] are ascribed to the VOH complex (E_1) and to the divacancy (E_2), respectively.

The recombination lifetime for spectrally resolved excitation with different photon energies varies slightly, as shown in Fig. 3.5.4.

In general, photoconductivity for bulk excitation (with 1062 nm wavelength) depends on the contribution of both types of carriers, and the amplitude of MW-PC is proportional to the product of free carrier mobility and lifetime. The mobility of holes is significantly smaller than that of electrons and, therefore, holes have only an impact on the diffusion of excess electron-hole pairs in a time scale exceeding the lifetime of holes. The capture of excess carriers is distributed among all of the electrically active defects. However, a single exponential decay observed in the as-irradiated material and the $1/\Phi_n$ dependence of the recombination lifetime in the annealed samples (Fig. 3.5.1) clearly indicates the dominance of a single recombination center. Simulations of neutron interaction with the silicon crystal [8, 16-17] indicate disordered regions with dimensions of about 0.1 µm which is less than the Debye length. Hereby, such regions act as extended cluster-like recombination centers. The cluster can be assumed as a volume with an inner defective surface which causes carrier diffusion from the non-disordered crystal and subsequent recombination at the cluster boundary. The effective lifetime τ_{Reff} for infinite velocity of surface recombination is determined by the minority carrier limited diffusion time $\tau_D = \pi^2 D_m/d^2$, as $1/\tau_{Reff} = 1/\tau_{Rcryst} + 1/\tau_D$ [13]. Here, D_m is the diffusion coefficient of holes (minority carriers), d is the averaged distance between the clusters, and τ_{Rcryst} is bulk recombination lifetime in the crystal. It follows from the data shown inFig.3.5.1 that the distance d changes from 200 µm to 20 nm, when the fluence increases from 10^{12} cm^{-2} to 10^{16} cm^{-2}. The analysis of the temperature dependence of τ_R, under the assuming that $\tau_R \approx \tau_{Reff}$, and $\tau_{Reff}(T)$ is mainly determined by a function $D_m=f(T)$, gives an exponential function $\tau_R \approx \tau_{Reff}, \propto T^n$, with 1<n<2. This corresponds to the proposed $D_m(T)$ and explains a rather small activation factor, in contradiction to the assumption of pure recombination on clusters with deep levels.

Changes of these regions under heat treatments change the density of trapping centers (Fig. 3.5.2). However, the spectral characteristics of deep centers (Fig. 3.5.3) show that the density of several levels changes during annealing and it shows the complicated character of the transformation of the centers that will be analyzed elsewhere. The asymptotic temperature dependences of the lifetime decay (Fig.3.5.2) also corroborate the manifestation of the cluster related recombination and different trapping centers for various fluence ranges. The latter changes of recombination-trapping characteristics can be explained by variation of distance d between clusters which depend on the irradiation fluence.

3.6 References

[1] I. Pintilie, E. Fretwurst and G. Lindström, Appl. Phys. Lett.. 92, pp. 024101, 2008
[2] I. Pintilie, E. Fretwurst, A. Junkes and G. Lindström, "Radiation induced point- and cluster – related defects with strong impact to damage properties of silicon detectors", presented at IEEE Nuclear Science Symposium and Medical Imaging Conference, 19-25 October 2008, Dresden, Germany.
[3] A. Junkes, E. Fretwurst and I. Pintilie, "Influences of cluster related defects on silicon detector properties", Presented on the 8th European Workshop on Radiation Effects on Components and Systems Eight European Conference on Radiation and Its Effects on Components and Systems (RADECS), Agora Center, University of Jyväskylä, Jyväskylä, Finland, 10 - 12 September 2008. Submitted to RADECS08 conference Proceedings and IEEE TNS
[4] R. M. Fleming, C. H. Seager, D. V. Lang, E. Bielejec, and J. M. Campbell, Appl. Phys. Lett. 90, pp. 172105, 2007
[5] Deep centers in Semiconductors, edited by S.T.Pantelides, Gordon and Breach, New York, 1986
[6] R. Passler, H. Pettersson, H.G.Grimmeiss, K. Schmalz. Phys.Rev.B 55 (1997) 4312
[7] G. Lucovsky, Solid State Communications, 3(9) (1965) 299
[8] M. Huhtinen, Nucl. Instr. and Meth. A 491 (2002) 194
[9] E.Gaubas, J.Vaitkus. Presentations at RD50 Workshops, 2007, 2008
[10] M.Moll, Nucl. Instr. and Meth. A 565 (2006) 202
[11] J.H.Bleka, L.Murin, E.V.Monakhov, B.S.Avset, and B.G.Svensson. Appl. Phys. Lett. 92. (2008) 132102.
[12] Presentations of B.Svensson and I.Pintilie at RD50/WODEAN workshop, August 2006, Hamburg
[13] E.Gaubas. Lith. Journ. Phys. vol. 43 (2003) 145-165
[14] E.Gaubas, A.Uleckas, R.Grogonis, V.Sirutkaitis, and J.Vanhellemont, Appl. Phys. Lett. **92** (2008) 222102
[15] E. Gaubas, J.Vaitkus, G.Niaura, J. Härkönen , E.Tuovinen , P. Luukka, and E. Fretwurst , Nucl. Instr. and Meth. A 546 (2005)108
[16] R.M.Fleming, C.H. Seager, D.V.Lang, P.J.Cooper, E.Bielejec, and J.M.Campbell. Journ. Appl. Phys. 102 (2007) 043711
[17] P.F. Ermolov, D.E. Karmanov, A.K. Leflat, V.M. Manankov, M.M. Merkin and E.K. Shabalina, Semiconductors 36 (2002) 1114

4 Defect Engineering

4.1 Epitaxial and MCz silicon

In continuation of the research plan new n- and p-type epitaxial layers with a thickness of 100 and 150 µm were grown by ITME. The pad-diodes were manufactured by CiS using different process technologies, either the standard process technology (denoted as EPI-ST) or performing an oxygen enrichment of the epi layer by a heat treatment for 24 hours at 1100 °C (denoted as EPI-DO), preceding the standard process steps. This way not only the oxygen concentration should be manipulated in the epi-layer but also the concentration of oxygen dimers.

4. 1.1 Material properties

In table 4-1-1 the main properties of the different n-type epitaxial layers and process variants are summarized.

Table 4-1-1 Material properties of EPI-layers

EPI-material	Type	Thickness [µm]	Resistivity ρ [Ω·cm]	Oxygen* [10^{16} cm^{-3}]
EPI-ST	n	75	150	9.2
EPI-DO	n	75	150	65
EPI-ST	n	100	300	5.4
EPI-DO	n	100	300	28
EPI-ST	n	150	480	4.5
EPI-DO	n	150	480	14
EPI-ST	p	150	1000	--

* the given concentrations represent mean values derived from the measured SIMS depth profiles.

The oxygen and carbon concentrations had been measured by Secondary Ion Mass Spectroscopy (SIMS) for the epi-layers [1]. In Fig. 4-1-1 the depth profiles are displayed for EPI-ST and EPI-DO samples after being fully processed.

- ***Oxygen profile in EPI-ST***

As can be seen for the as processed standard epi-layers (EPI-ST) oxygen is out-diffusing from the Cz substrate into the epi-layer up to a depth from the epi-layer substrate interface of about ½ of the total epi-layer thickness. The depth profile of the oxygen concentration near to the front side is due to an in-diffusion from the SiO_2-Si interface leading to an error function like distribution of the oxygen concentration in this surface region. In total a O-depth profile is achieved, which starts at the front side of the epi-layer with a concentration of about $8\cdot10^{16}$ cm^{-3}, decreases to values of about $2.2\cdot10^{16}$ cm^{-3} in a depth of 25 µm for the 75 µm epi-layer, $1.6\cdot10^{16}$ cm^{-3} in a depth of 40 µm for the 100 µm layer and about $9\cdot10^{15}$ cm^{-3} at 60 µm for the 150 µm layer. After these minimal values the concentrations increase up to $3.8\cdot10^{17}$ cm^{-3} at the epi-layer substrate interface for the 75 µm layer, $2\cdot10^{17}$ cm^{-3} for the 100 µm layer and $2.4\cdot10^{17}$ cm^{-3} for the 150 µm layer. Similar strong non-homogeneous profiles are typically observed for samples of fully processed epi-layers without the oxygenation treatment [2].

- ***Oxygen profile in EPI-DO***

The oxygen enrichment at 1100 °C promotes a further out-diffusion of oxygen from the substrate as well as from the SiO_2-Si interface. This treatment leads to a considerable increase of the oxygen content in the minimum of the corresponding EPI-ST profiles, up to $6.5\cdot10^{17}$ cm^{-3} for the 75 µm layer, $2.4\cdot10^{17}$ cm^{-3} for the 100 µm layer and up to $7\cdot10^{16}$ cm^{-3} for the 150 µm layer. The most homogeneous distributions throughout the main part of the epi bulk excluding the

surface region of 10 μm is observed for the 75 μm layer, where a decrease of the oxygen concentration is seen, most likely caused by an out-diffusion of oxygen.

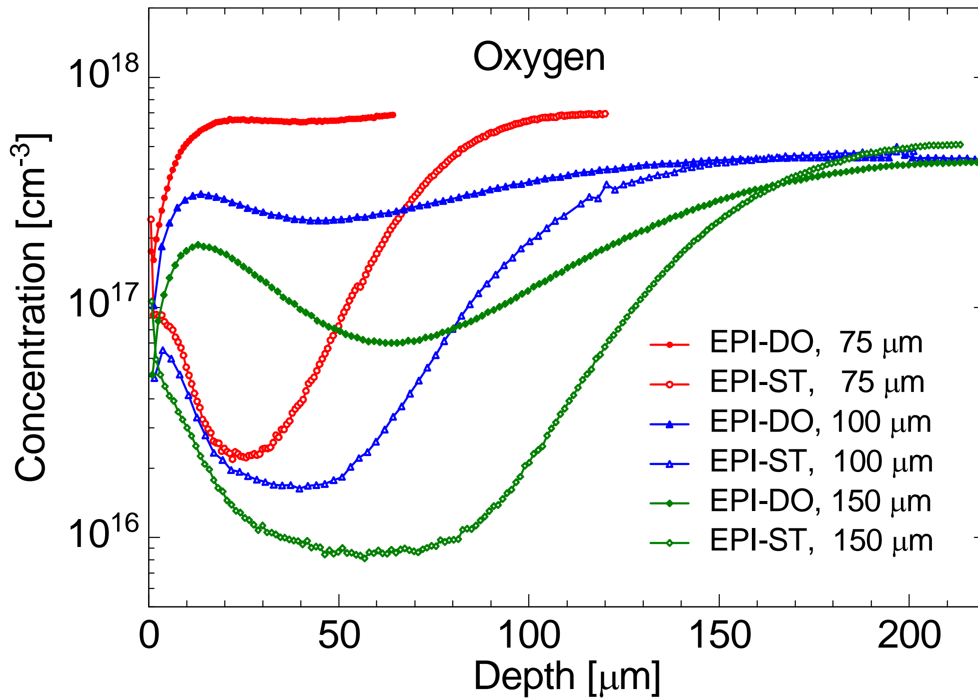

Fig. 4-1-1 Oxygen concentration profiles measured with SIMS in 75 μm, 100 and 150 μm n-type epi-silicon: after oxygen enrichment and full processing (EPI-DO), after standard processing (EPI-ST).

The carbon concentrations in the epi-layers vary between $1.2\cdot10^{15}$ cm^{-3} and $5\cdot10^{15}$ cm^{-3} for the different processing procedures but these values are supposed to be already below the detection limit of the SIMS-method.

For the MCz sample the oxygen and carbon depth profiles are shown in Fig. 4-1-2. Also in this case an out-diffusion of oxygen at the surface can be seen. As the carbon concentration is concerned, a value of $[C] = 2.5\cdot10^{15}$ cm^{-3} is observed. As mentioned before such a small concentrations is expected to be below the detection limit.

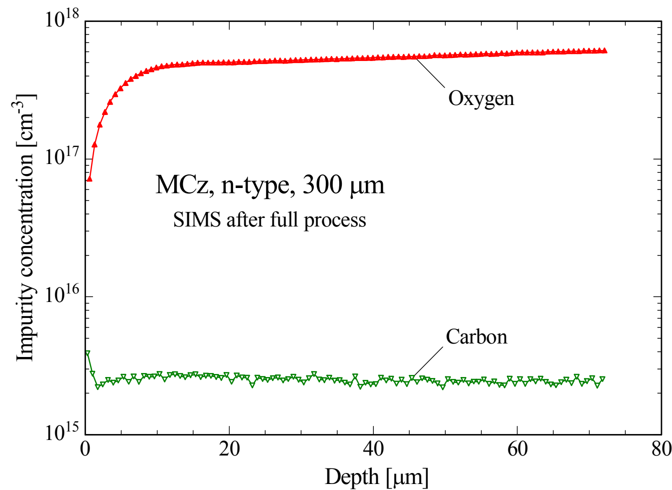

Fig. 4-1-2 Oxygen and carbon concentration profiles measured with SIMS in 300 μm thick n-type MCz silicon after full processing.

4.1.2 Formation of shallow donors in EPI- and MCz-silicon

It had been shown that the space charge sign of n-type epi-layers with a thickness of 25, 50 and 75 µm and a resistivity of 50 Ω·cm stays positive after 24 GeV/c proton damage up to fluences of 10^{16} cm^{-2} [2]. For large fluences in these epi-diodes the creation of acceptors is obviously always overcompensated by an introduction of shallow donors. The formation of these shallow donors was investigated by the Thermally Stimulated Current (TSC) method and it was demonstrated that the TSC signal due to the shallow donor had a very similar dependence on the material as the average oxygen concentration and the stable damage generation [2, 3]. It is believed that these radiation induced donors are related to oxygen dimers O_{2i}.

Previous DLTS studies [4] had shown that the introduction rate of the O_{2i} related defect IO_{2i} exhibits a quadratic dependence on the oxygen concentration in the material as suggested by the result of L. I. Murin et al. [5]. As the IO_{2i} defect complex can be regarded as a very sensitive indicator for the presence of O_{2i} in silicon it is suggested that under some prerequisites its concentration may be taken as a relative measure for the O_{2i} concentration in the material. The importance of O_{2i} for the formation of shallow donors in silicon after 24 GeV/c proton irradiation had been outlined in several papers [2, 3, 6].

It is expected that for neutron damage the introduction of shallow donors differs considerably to that induced by charged hadrons. Therefore, investigations of macroscopic device properties in correlation with microscopic studies (TSC measurements) in 75 µm standard (EPI-ST) and diffusion oxygenated epitaxial layers (EPI-DO) as well as 300 µm MCz material were performed after exposure to reactor neutrons [7]. For example the development of the effective doping concentration as function of fluence indicated that all materials undergo space charge sign inversion, depending on the initial doping concentration (donor removal) and the effective introduction of acceptors and donors. The space charge sign inversion had been proven by TCT-measurements with 670 nm laser light.

TSC measurements on all materials after irradiation with $5\cdot10^{13}$ n/cm^2 demonstrate that shallow donors (denoted as bistable donor $BD^{0/++}$ in Fig. 4-1-3) are generated in both epi-materials but in a much lower concentration in MCz material. All spectra, shown in Fig. 4-1-3, are taken for a reverse bias voltage which guaranties that the diodes stay fully depleted in the overall TSC temperature range. For the first time the bistability of the BD center could be directly observed in the EPI-DO diode as shown in Fig. 4-1-4. In the TSC spectrum measured directly after irradiation a peak at 49 K (attributed to $BD^{+/++}$) is recorded which vanishes after a short storage time of 3 hours at room temperature, but during a second measurement a strong increase of the (0/++) transition of the BD center is observed.

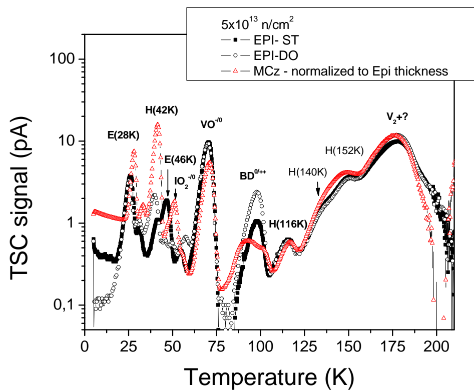

Fig. 4-1-3 TSC spectra after irradiation with $5\cdot10^{13}$ n/cm^2 recorded on a EPI-ST, EPI-DO and MCz diode. The TSC current of the 300 µm thick MCz diode is normalized to the thickness of the EPI diodes (75 µm).

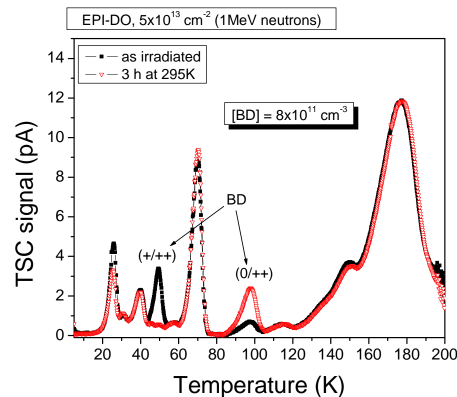

Fig. 4-1-4 TSC spectra recorded on a EPI-DO diode as irradiated to $5\cdot10^{13}$ n/cm^2 and after storage for 3 hours at 295 K.

The donor activity of both BD transitions had been proven by the temperature shift of their peak position as function of the applied bias voltage (Poole-Frenkel effect) for both BD transitions [7]. In addition to the bistable donor BD a TSC signal at E45 K (labeled E(45K) showed also a strong

temperature shift of the peak position to lower temperatures with increasing bias voltage pointing to a donor characteristic of this defect [7].

Annealing at 80 °C showed that the concentration of donors slightly increases (about 20 %) during the first period of about 80 minutes in all materials (see Fig. 4-1-5). The concentrations refer to the sum of the $BD^{0/++}$ signal and the TSC-peak E(45K). The introduction of these donors depends strongly on the material type. The BD concentration in the EPI-DO material is about a factor 1.5 larger compared to EPI-ST. This trend is understandable considering the higher oxygen concentration in EPI-DO but the corresponding ratio of the oxygen concentration is about 7. On the other hand the much lower BD concentration in the MCz material was not expected since the oxygen concentration in MCz is nearly the same as measured in EPI-DO. Thus, a direct correlation of the BD concentration with the oxygen content in the material as measured by the SIMS-method cannot be stated. It was suggested that oxygen dimers O_{2i} are involved in the creation of these donors but so far this hypothesis could not be substantiated by these results. Especially the nearly identical oxygen content in MCz and EPI-DO would point to a similar concentration of O_{2i} and, therefore, to a similar generation rate for the BD, which is in contradiction to the observation.

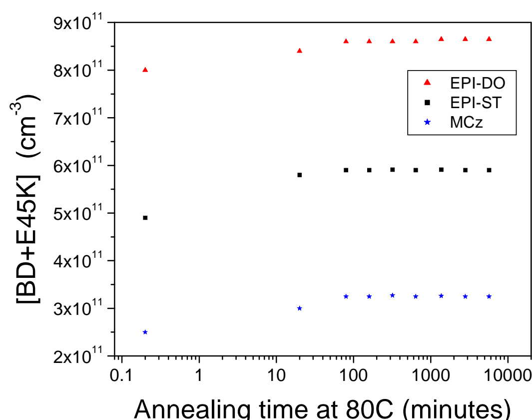

Fig. 4-1-5 Annealing behavior of the donor concentration (BD + E45K) at 80 °C in 75 µm EPI-DO, EPI-ST and 300 µm MCz diodes.

After irradiation of EPI-DO devices with 24 GeV/c protons TSC spectra were recorded after isothermal annealing at 80 °C. As an example in Fig. 4-1-6 spectra recorded after an annealing time of 11460 min are plotted for different reverse bias voltages. Here only the low temperature range between 5 K and 80 K is shown (see also chapter 3 of this report).

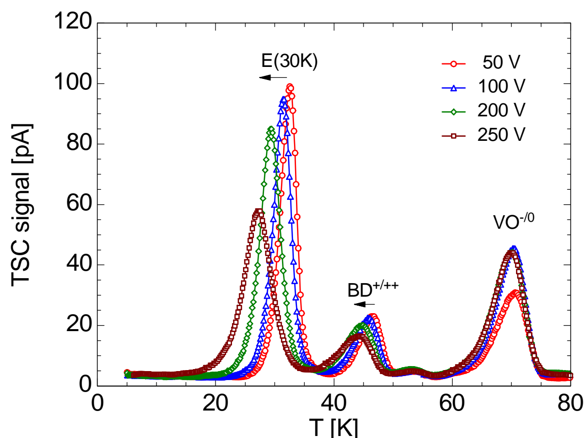

Fig. 4-1-6 TSC spectra of an EPI-DO diode after $2.3\cdot10^{14}$ cm^{-2} 24 GeV/c protons and for different reverse bias voltages.
Annealing time 11460 min at 80 °C.

Beside the well known VO signal two electron traps at about 30 K and at 45 K are observed. Both TSC peaks (30 K and 45 K) show a shift of the peak position to lower temperatures with increasing reverse bias indicating their donor character. The 45 K peak is assigned to the known bistable double donor BD_B in configuration B and the TSC signal corresponds to the transition $BD^{+/++}$ (see also Fig. 4-1-4). An assignment of the E(30K) donor to a specific defect cannot be given so far.

The annealing behavior of the E(30K) and the bistable donor BD at 80 °C is shown in Fig. 4-1-7 for EPI-DO diodes irradiated with 24 GeV/c protons ($\Phi_{eq} = 2.3\cdot10^{14}$ cm^{-2}) and reactor neutrons ($\Phi_{eq} = 1\cdot10^{15}$ cm^{-2}) as well as for an EPI-ST diode after neutron irradiation. For comparison of the different data sets the evaluated concentrations had been normalized to their individual 1 MeV neutron equivalent fluence values. The introduction rate for both donors E(30K) and BD(98K) is appreciably larger for protons compared to neutron damage. For the E(30K) trap in EPI-DO the ratio of the introduction rate between protons and neutrons is 2.4 and the corresponding ratio for the BD is 3.5. The difference in the E(30K) concentration between EPI-DO and EPI-ST after neutron irradiation is only 4 % and for the BD the ratio of EPI-DO and EPI-ST is 1.4. This is nearly the same after irradiation with the low neutron fluence of $5\cdot10^{13}$ cm^{-2} (see above).

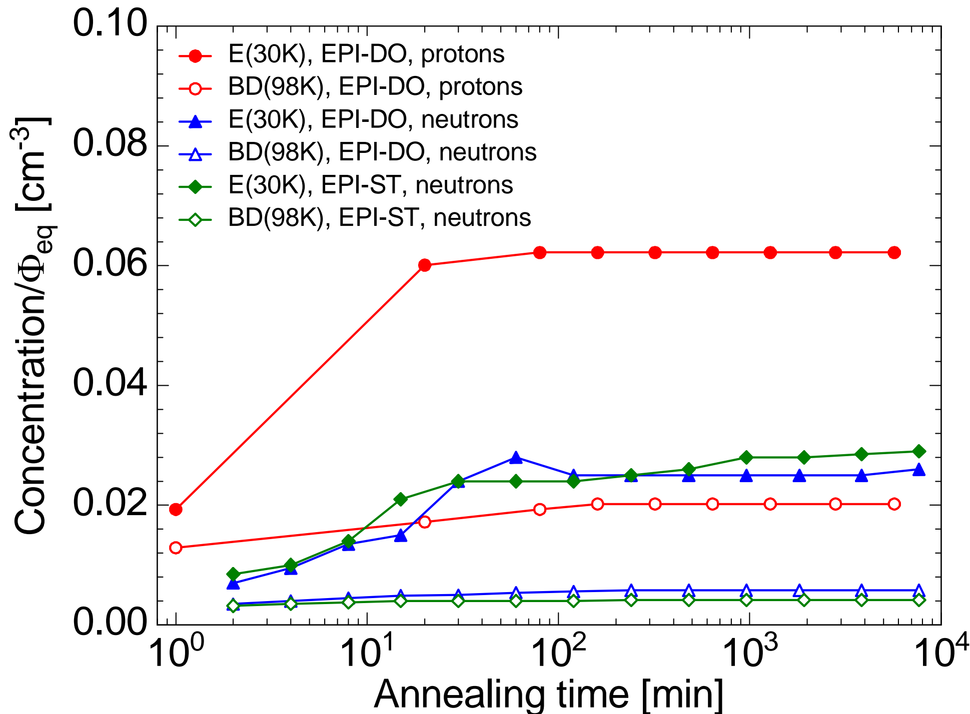

Fig. 4-1-7 Concentration of the donors E(30K) and BD(98K) normalized to 1 MeV neutron equivalent fluence versus annealing time at 80 °C for 75 µm EPI-DO after 14 GeV/c proton and neutron irradiation and 75 µm EPI-ST after neutron irradiation.

The short term annealing behavior of both donors after proton and neutron damage is partially responsible for the so called beneficial annealing of the effective doping concentration which was usually attributed to the annealing out of acceptors only. On the other hand the large introduction rate of donors induced by high energy protons explains why the space charge of this material stays positive up to extremely high fluences, i.e. no space charge sign inversion is observed.

Several questions are still open, e. g the defect structure of the E(30K) trap, is oxygen involved or is this trap an intrinsic defect, the basic formation kinetics. Also the differences between MCz and EPI-DO with respect to the donor formation are not understood although the oxygen concentrations are similar.

4.2 Hydrogenation of silicon

It is well-known that hydrogen can easily penetrate into silicon crystals at various stages of detector processing [8]. It is expected that an enrichment with hydrogen might lead to more radiation tolerant devices due to hydrogen passivation of radiation induced defects [8, 9] and an acceleration of oxygen diffusion by promoting the formation of oxygen dimers O_{2i} [10-12].

As already pointed out in the RD50 status report 2007, the major problem of the hydrogen enrichment is the quantitative evaluation of the hydrogen content. The lower limit for the detection of hydrogen by the Secondary Mass Spectroscopy (SIMS) method is about 10^{17} cm^{-3}. A ten times higher

sensitivity can be achieved for deuterium [1]. Therefore, in a first test experiment FZ samples were implanted with 710 keV deuterons. The dose value was chosen to be 10^{16} cm^{-2}. In order to prevent a fast out-diffusion of deuterium through the surface a 50 nm silicon nitride layer was deposited on top of the samples.

Fig. 4-2-1 presents depth profiles of the implanted deuterium concentration as recorded by the SIMS technique. The as implanted profile has a peak concentration of about $2 \cdot 10^{20}$ cm^{-3} at a depth of 7.5 μm which corresponds to the range of 710 keV deuterons in silicon. A heat treatment at 400 °C for one hour leads to a considerable broadening of the primary profile by diffusion. For one sample the nitride layer was removed before heating. This resulted in a larger diffusion length towards the surface and a less pronounced tail in the direction of the bulk compared to the sample with the nitride layer on top of the surface.

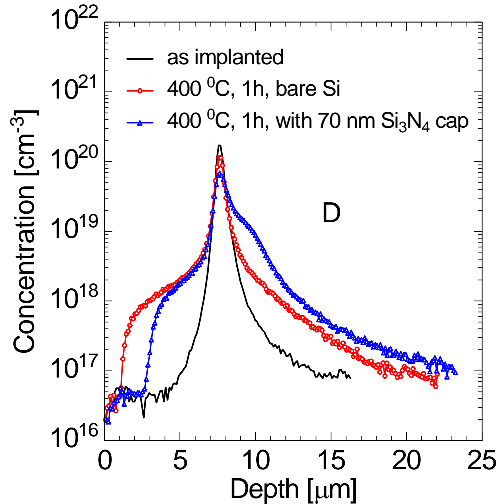

Fig. 4-2-1 Deuterium concentration depth profiles recorded by SIMS for as implanted and annealed samples at 400 °C for 1 h in Ar with and without a nitride surface layer.

Since the diffusion at 400 °C for 1 hour was not sufficient for a more homogenous distribution of the deuterium concentration, annealing experiments at higher temperatures were performed.

In Fig. 4-2-2 the SIMS profiles after annealing at 500 °C and 600 °C are shown. The treatment at 500 °C for 3 hours (Fig. 4-2-2(a)) promotes an increase of the diffusion front towards the surface. For the sample with a 70 nm Si_3N_4 layer on top of the surface the profile fills the gap between the surface and the peak fully. Without the nitride layer a strong out-diffusion of deuterium is observed. At 600 °C the out-diffusion through the uncovered surface is nearly complete and in the case of the nitride barrier layer the concentration drops also by more than one order of magnitude.

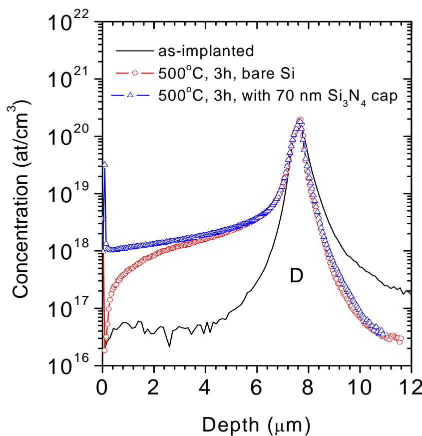

(a)

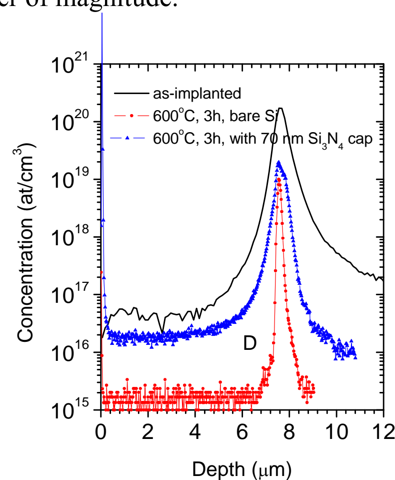

(b)

Fig. 4-2-2 Depth profiles of deuterium after annealing at 500 °C for 3 h (a) and 600 °C for 3 h (b) with and without a 70 nm Si_3N_4 surface layer.

These experiments show that also hydrogen should be detectable by SIMS if the concentration exceeds values above 10^{17}cm^{-3}.

In a new experiment an array of nine 50 µm thick EPI-diodes grown on 300 µm Cz substrates had been implanted through the rear side of the substrate with 5.5 MeV protons. This energy was chosen in order to get a layer with the maximal concentration at a position in the substrate which is about 10 µm away from the interface between the substrate and the epitaxial layer. This way it is expected that the EPI-diode will not be damaged by the proton beam. Several annealing procedures were assigned for a proper diffusion of the implanted hydrogen into the EPI-layer and the concentration profiles were controlled by SIMS measurements.

The depth profiles of the hydrogen concentration after different heat treatments are shown in Fig. 4-2-3. The different depth of the peaks for the as implanted and the annealed samples at 350 °C (see Fig. 4-2-3(a)) might be due to calibration problems in the depth measurement. The measured concentrations in the EPI-layers are near to the detection limit. For comparison the oxygen profile of the as implanted diode is included in Fig. 4-2-3(a).

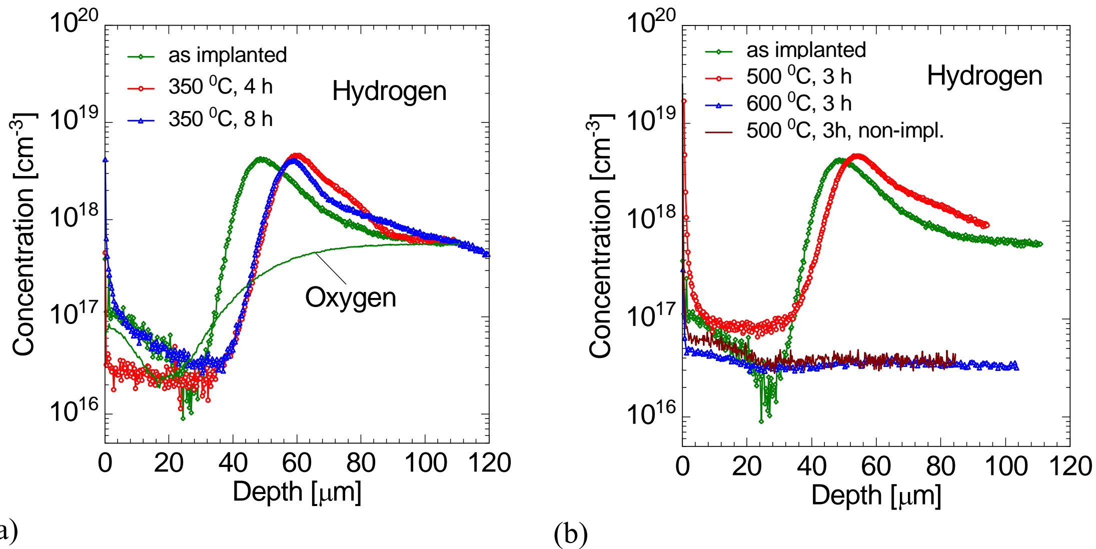

Fig 4-2-3 Concentration depth profile of hydrogen in 50 µm EPI-diodes: (a) as implanted, after annealing for 4 h at 350 °C and for 8 h at 350 °C; included: the Oxygen profile for as implanted diode; (b) after annealing for 3 h at 500 °C and 600 °C. For comparison in (b) the Hydrogen profile of a non-implanted but for 3 h at 500 °C annealed diode is included.

The treatment at 500 °C for 3 hours (see Fig. 4-2-3(b)) leads to a sufficient increase of the concentration of about 10^{17} cm^{-3}, while after annealing at 600 °C all hydrogen out-diffuses completely from the EPI-layer as well as from the substrate. For comparison a non-hydrogenated sample was also annealed at 500 °C for 3 hours and a SIMS measurement was performed. The recorded profile is included in Fig. 4-2-3(b) and the concentrations are similar to those obtained after annealing at 600 °C of an implanted diode.

Since an annealing of a diode at 500 °C for 3 hours would destroy the p^+-n junction by spiking of Al through the p^+-layers, the Al has to be etched off totally before the heat treatment. In order to prove the electrical properties of the diodes after implantation and after annealing at 500 °C current-voltage (I-V) and capacitance-voltage (C-V) characteristics were recorded and compared with the characteristics of a non-treated diode.

The current versus reverse bias and forward bias voltage characteristics are shown in Fig. 4-2-4 and Fig. 4-2-5, respectively. After implantation the reverse current increases by about two orders of magnitude and after annealing at 500 °C the I-V curve is shifted up to the µA range and break down occurs at about 80 V. These changes indicate that the EPI-layers are strongly influenced by the implantation and that part of the defects induced in the substrate diffuses into the EPI-layer. This effect is boosted by the annealing at 500 °C.

On the other hand the forward current characteristics are demonstrated in Fig. 4-2-5. As can be seen the shape and the absolute values are identical for the non-implanted and the as implanted diode. But the slope of the I-V characteristic of the annealed diode is considerably lower compared to the

other ones. At high forward bias voltages (> 0.6 V) the I-V curve becomes linear and the slope corresponds to a resistance of 600 Ω. This is typically seen in heavily damaged diodes.

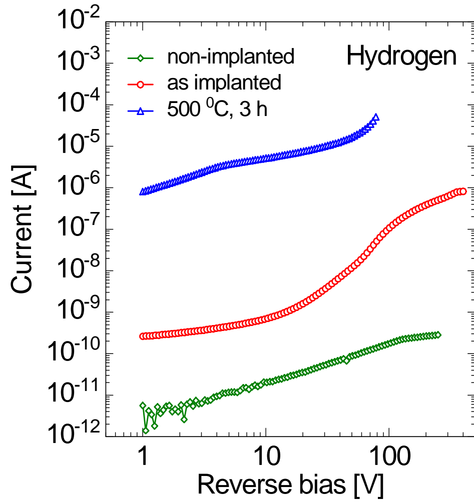

Fig. 4-2-4 Reverse current voltage characteristics for a non-implanted, implanted and at 500 °C for 3 h annealed diode.

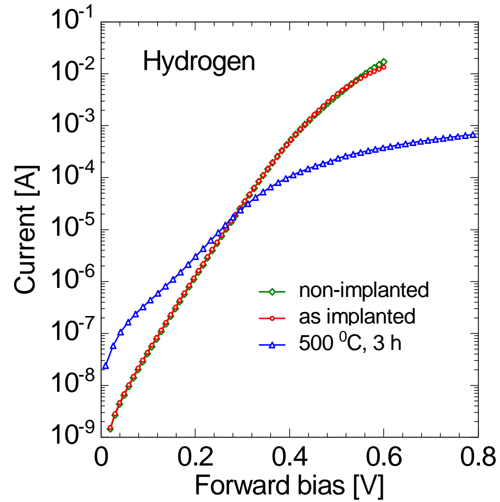

Fig. 4-2-5 Forward current characteristics for a non-implanted, implanted and at 500 °C for 3 h annealed diode.

Further doping depth profiles were extracted from C-V characteristics recorded with a frequency of 100 kHz (see Fig. 4-2-6). For the non-implanted diode a flat profile up to the interface between the EPI-layer and the substrate at about 50 µm is observed. The as implanted diode shows a strong increase of the doping concentration N_d towards the interface. This might be due to a formation of thermal donors which is promoted by out-diffused hydrogen from the substrate into the region of the EPI-layer where the oxygen concentration is high (see Fig. 4-2-3 (a)).

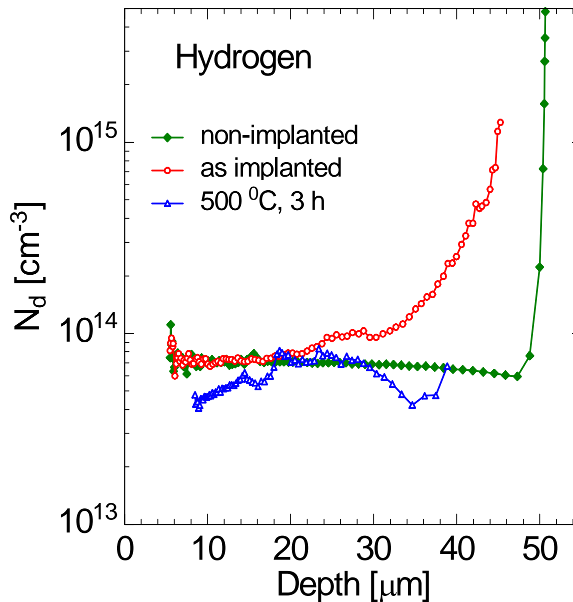

Fig. 4-2-6 Depth profiles of the doping concentration for a non-implanted, as implanted and at 500 °C annealed diodes. C-V recorded for 100 kHz.

The doping concentration of the annealed diode is the same in the region between 20 µm and 30 µm as measured for the non-annealed diode. The deviation in the front region and for the region > 30 µm is not understood, but it should be kept in mind that the C-V characteristic is distorted by a high concentration of defects. The limited depth of profile to 40 µm is caused by break down.

Very first measurements on defects were performed by Deep Level Transient Spectroscopy (DLTS) on the as implanted diode. In Fig. 4-2-7 DLTS spectra for fill pulses of V_p = -0.1 V (electron injection) and V_p = +3 V (hole and electron injection) are plotted.

It is obvious that defects are formed in the EPI-layer due to the implantation of hydrogen. The well known defect levels VO(-/0) and V_2(-/0) are seen if the duration of the fill pulse is short (100 µs). For the long fill pulse duration (100 ms) negative signals dominate the spectrum below 170 K. It seems that in the temperature range hole traps are filled although the fill pulse is negative (-0.1 V) and, therefore, only electron traps should be filled. This very strange effect could not be clarified so far. Forward biasing results in the spectrum shown in part (b) of Fig. 4-2-7. For the fill pulse duration of 100 ms two dominant peaks at 100 K and 170 K are detected, while for the short fill pulse in the low temperature range the electron trap VO is visible. All hole traps detected in this sample cannot be assigned to known defects. More detailed studies are needed for a better understanding of these spectra.

These first results on hydrogenation by implantation of MeV protons and annealing at high temperatures demonstrate that the induced radiation damage leads to a deterioration of the electrical properties of the diodes beyond acceptable levels. Therefore, one has to search for other techniques avoiding any radiation damage or reducing the damage as much as possible.

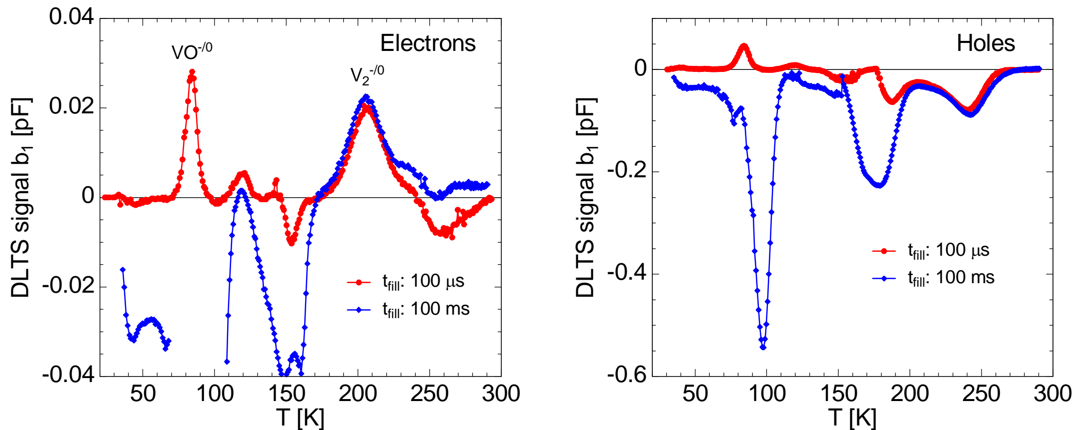

Fig. 4-2-7 DLTS spectra of an as implanted diode after electron injection (a) and after forward biasing (hole and electron injection) (b). Reverse bias voltage V_{rev} = -10 V, fill pulse V_p = -0.1 V (a) and V_p = +3 V (b), duration of fill pulse t_{fill} = 100 µs and 100 ms.

4.3 Defect engineering by pre-irradiation treatments

In the frame of the RD50 research project, the INFN in Padova, the Institute of Nuclear Research (KINR) in Kiev, ITC IRST in Trento and CNM in Barcelona have investigated radiation hardening by preliminary neutron irradiation of silicon, which is expected to create gettering sites in the silicon bulk. Preliminary irradiation of silicon by fast neutrons and the subsequent annealing lead to the formation of sinks for primary radiation defects. These sinks are complexes of radiation-induced defects with neutral impurities, such as C and O, always present in the silicon wafers. The optimal value of annealing temperature was found experimentally. It was shown that after pre-irradiation and annealing procedures the changes in the electrical characteristics with respect to un-irradiated samples are negligibly small [13]. For comparison Neutron Transmutation Doped (NTD) silicon was included in the investigation.

The investigated materials are summarized in the following Table 4-3-1:

N-type silicon:

Producer	Type	ρ [kΩ·cm]	τ [µs]	d [µm]	Processing
TOPSIL	FZ	~ 43 ~ 46 after pre-irrad.	~ 1000	310	ITC IRST
TOPSIL	FZ NTD	~ 3	~ 600	280	ITC IRST

The irradiation of the different devices were performed at the research reactor of the Jozef Stefan Institute in Ljubljana. In Fig. 4-3-1 the development of the effective doping concentration $|N_{eff}|$ as function of fluence is shown for the different n-type materials. For all devices space charge sign inversion (SCSI) is observed for fluence values above 10^{14} n/cm^2. Thus, the linear increase with fluence is interpreted by an introduction of negatively charged acceptor like defects in the space charge region. The introduction rate β found for the pre-irradiated diodes (β = 0.011 cm^{-1}) is about a factor of 2.5 smaller compared to standard FZ samples (β = 0.028 cm^{-1}) and for the NTD material a value of β = 0.015 cm^{-1} is extracted.

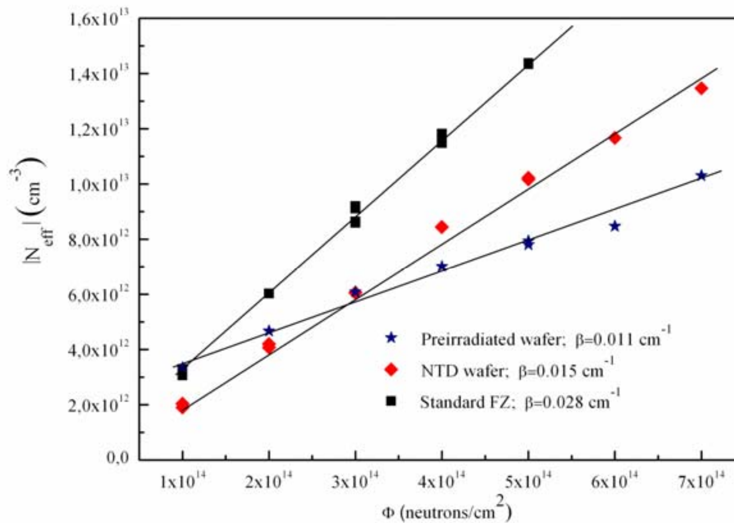

Fig. 4-3-1 Effective doping concentration as function of fluence for the n-type standard FZ, NTD and pre-irradiated devices. The lines are linear fits of the experimental data.

The reverse current per unit volume as function of fluence is plotted in Fig. 4-3-2. All values are taken after irradiation without any annealing. The current related damage constant α of pre-irradiated samples is about 10 % larger compared to standard FZ and for NTD samples α is about 20 % lower than the FZ value.

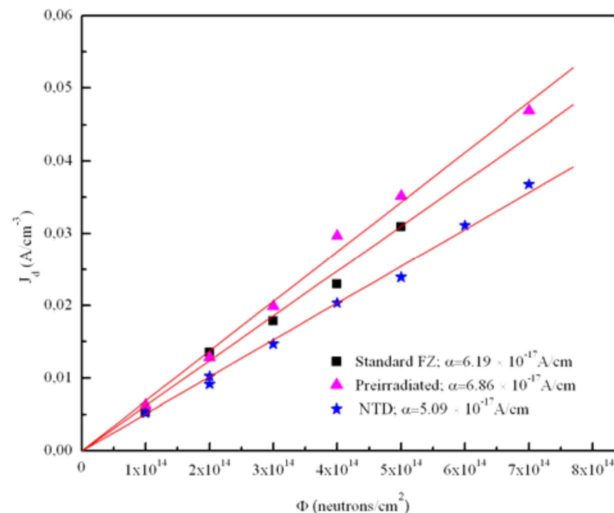

Fig. 4-3-2 Reverse current per unit volume as function of fluence for pre-irradiated, NTD and standard FZ diodes.

Charge collection efficiency (CCE) measurements with β-particles have been performed with the set-up at the Jozef Stefan Institute in Ljubljana. In Fig. 4-3-3 the fluence dependence of the collected charge at full depletion relative to non-irradiated diodes is shown for the different materials.

The development of the collected charge with fluence is similar for NTD and pre-irradiated devices, while for FZ a lower efficiency is observed.

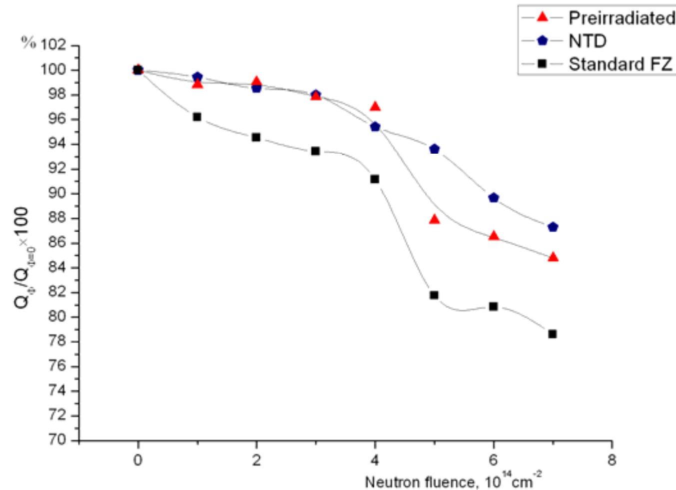

Fig. 4-3-3 Charge collection efficiency versus neutron fluence for pre-irradiated, NTD and standard FZ devices.

4.4 References for Chapter 4

[1] A. Barcz, SIMS laboratory, Physics Institute of the Polish Academy of Science, Warsaw, Poland

[2] G. Lindström, I. Dolenc, E. Fretwurst, F. Hönniger, G. Kramberger et al., Nucl. Instr. and Meth. A 568 (2006) 66-71

[3] I. Pintilie, M. Buda, E. Fretwurst, G. Lindström, J. Stahl, Nucl. Instr. and Meth. A 556 (2006) 197-208

[4] F. Hönniger, E. Fretwurst, G. Lindström, G. Kramberger, I. Pintilie, R. Röder, Nucl. Instr. and Meth. A 583 (2007) 104-108

[5] L.I. Murin, T. Hallberg, V.P. Markevich and J.L. Lindström, Phys. Rev. Letters Vol. 80 Number 1 (1998) 93-96

[6] G. Lindström, E. Fretwurst, F. Hönniger, G. Kramberger, M. Möller-Ivens, I. Pintilie, A. Schramm, Nucl. Instr. and Meth. A 556 (2006) 451

[7] I. Pintilie et al., paper presented at the IEEE-NS Symposium, Dresden, 15-25 October, 2008

[8] S.J. Pearton, J.W. Corbett, and M. Stavola, Hydrogen in Crystalline Semiconductors, Springer-Verlag, Berlin, 1992

[9] O.V. Feklisova, N. Yarykin. Semicond. Sci. Techn., 12 (1997) 742

[10] R. C. Newman, J. H. Tucker, A. R. Brown, and S. A. McQuaid. J. Appl. Phys. 70 (1991) 3061

[11] V. P. Markevich, L. I. Murin, J. L. Lindström and M. Suezawa. Semiconductors 34 (2000) 998

[12] R C Newman J. Phys.: Condens. Matter 12 (2000) R335

[13] P.G. Litovchenko, D. Bisello, A. Candelori, A.P. Litovchenko, A.A. Groza, et al., Radiation hardening of silicon for detectors by preliminary irradiation, Solid State Phen., vol.95-96 (2004), pp. 399-404

5 Pad Detector Characterization (PDC)

In the last year a major effort was devoted to understanding the open questions regarding the operation of irradiated silicon detectors. The main focus was concentrated on:

- Understanding the damage after irradiation of detectors exposed to irradiation fields resembling those of LHC experiments. So called mixed irradiations were performed where irradiations by fast charged hadrons (pions or protons) were followed by additional neutron irradiations.
- Measurements of charge collection efficiency for minimum ionizing particles for over-depleted detectors ($V>>V_{fd}$). Under this condition the loss of CCE depends on effective trapping probabilities only. In this way a cross-check with TCT measurements can be made in terms of particle and material dependence of trapping parameters.
- The dependence of full depletion voltage (V_{fd}) on fluence and annealing time for various materials after fast charged hadron irradiations. Particularly important are systematic studies of V_{fd} and electric field profile of detectors made on MCz and epitaxial wafers.
- Finding the correlation of V_{fd} with CCE at high fluences.

5.1 Effective doping concentration in different materials

The evolution of effective doping concentration and consequently V_{fd} after irradiation can be described by three terms ("Hamburg model" [1]): the decay of effective acceptors immediately after irradiation ("beneficial annealing" - *Na*), stable part (*Nc*) and creation of the effective acceptors at late annealing stages ("reverse annealing", *Ny*):

$$\Delta Neff = N_{eff0} - N_{eff} = N_a(\Phi,t) + N_c(\Phi) + N_y(\Phi,t)$$
$$Na(\Phi,t) = g_a \cdot \Phi \cdot \exp(-t/\tau_{ra})$$
$$Nc(\Phi) = N_{C,0}\left(1-\exp(c\Phi)\right) + g_c\Phi \qquad ,$$
$$Ny(\Phi) = gy\Phi(1-\exp(-t/\tau_{ra})) + N_{Y,2}\Phi,t)$$

where $N_{eff,0}$ denotes the initial dopant concentration, g_a and g_y introduction rate of defects assuming the 1st order dynamics and τ_{ra} and τ_a the corresponding time constants. The removal of initial dopants is described by the first term in N_c ($N_{C,0}$ denotes the concentration of initial dopants being removed) and generation of stable defects by g_c.

Although the effective doping concentration in silicon detectors is not constant and it exhibits space charge of different sign at both contacts [2,3,4,5], the model with limited validity is still used to compare detectors. It works very well for FZ detectors and fails mostly for oxygen rich detectors. It nevertheless qualitatively describes the evolution of V_{fd} after irradiation.

5.1.1 Beneficial annealing

The beneficial annealing seems to be the least significant part of the damage due to short (~14 days at RT, ~8 min at 80°C) time constant and introduction rate (g_a~0.01 cm^{-1} [1]) which is smaller than for stable damage and long term annealing. Moreover it is difficult to measure precise introduction rate and time constant especially at larger fluences, due to so called "self annealing" during irradiations [6]. There are indications that at high fluences (>10^{15} cm^{-2}) the time needed for completion of beneficial annealing (time to reach minimum in V_{fd}) is prolonged up to few tens minutes at 80°C [7].

5.1.2 Stable damage

The stable part in FZ silicon which was the only detector grade material up to recently is always of negative sign [8]. As the reverse annealing and stable damage represent the introduction of effective

acceptors the increase of $|N_{eff}|$ and consequently V_{fd}, was kept as low as possible by keeping the detectors cold for most of the time. The RD48 collaboration proved the positive role of oxygen after irradiations with fast charged hadrons [8]. The introduction rate of stable acceptors was reduced by around factor of 3 when compared to STFZ detectors. In addition it was shown that long term annealing time constants are prolonged for high [O].

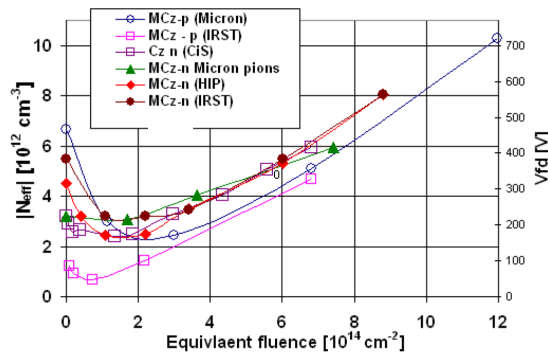

Fig. 1: The dependence of $|N_{eff}|$ on charged hadron fluence for different oxygen rich materials [14-16] after completed beneficial annealing. The processing company is given in the brackets.

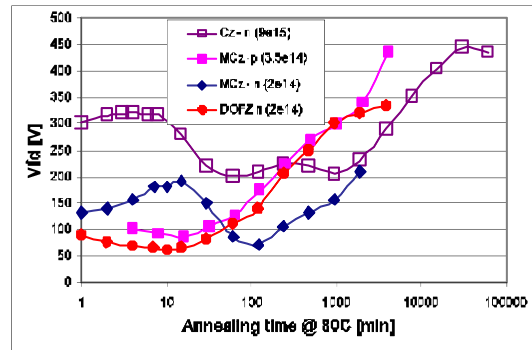

Fig. 2: The evolution of full depletion voltage with time for the same materials as in Fig. 1. Number given in the brackets denotes the equivalent fluence in cm^{-2}.

The oxygen concentration in DOFZ is around $2\cdot10^{17}$ cm^{-3}, which is an order of magnitude lower than the [O] in MCz/Cz materials [9,10]. The MCz n-type detectors do not undergo SCSI ("movement of the main junction") after irradiation with 24 GeV protons (see Fig. 1). The N_{eff} of MCz-n (wafers from Okmetic, Finland) or Cz-n (wafers from Sumitomo, Japan) type detectors first decreases, due to initial donor removal, and than starts to rise as the stable donors are introduced. A strong confirmation of that assumption can be seen in Fig. 2 where annealing behavior for MCz/Cz n-type material is typical for detectors with positive space charge. A natural assumption would be that also MCz-p type detectors beyond certain fluence become n-type after the initial shallow acceptors are compensated by radiation induced stable donors. However, MCz-p type detectors after initial decrease remain p-type at all fluences [11,12] (see Figs. 1,2). It is therefore a puzzle why all oxygen rich materials, including, DOFZ show similar increase of V_{fd} with fluence.

All the previous observations were confirmed this year with more measurements [13-17]. The introduction of predominant negative space charge in MCz-p samples irradiated with 24 GeV protons over large fluence range was confirmed by annealing studies and is shown in Fig. 3. However at the highest fluence the annealing behavior shows the evolution typical for detectors of predominantly positive space charge (initial increase of V_{fd} and later decrease) [17]. Although a quantitative explanation is not possible it seems as the defects produced during irradiation are active under electric field in such way that initially there are slightly more acceptors and later on the donors prevail. As the $N_{eff}\neq const.$ the V_{fd} can be different from 0 even if the net charge in detector vanishes. A similar observation can hold for MCz-n detectors where the donors prevail.

The electric field distribution measured by TCT for MCz-p detector irradiated with 24 GeV protons to $\Phi_{eq}=8.8\cdot10^{14}$ cm^{-2} is shown in Fig. 4. The induced current (proportional to electric field) after injection of carriers by short red laser pulse and corrected for trapping shows distribution typical for almost homogenous electric field with small peaks at both contacts. The interpretation of the TCT signals depends strongly on effective trapping times constants which are at high fluences of few ns order. Since trapping correction requires exponentiation of the measured signal curves to account for trapping already slight variation of trapping time constants can result in different interpretation. Namely, the comparison of TCT signals measured by different groups [15,18] for detectors produced on the same wafers and irradiated together show a very good agreement although different conclusions were drawn. As will be shown the conclusion made on the dominant space charge in MCz-p detectors after irradiation with fast charged hadrons is confirmed also with mixed irradiations.

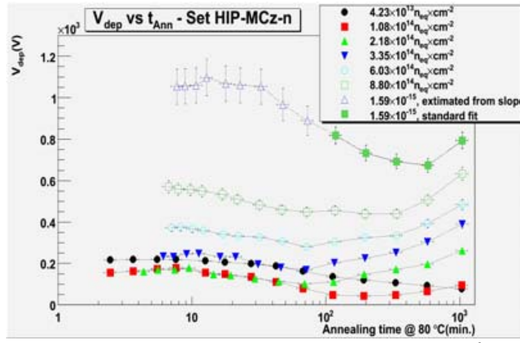

Fig. 3: Evolution of V_{fd} during annealing at 80°C for MCz-p irradiated detectors irradiated to different fluences of 24 GeV/c protons. Note the different behavior of the most irradiated sample.

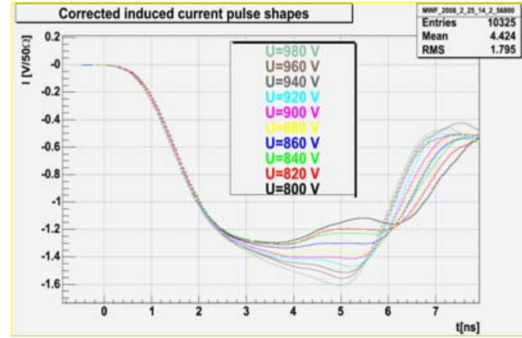

Fig. 4: Induced current pulse shapes after trapping correction for MCz-p detectors irradiated to Φ_{eq}=8.8·10^{14} cm^{-2}after 1000 min annealing at 80°C.

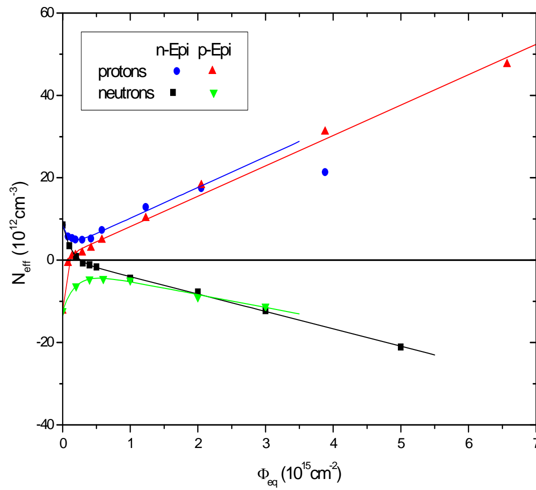

Fig. 5: N_{eff} of 150 μm thick epitaxial detectors irradiated with 24 GeV protons and neutrons.

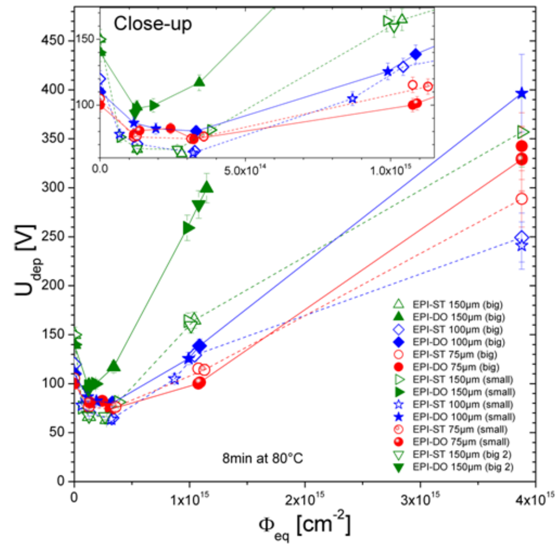

Fig. 6: N_{eff} of different epitaxial detectors irradiated with 24 GeV protons [39]. Please not that g_y in this case denotes introduction rate of stable donors. The Epi-Si wafers ware produced by ITME, Warsaw.

The introduction of donors with charged hadrons was observed also for epitaxial silicon detectors, but unlike MCz, for both n and p type detectors (see Figs. 5,6). The epitaxial silicon detectors have much lower [O] concentration of order 10^{17} cm^{-3} [19] than MCz/Cz, but the fraction [O_{2i}]/[O] in epi-Si detectors is much larger than in MCz [20]. The introduction of shallow bistable donors (BD) is assumed to be related to the [O_{2i}], which is assumed to be the precursor [21,22] for BD creation. The most probable reason is out-diffusion of O_{2i} from Cz substrate to epitaxial Si during the thermal treatments involved in device processing. That also explains different introduction rate of bistable donors for different detector thicknesses measured in [19,20] and at the same thickness for different detector processes. In the last report it was shown that the same starting material (150 μm epi-n type wafers) processed by different labs resulted in almost a factor of 2 difference in donor introduction rate [23].

In order to establish the role of oxygen several epitaxial wafers were oxidized by diffusion to reach oxygen concentrations between 2-6·10^{17} cm^{-3}. The role of oxygen in generation of positive space charge after 24 GeV proton irradiations is nicely observed. When compared to the non-oxygenated detectors from the same material (also same process - CiS) DO detectors exhibit larger introduction

rate of donors (see Fig. 6) [16]. The difference varies with detectors thickness being almost a factor of two for 150 μm thick detectors and 30% for 75 μm thick detectors.

The stable damage seems to depend on detector initial resistivity also for materials other than Epi-Si as reported in Ref. [24]. As shown in the last report 50 μm FZ-n type detectors of initial resistivity ~50 Ωcm undergo SCSI while higher resistivity detectors of all thickness do not. As thin detectors processed on high resistivity wafers exhibit no such behavior after 24 GeV p irradiations [25] the effect seems to be related to initial doping concentration rather than thickness of device. On the other hand the diffusion of oxygen during processing can also be more important in thin detectors.

Epitaxial n-type detectors don't undergo SCSI also with 26 MeV protons until the late stages of reverse annealing. On the other hand the MCz n-type detectors do undergo SCSI after few times $\Phi_{eq}=10^{14}\text{cm}^{-2}$ of 26 MeV protons [26], which has been confirmed by evolution of V_{fd} during annealing and TCT measurements. The 24 GeV protons are between the neutrons and 26 MeV protons in terms of ratio "cluster damage/point defects", which only adds to the controversy of SCSI in MCz detectors.

The initial donor removal after 24 GeV p irradiations seem to be almost complete $N_{eff,0}=N_{C,0}$ for FZ (shown already by RD48 collaboration [8]) and MCz detectors (see also Fig. 1). Studies of donor removal for epitaxial detectors revealed the correlation with oxygen concentration. . It was also found 90% of the donors are removed for DO sensors, while only 60% for standard epitaxial detectors. Also the removal rate declines with larger oxygen concentration [16]. For the samples shown in Fig. 6 it is around 2-3 times smaller than in non-oxygenated samples. Almost complete acceptor removal was observed for MCz-p detectors [11,12,27]. Due to higher resistivity of FZ-p wafers the measurements of acceptor removal require more detailed studies, which are yet to be performed. Also the measurements of removal rate and fraction of removed initial acceptors need further studies.

NEUTRON IRRADIATIONS

The stable damage in neutron irradiated detectors is always of negative sign regardless of the silicon type. The only exception observed so far were thin n-type epitaxial detectors (50,75 μm) of low resistivity (50 Ωcm) [26], where no SCSI was observed and effective donors were generated. The introduction rate of stable acceptor seems to be related to resistivity or thickness. Around 3 times smaller g_c~0.006 cm^{-1} [28,29] was measured in epitaxial detectors, but also in thin FZ and MCz detectors of resistivity lower (see Fig. 7)[28] than in materials of standard thickness.

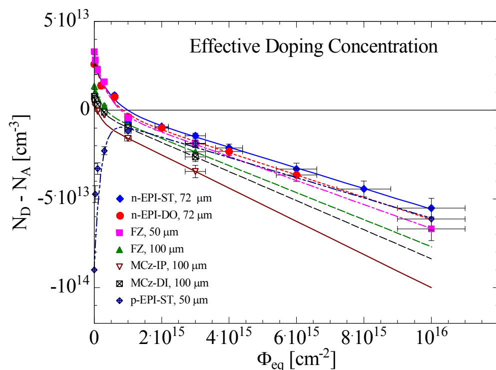

Fig. 7: Dependence of effective space charge on neutron fluence for different materials after completed beneficial annealing.

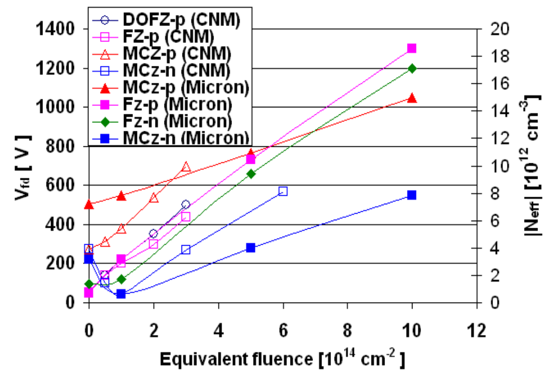

Fig. 8: Dependence of V_{fd} on fluence for different detectors (see legend) processed by various intitutions. The MCz-p,n detectors processed by Micron exhibit much smaller increase of V_{fd} with neutron fluence than seen before. The measurements were performed after completed beneficial annealing.

The measurements performed this year on 300 μm thick MCz detectors processed by Micron show a smaller stable damage ($g_c \sim 0.008$ cm^{-1} [30]) for n and p type silicon as can be seen in Fig. 8. The detectors were processed on the wafers for which previous measurements showed g_c~0.02 cm^{-1} ([31] CNM, [32] CiS, [33] IRST) and no difference between FZ/DOFZ/MCz materials [8]. This implies that the difference can be due to the process, but this needs further investigation.
No acceptor removal was observed after neutron irradiations [31, 33] in all materials, while donors are partially removed [8].

5.1.3 Reverse annealing

In the first approximation the long term annealing on the time scales of interest for SLHC is independent on the material [8,19,11,12,15,30,34,35,36] or irradiation particle. The acceptor activation is governed by the first order process with the introduction rate g_Y varying between 0.026 and 0.0048 cm^{-1} and the time constants of around 100 min at 80°C, depending on [O]. Significantly lower $g_Y = 1.6 \cdot 10^{-2}$ cm^{-1} was observed only in neutron irradiated epi-Si detectors [20].
In epitaxial detectors [14] the reverse annealing has also the second component (see Fig. 9,10) which obeys the second order kinetics. Recently, such a behavior was also seen in MCz [15], but further measurements are needed to establish defect dynamics. The time constant of the second component in epi-Si is however so large (>1000 min at 80°C) that is becomes irrelevant for SLHC. The introduction rate of the first (short) component tends to be smaller for MCz and Epi-Si detectors than for FZ detectors. Although in FZ and epitaxial detectors the same activation energy (Ea=1.3 eV) can be used to scale time constants measured to different temperatures there are some indications that for MCz detectors Ea=1.04 eV is smaller [15].

The reverse annealing amplitude ($N_{Y,1}$) was observed in some measurement to exhibit saturation at fluences >few 10^{15} cm^{-2} [28] in thin detectors (epi-Si, FZ and MCz). A similar observation at lower fluences was reported by RD48[8] for DOFZ detectors.

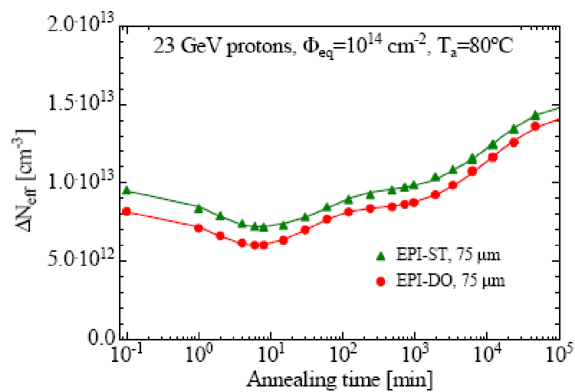

Figure 9: The annealing of N_{eff} for 75 μm thick epitaxial detectors.

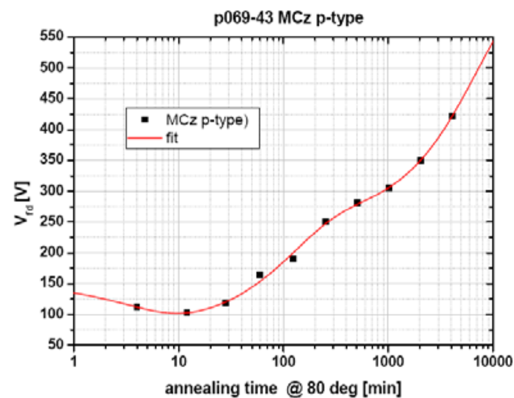

Figure 10: Annealing of MCz-p diode of standard thickness showing the second component in long term annealing.

5.1.4 Bias dependent damage

The V_{fd} depends strongly on the biasing condition during and after the irradiation. The details of the activation and deactivation of the bias dependent contribution to N_{eff} were reported in last year. Equally important is the additional damage caused by applied bias during the irradiation which was reported in Ref. [36], but needs verification with new detector grade materials.

5.1.5 Summary of results

The key parameters of the model for 24 GeV proton irradiated detectors are shown in Table 1.

	g_{eff}, g_c, β_{eq} [10^{-3} cm^{-1}]	g_Y [10^{-3} cm^{-1}]	τ_{ra} [min at 80°C]
DOFZ-n,p [8,12]	~6-10	50 (a)	~200
STFZ-n,p [8,12,35]	~10-20 (b)	45 to 65	>80
MCz-n [30,39,35,37,38]	-4 to -6.5	28 to 45	80 to 200
MCz-p [11,12,30,38]	~7-10 (e)	~28	100 to 500 (d)
Cz-n [34]	~-5	~30	~80
Epi-n [12,16,33,15,40]	-3 to -20 (c)	~30	~130
Epi-p [16,15,40]	-12 to -24 (c)	-	-

Table 1: Survey of damage parameters in different silicon materials after irradiation with 24 GeV protons.

(a) g_Y tends to saturate for DOFZ-n material at high fluences and may do so also in MCz. (b) The β_{eq} for STFZ-p type measured by [35] was found around 5 times lower than expected. Large variations between different STFZ materials were observed in the past also for STFZ-n type. (c) The introduction rate depends on thickness of the detector and on the process. (d) The huge difference in time constant reported in [11] is assumed to be related to thermal donors (e) Valid up to $\Phi_{eq}=10^{15}$ cm^{-2}. Blue denotes introduction of negative space charge while red of the positive.

5.2 Effective trapping times

Trapping of the drifting charge in the irradiated silicon detectors represents the limiting factor for their efficient use at highest SLHC fluences. The effective trapping probabilities are calculated as $1/\tau_{effe,h} = \beta_{e,h}(t, T)\cdot\Phi_{eq}$, where $\beta_{e,h}$ depends on time after irradiation and measurement temperature.

Particularly important in the last year were measurements of β at very high fluences. As the Charge Correction Method [41,42] can only be used for over-depleted detectors its applicability for detectors of standard thickness was limited to fluences up to 10^{15} cm^{-2}. A modified CCM was proposed [43] which can be performed on thin samples, but required also the simulation of the device. A state of the art TCT setup with significantly reduced rise time (<<1ns) enabled the measurements of time resolved pulses in 150 μm silicon detectors, and by that the use of CCM. The determination of effective trapping times of electrons (only front injection was possible) for epitaxial detectors irradiated up to $\Phi_{eq}=3\cdot10^{15}$ cm^{-2} is shown in Fig. 11 [16]. The measurements show that $\beta_{e,h}$ agrees well with previously determined although the uncertainty is relatively large.

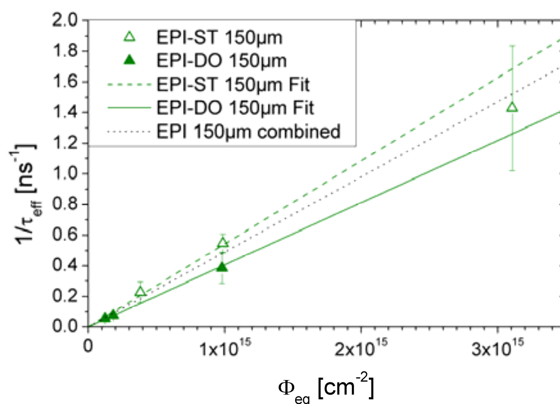

Figure 11: Effective trapping probabilities of electrons determined by CCM for 150 μm thick epitaxial detectors.

The values of effective trapping times damage constant from different groups [12,16,31,34,42-48] are gathered in the Table 2. The effective trapping times, within the error margins, don't depend on resistivity, [O], [C], wafer production (Cz, FZ, epi-Si) and type of silicon (p or n).

t_{min} , T = -10°C	β_h [10^{-16}cm^{-2}/ns]	β_e [10^{-16}cm^{-2}/ns]
Reactor neutrons	4.7± 1	3.5 ± 0.6
fast charged hadrons	6.6 ±1	5.3 ± 0.5

Table 2: Trapping time damage constants for neutron and fast charged hadron irradiated silicon detectors.

Simulations of CCE which use the effective trapping times as input systematically underestimate the measurements. As shown in the last report this remains true even if device model uncertainties related to the drift velocity, electric field parameterization and linear-field approximation could be excluded as the reason simply by setting $v_{dr} = v_{sat}$. One of the explanation can be a voltage-dependent τ_{eff} [16], detrapping effects, a velocity-dependent capture cross section or trap filling at high currents. In an improved model τ_{eff} should be better parameterized as electric-field dependent. A CCM should therefore be applied to certain voltage intervals to extract the voltage-dependent τ_{eff}.

5.2.1 Isochronal annealing of effective trapping times

The studies of isochronal annealing of effective trapping times were initiated to reveal the properties of underlying defects. It was observed that effective trapping times of electrons decrease at elevated temperatures of T>80°C [50]. This yeas a systematic study was performed [51] with annealing starting at 80°C with temperature increment of 20°C (30 min between the steps). The measurements for FZ detectors (Fig. 12a,b) show a decrease of electron trapping probability while the trapping probability of holes is not affected. The same behavior was confirmed for electron trapping probability in MCz detectors (Fig. 12c). On the other hand the effective trapping probability of holes shows an increase (Fig. 12d). A lot of effort is going on in WODEAN collaboration to correlate these measurements with measurements of defect properties by various techniques.

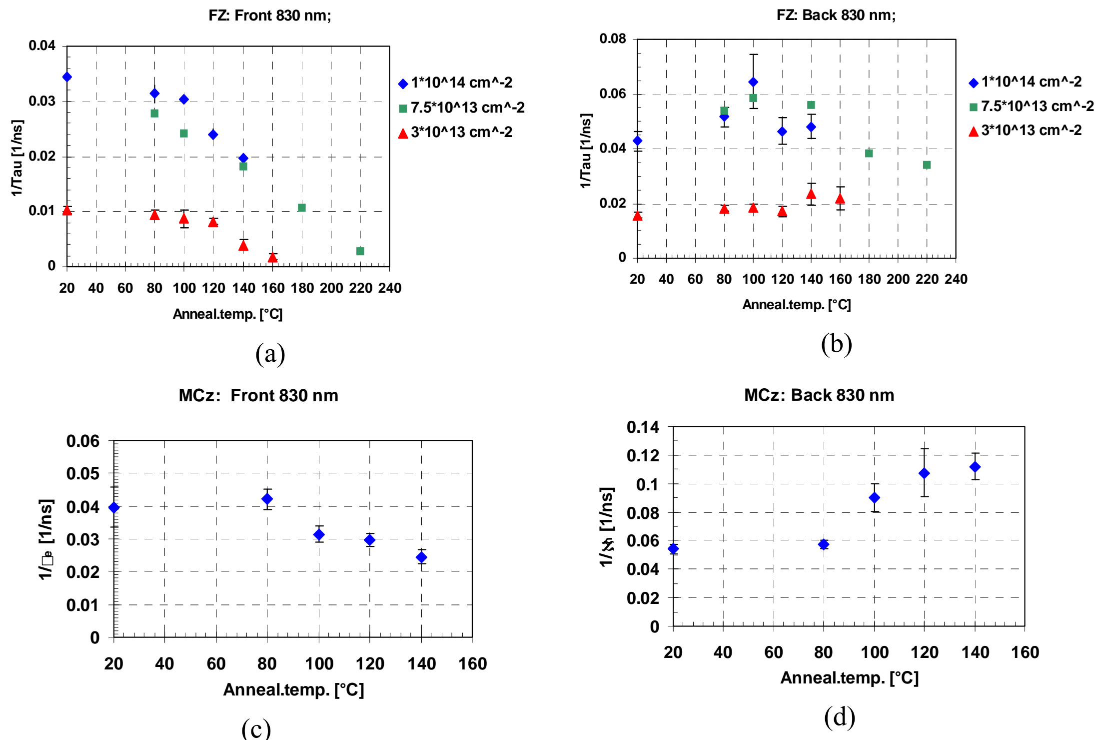

Figure 12: The effective trapping probability after isochronal annealing of diodes: (a) electrons - FZ, (b) holes - FZ, (c) electrons - MCz and (d) holes - MCz.

5.2.2 Annealing of trapping times

The effective trapping times annealing was studied in the past years and the conclusions can be found in last report.

5.3 Charge collection measurements

The collected charge depends on both electric field (hence N_{eff}) and on trapping probabilities. It is the most important parameter in characterization of any silicon particle detector. The measurement of charge collection were performed by different groups (CERN, IJS, SCIPP, Florence) using electrons from the ^{90}Sr source. The aim of measurements this year was to establish correlation between the onset of saturation of collected charge and V_{fd} measured by C-V, to determine the charge collection at 500 V and to establish the difference in charge collection for different irradiation particles. A systematic study on large set of samples processed on FZ and MCz wafers by Micron was conducted this year in order to answer these questions [13].

The measurements of effective trapping times have lead to conclusions that measured charge once the detector is highly over-depleted (V_{fd}<<V_{bias}) does not depend on the wafer properties (type, resistivity, oxygen concentration). The drift velocity approaches the saturation velocity in the entire thickness of detector; hence the carrier drift time becomes equal for all detectors. Under such conditions the loss of charge collection efficiency is entirely determined by effective trapping times. As shown in the last report the neutrons seem to be less damaging than 24 GeV protons at the same equivalent fluence, which was in accordance with effective trapping time measurements. It was on the other hand established that effective trapping times should be longer than measured by TCT as much as ~40%. Such a correction was needed for achieving reasonable agreement between simulation and measurements, both for neutron and 24 GeV proton irradiated detectors. This year the measurements were extended to 200 MeV pions and unlike in the previous year all the measurements were taken with LHC speed electronics. The most probable charge measured at bias voltages V_{bias}>V_{fd}+200 V (over-depletion) is shown in Fig. 13. There is no evident dependence on the material. On the other hand pion irradiated samples show lower CCE as neutron ones at the same equivalent fluence. Also measurements averaged for different diodes irradiated to the same equivalent fluence (shown in Fig. 14) confirm this observation. The difference between protons and pions is due to a single diode measurement at the highest proton fluence. The maximum collected charge decreases at the rate of ~600 e/10^{14} cm^{-2} for neutron irradiated samples and ~800 e/10^{14} cm^{-2} for pion irradiated samples.

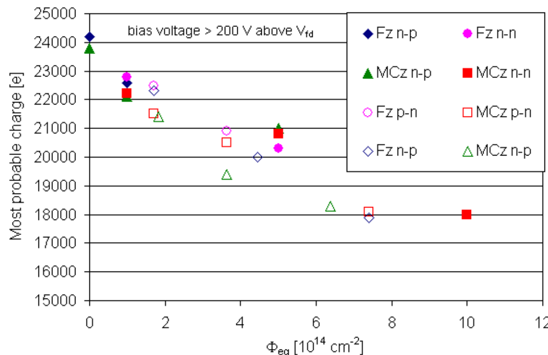

Figure 13: Charge induced in over-depleted pad detectors after neutron (solid markers) and 200 MeV pion irradiations (hardness factor 1.14) [13].

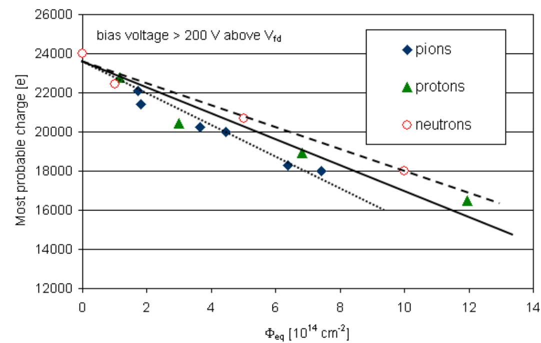

Figure 14: Measured charge in over-depleted detectors averaged over different materials irradiated to the same Φ_{eq} of reactor neutrons 200 MeV pions and 24 GeV protons [13].

With thin epitaxial detectors the studies of charge collection in over-depleted detectors can be extended up to the highest fluences at SLHC. A survey of measurements of detectors irradiated with 24 GeV protons and neutrons [23,40,51] is shown in Fig. 15. Note that, as for MCz-n detectors this is the worst point of operation for all charged hadron irradiated epitaxial detectors (as also for neutron 50 μm, 50 Ω cm).

There is a possibility that detector bias after upgrade will be limited to present value of 500 V. It is therefore reasonable to compare also the charge collection measurements at V_{bias}=500 V (see Fig. 16). The best performing detectors are those with lowest depletion voltage, mostly MCz. The best performing detectors at given fluence lay on the line with slope ≈ −1000 e/10^{14} cm^{-2}. Around 13000 e can be collected at 10^{15} cm^{-2}, which would yield a sufficient signal to noise ratio (S/N~12) with present electronics for short (few cm) strips.

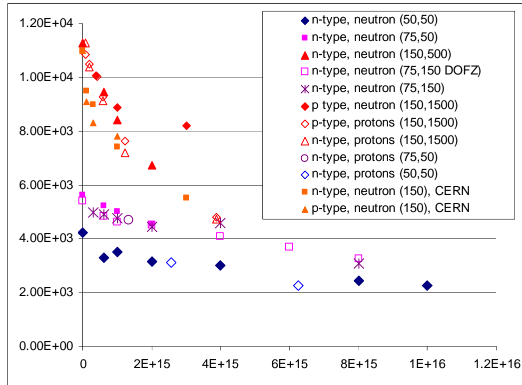

Figure 15: Most probable charge dependence on fluence for over-depleted Epi-Si detectors of different types; at each sample type, irradiation particles and in the brackets thickness and resistivity are given (taken after short term annealing).

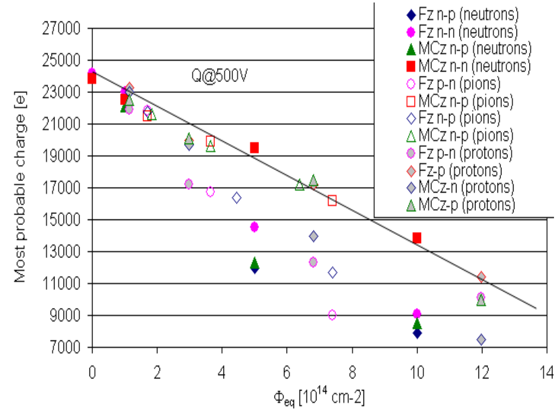

Figure 16: Most probable charge measured at 500 V in different diodes processed by Micron. The detector material and irradiation particle is given in the legend.

In last report it was shown that V_{fd} measured from C-V coincides with the onset of saturation in charge collection efficiency ($V_{fd,CCE}$ – see Fig. 17 for explanation) for neutron irradiated strip and pad detectors at fluences around 10^{15} cm^{-2}. For thin epitaxial detectors a good agreement wad demonstrated [51] over the whole SLHC fluence range. This year such correlation was established also for charged hadron irradiated detectors of standard thickness (see Fig. 18) which was found to be even better than for neutrons.

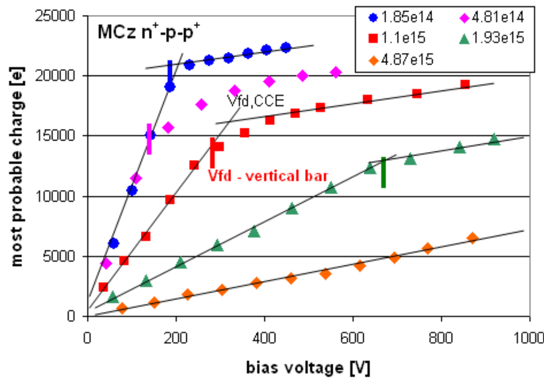

Figure 17: Dependence of charge collection on voltage for MCz-p detectors irradiated by 24 GeV protons (proton fluence given in legend). The determination of $V_{fd,CCE}$ and V_{fd} determined by C-V are indicated in the plot.

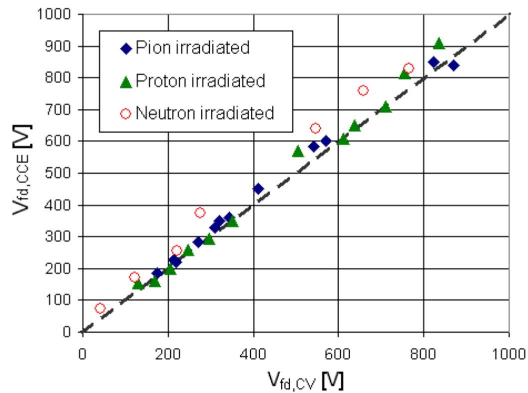

Figure 18: Correlation of V_{fd} and $V_{fd,CCE}$ measured on as set of neutron, 200 MeV pion and 24 GeV proton irradiated MCz and Fz pad detectors. The samples have been annealed for 80 min at 60°C.

Recent measurements with strip detectors (n^+ readout) at fluences beyond $2{\cdot}10^{15}$ cm^{-2} [52,53] point to device modeling different from that at lower fluences. Some measurements show CCE of almost 100% without showing onset of saturation. At very high voltages (up to 1900V!) the charge increases even more rapidly. The simulations could not reproduce the measured charge [53] even without trapping. One of the possible explanation is the onset of avalanche effects in the sensors, which happens at electric field strengths of >10 V/µm for electrons [54]. In strip geometry this condition is fulfilled sooner than in pad detectors, which might be the reason why up to recently such effect was not observed in diodes. However, recent measurements with 100 µm thick epitaxial pad detectors biased up to 700 V show similar behavior (see Fig. 19). Investigation of these effects will be one of the main objectives of the PDC working group in the following year

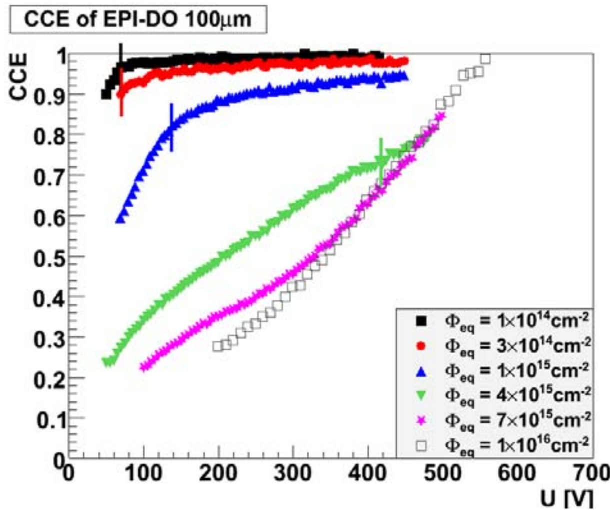

Figure 19: The charge collection efficiency for alpha particles measured after completed beneficial annealing.

5.4 Mixed irradiations

Detectors at LHC and SLHC will be exposed to different mixture of fast charged hadrons and neutrons with spectrum similar to reactor neutrons. The annealing behavior of MCz-n detectors indicates that positive space charge is introduced by irradiation with charged hadrons. As negative space charge is introduced by neutrons one expects compensation of space charge in mixed radiation field and consequent reduction of V_{fd}. Also the evolution of defects after irradiation may be different owing to different ratio of point defects and clusters. Therefore, it is not straightforward that damage produced by two different irradiation particles simply adds together. In order to check that a set of 200 MeV pion and 24 GeV proton samples irradiated up to $\Phi_{eq}=7\cdot10^{14}$ cm^{-2} [55] was irradiated with additional $\Phi_{eq}=2\cdot10^{14}$cm^{-2} neutrons. The CV, IV and CCE measurements were performed during annealing at 60°C and the properties were compared to control samples which were not irradiated with neutrons.

5.4.1 Leakage current

The leakage current scales with equivalent fluence as shown in Fig. 20. All diodes irradiated first by charged hadrons and then neutrons exhibit the increase of leakage current proportional to the equivalent fluence $\Phi_{eq} = \Phi_{eq,p,\pi} + \Phi_{eq,n}$ and compatible with $\alpha=4\cdot10^{-17}$ A/cm. Also annealing studies show acceptable agreement with the one expected for single particle irradiation.

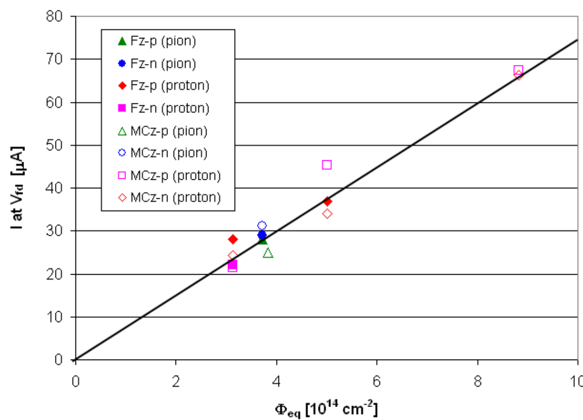

Figure 20: Dependence of leakage current on Φ_{eq} for mixed-irradiated samples after annealing of 80 min at 60°C. The solid line denotes the current expected for assumed $\alpha=4\cdot10^{-17}$ A/cm.

5.4.2 Full depletion voltage

The effective doping concentration was found to increase with increase of equivalent fluence for FZ detectors as it follows from equation

$$|N_{eff}| \sim |g_{c,p}\Phi_{eq,p} + g_{c,n}\Phi_{eq,n}|.$$

Similar $g_{c,p}$ and $g_{c,n}$ result in almost linear increase of the Neff with equivalent fluence as shown in Fig. 21a and denoted by arrows. The different sign of introduction rate of stable defects $g_{c,p}$, and $g_{c,n}$ leads to reduction of N_{eff} and by that the V_{fd} for MCz-n detectors (see Fig. 21b). The decrease of 140 V is compatible with expectations based on neutron only irradiated detectors, except for the pion irradiated samples which underwent dominant space charge sign inversion. The V_{fd} of MCz-p detectors also increases (see Fig. 21c), however at high fluence the increase of 80 V is significantly smaller than expected ~150 V after additional $\Phi_{eq,n} = 2{\cdot}10^{14}$ cm^{-2}. This can be explained by the strong polarization of detectors ("double junction") at high fluences where the balance of positive and negative space charge regions starts turning in favor of positive space charge. The observation is in agreement with TCT measurements [17]. An ideal detector would therefore be MCz-n detector readout at n^+ side which is placed in the irradiation field where the space charge is ideally compensated. A similar experiment was conducted in Ref. [55] for strip detectors with reversed order of irradiation (neutrons first) and showed the same behavior.

Long term annealing of mixed irradiated samples confirms the above conclusions. Moreover the change of V_{fd} before (for convenience denoted by t=0.1 min) and immediately after (denoted by t=1 min) irradiation clearly points to dominant space charge in the MCz-n detector. For the two highest proton fluences the V_{fd} decreases and then shows the behavior typical for detector with predominately positive space charge. Although the V_{fd} of MCz-p detectors increases the increase is smaller than for FZ (see Fig. 19). Also long term annealing of MCz detectors is delayed. The fit of Hamburg model to the mixed irradiated FZ detectors gives introduction rate of g_Y=0.054 cm^{-1} and time constants of around 1000 min which is in agreement with single particle irradiations and previous data on the FZ detectors. This implies that long term annealing scales with equivalent fluence.

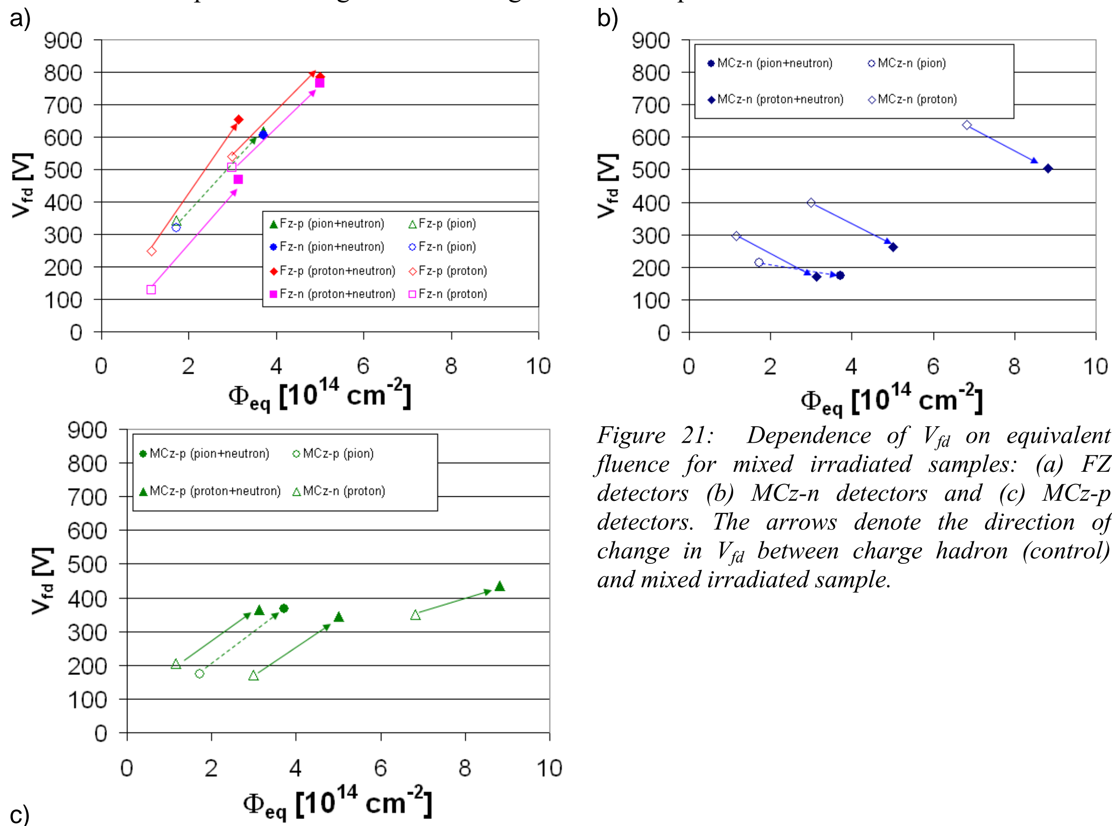

Figure 21: Dependence of V_{fd} on equivalent fluence for mixed irradiated samples: (a) FZ detectors (b) MCz-n detectors and (c) MCz-p detectors. The arrows denote the direction of change in V_{fd} between charge hadron (control) and mixed irradiated sample.

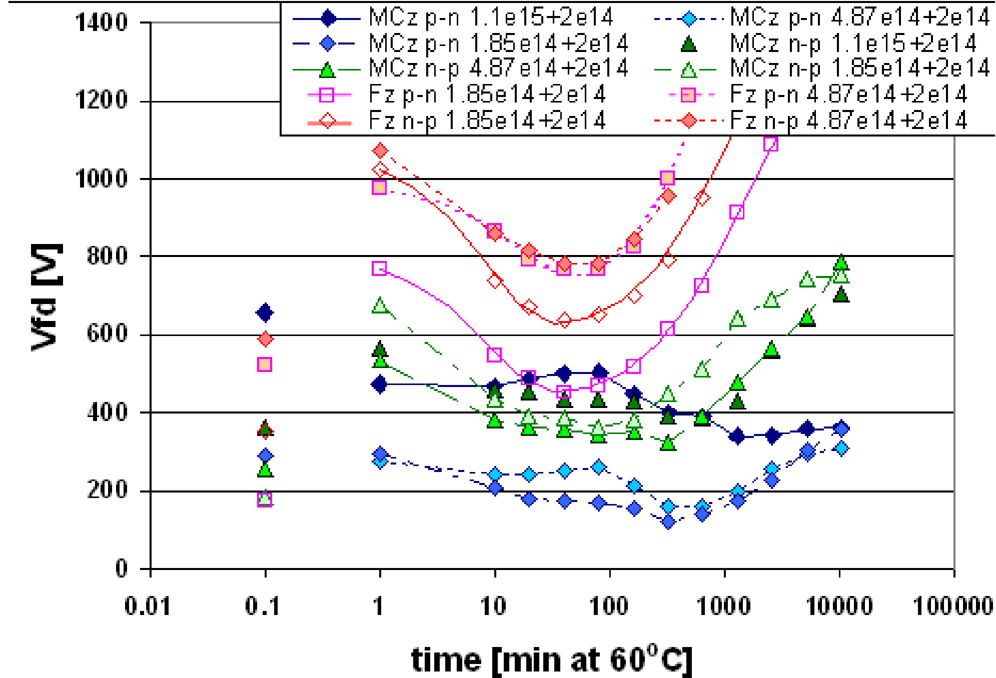

Figure 22: The evolution of V_{fd} of mixed (proton + neutron) irradiated detectors during long term annealing. The V_{fd} > 1000 V are obtained by extrapolation of C-V curve to geometric capacitance and not directly from fit. The fluence and material type are given in the brackets.

5.4.3 Charge collection measurements

The charge collection measurements were performed on the mixed irradiated samples at different points during annealing. The $V_{fd,cce}$ at different annealing times agrees well with V_{fd} from CV as illustrated in Fig.20. The beneficial effect of additional neutron irradiation can be seen in Fig. 23a where up to 5000 min at 60°C the CCE is better for mixed than for equivalent sample irradiated only with protons. Also long term annealing is not very harmful for MCz-p detectors. The V_{fd} and consequently CCE of MCz diodes irradiated to $\Phi_{eq}=8.9\cdot10^{14}$ cm^{-2} with a mix corresponding to r=10 cm at SLHC were during the entire annealing at 60°C at levels enabling successful operation already at 500 V.

Annealing does not alter charge at $V>>V_{fd}$, which can be explained by compensations of an increase and a decrease of effective trapping probability of holes and electrons, which is also in agreement with assumption that the effective trapping probabilities are additive.

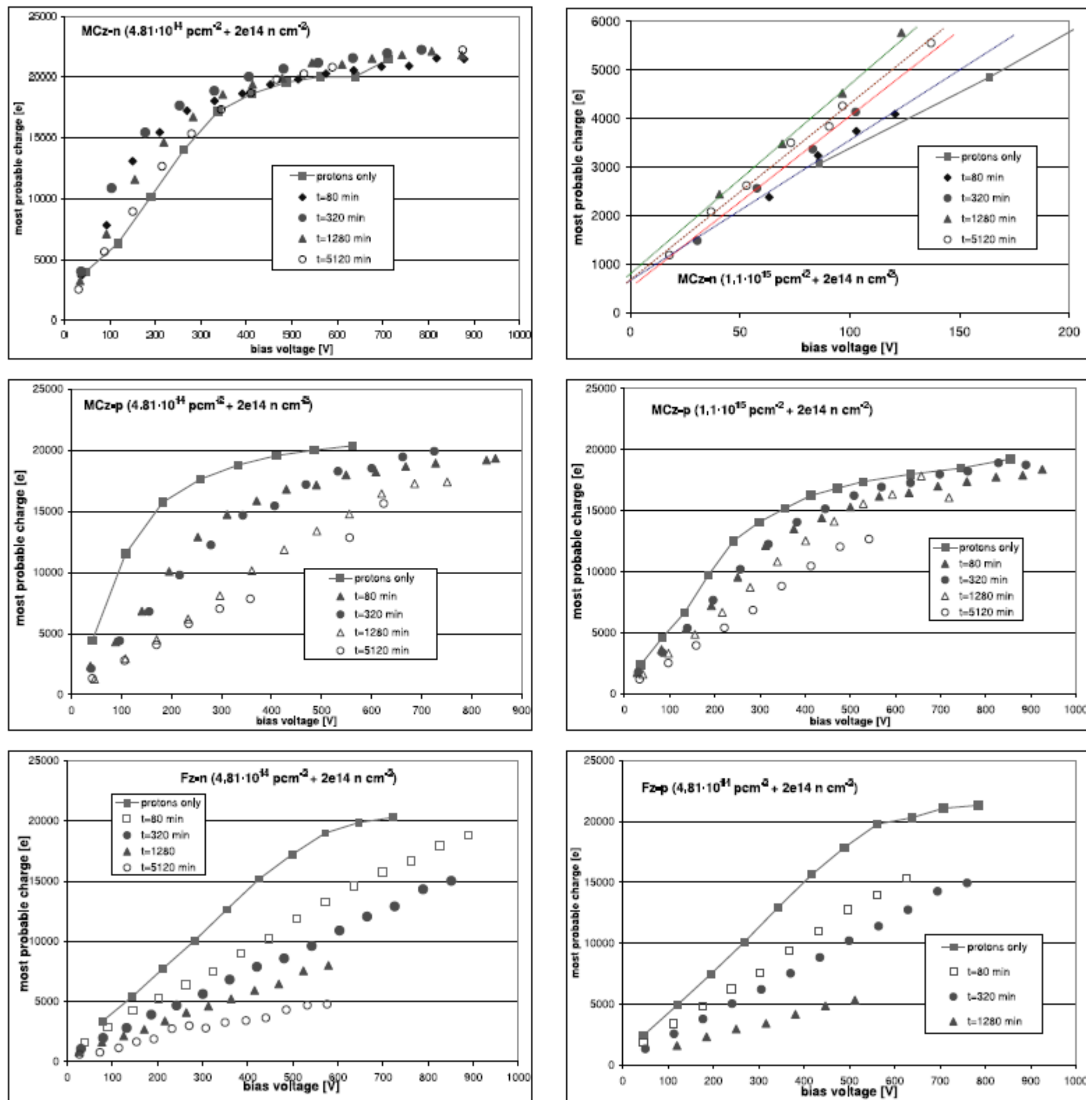

Figure 23: The dependence of most probable charge for different mixed irradiated detectors at different annealing stages. The measurements for proton only irradiated detector are connected by lines. Note that for the MCz-n samples irradiated to highest fluence broke close at the guard ring region. The measurements were possible only up to ~200V before it started to show break-down.

REFERENCES

[1] M. Moll, Ph.D. Thesis, Hamburg University, 1999, DESY THESIS 1999-040, ISSN-1435-8085.

[2] E. Verbitskaya, V. Eremin, A. Macchiolo, "First results on electric field distribution in irradiated epi-Si detectors", pres. 11 RD50 Workshop, Nov 12-14, 2007, CERN.

[3] E. Verbitskaya et al., Nucl. Instr. and Meth. A 557 (2006) 528-539.

[4] E. Verbitskaya et al., Nucl. Instr. and Meth. A583 (2007) 77.

[5] V. Eremin, "Recent results on electric field distribution in SMART irradiated detectors on MCZ and epitaxial silicon", pres. 9 RD50 Workshop, Oct 16-18, 2006, CERN.

[6] G. Lindström, private communciations.

[7] E. Fretwurst et al., Nucl. Instr. and Meth. A552 (2005) 124.

[8] G. Lindström et al., Nucl. Instr. and Meth. A466 (2001) 308.

[9] CERN-LHCC-2004-031 and LHCC-RD-005, RD50 Status Report 2004.

[10] CERN-LHCC-2005-037 and LHCC-RD-009, RD50 Status Report 2005
[11] H. Hödelmoser et al, ., Nucl. Instr. and Meth. A583 (2007) 64.
[12] V. Cindro et al, "P-type Silicon irradiated with 24 GeV/c protons", presented at 10th RD50 Workshop, Vilnius, June, 2007.
[13] G. Kramberger et al*., "Charge collection measurements on MICRON RD50 strip detectors and diodes irradiated with protons, pions"*, presented at 12th RD50 Workshop, Ljubljana, June, 2008.
[14] D. Eckstein et al.," *Comparison of proton damage in thin FZ, MCz and epitaxial silicon detectors*", presented at 12th RD50 Workshop, Ljubljana, June, 2008.
[15] K. Kaska et al.,"*Annealing studies on MCz after 23 GeV proton irradiation and CCE of 150um epitaxial silicon devices*", presented at 12th RD50 Workshop, Ljubljana, June, 2008.
[16] J. Lange et al.,"", presented at 13th RD50 Workshop, CERN, November, 2008.
[17] D. Creanza et al.,"*On MCz SCSI after 24 GeV/c proton irradiation*", presented at 10th RD50 Workshop, Ljubljana, June, 2008.
[18] K. Kaska et al.,"*TCT measurements on MCz n- and p-type after proton and neutron irradiation*", presented at 13th RD50 Workshop, CERN, November, 2008.
[19] G. Lindstr¨om et al., Nucl. Instr. and Meth. A556 (2006) 451.
[20] E. Fretwurst et al.,"*Radiation tolerant epitaxial silicon detectors*", presented at 6th RD50 Workshop, Helsinki, June, 2005.
[21] E. Fretwurst et al., Nucl. Instr. and Meth. A514 (2003) 1.
[22] Y.J. Lee et al., Phys. Rev. B 65 (2002) 085205-1-12.
[23] K. Kaska et al.,"*Epitaxial silicon detectors irradiated with protons and neutrons* ", presented at 11th RD50 Workshop, CERN, November, 2007
[24] E. Fretwurst et al.,"First results on 24 GeV/c proton irradiated thin silicon detectors", presented at 11th RD50 Workshop, CERN, November, 2007.
[25] E. Fretwurst at al., . Instr. and Meth. A552 (2005) 124.
[26] G. Lindström et al., Nucl. Instr. and Meth. A568 (2006) 66.
[27] M. Bruzzi et al., Nucl. Instr. and Meth. A 552 (2005) 20.
[28] E. Fretwurst et al.,"Comparison of neutron damage in thin FZ, MCz and epitaxial silicon detectors", presented at 10th RD50 Workshop, Vilnius, June, 2007.
[29] G. Kramberger et al.,"CCE measurements with Epi-Si detectors", presented at 8th RD50 Workshop, Prague, June, 2006.
[30] G. Kramberger et al.,"*Charge collection measurements on MICRON RD50 detectors*", ATLAS ID upgrade Workshop, Valencia, 2007.
[31] V. Cindro et al.,"Trapping of Electrons and Holes in p type Silicon Irradiated with Neutrons", presented at IEEE NSS-MIC Symposium, San Diego, October, 2006.
[32] E. Fretwurst et al., Instr. and Meth. A583 (2007) 58.
[33] N. Manna et al., "Study of radiation damage induced by protons and neutrons on heavily irradiated Magnetic Czochralski and Epitaxial silicon detectors", presented at 8th RD50 Workshop, Prague, June 2006.
[34] E. Fretwurst et al., "Survey of radiation damage studies at Hamburg ", presented at 3*rd* CERN-RD50 Workshop, CERN, November, 2003.
[35] G. Pellegrini et al., Meth. Instr. and Meth. A552 (2005) 27.
[36] G. Kramberger et al., Nucl. Instr. and Meth. A450 (2000) 288.
[37] J. Harkönen et al., Nucl. Instr. and Meth. A552 (2005) 43.
[38] G. Segneri, et al., Nucl. Instr. and Meth. A573 (2007) 283.
[39] N.Manna et al., Nucl. Instr. and Meth. A583 (2007) 87.
[40] V. Khomenkov et al., "Radiation Tolerance of Epitaxial Silicon after Fast Hadron Irradiaion", presented at IEEE NSS-MIC, Dresden, October 2008.
[41] G. Kramberger et al., Nucl. Instr. and Meth. A476 (2002) 645.
[42] T.J. Brodbeck et al., Nucl. Instr. and Meth. A455 (2000) 645.
[43] J. Weber et al.,"Determinaton of Traping Time Constants in Neutron Irradiated Thin Epitaxial Pad Detectros", presented at 11th RD50 Workshop, CERN, November, 2007.
[44] J. Weber et al., IEEE Trans. NS 54(6) (2007) 2701.
[45] A. Bates and M. Moll, Nucl. Instr. and Meth. A 555 (2005) 113-124.
[46] O. Krasel et al., IEEE Trans. NS 51(1) (2004) 3055.
[47] G. Kramberger et al., Nucl. Instr. and Meth. A 481 (2002) 297-305.
[48] T. Lari et al., Nucl. Instr. and Meth. A 518 (2004) 349.
[49] G. Kramberger et al., "Effective trapping times after isochronal annealing«, presented at the 2-nd WODEAN workshop, Vilnius, June 2007.

[50] M. K. Bock et al.," *Charge Carrier Trapping in FZ, MCz and Epi Silicon Diodes after Hadron Irradiation*", presented at IEEE NSS-MIC, Dresden, October 2008.
[51] G. Kramberger et al., , Nucl. Instr. and Meth. A 554 (2005) 212.
[52] G. L. Casse et al.,"Radiation Hardness of p-type detectors", Presented at 7th RESMDD Conference, Florence, 2008.
[53] I. Mandić at al.*," Observation of full charge collection efficiency in n+p strip detectors irradiated up to* $3x10^{15}$ *n/cm*^{2}", Presented at 7th RESMDD Conference, Florence, 2008.
[54] C. A. Lee et al., Phys. Rev. 143-3A (1964) A761.
[55] G. Krambeger et al.*,"C-V/I-V and CCE measurements of MCz and FZ p and n type diodes after mixed irradiations"*, presented at 12th RD50 Workshop, Ljubljana, June, 2008.
[55] T. Affolder at al., " *Charge Collection, Power, and Annealing Behaviour of Planar Silicon Detectors after Reactor Neutron, Pion and Proton Doses up to 1.6×1016* n_{eq} *cm*$^{-2}$",presented at 13th RD50 Workshop, CERN, November, 2008.

6 New Structures

The past year has been a successful year for the new structures working group of RD50. The thin detectors sub-section progresses towards segmented detectors fabricated on epitaxial and SOI wafers, with the fabrication of strip and ATLAS pixel sensors currently being performed in MPI and Industry. Test structures to prove the isolation of features on the n-side of the wafer, using homogenous and moderate p-spray techniques, have been performed and irradiated. The interstrip capacitance and resistance remain acceptable up to the tested dose of 1 MRad. The 3D detector section has seen the full characterization of the single-type column detectors produced at FBK, including the final paper on the 2007 CERN testbeam, which demonstrated the incomplete charge collection due to ballistic deficit and the detection efficiency as a function of position of the incident beam across the detector's surface. Double-sided 3D devices have now been fabricated by both FBK and CNM-IMB and results from those from CNM-IMB operating as pixel and strip detectors are shown, including charge collection after irradiation. A testbeam has taken place with double-sided detectors from both FBK and CNM-IMB in 2008 and the analysis is on going. Extensive simulation work at Valencia and Ioffe is also reported.

6.1 Thin Detectors

This research line investigates the properties of thin planar detectors for extremely high radiation fluences (> 10^{15} 1 MeV n_{eq} cm^{-2}). The main advantage of such devices would be the radiation tolerance, i.e. low depletion voltage and higher collection efficiency, especially at low operation voltages due to the small depleted volume, compared to standard thick (300 µm) devices. The active thickness can be adjusted to the expected fluence which depends on the radial distance from the interaction point. This would also results in a positive effect on the material budget. The thin detectors will have n-type segmented implants to keep the highest electrical field under the readout implant throughout the lifetime of the device. The aim of this program is to determine the optimal thickness, the type and technology for planar detectors to be used at fluences between 10^{15} and 10^{16} 1 MeV n_{eq} cm^{-2}.

The R&D focuses on two technologies to build thin detectors. The first method is based on the success of fabricating pad diodes on thin epitaxial material that was reported in [1] and [2]. The second method exploits the wafer bonding technology for the production of thin detectors [3]. Wafer bonding technology is know as SOI (silicon on insulator) as it involves a detector grade wafer, already backside processed and oxidized, being bonded onto a low resistivity handle wafer; resulting in a silicon detector-insulator-silicon substrate stack. The detector wafer is then thinned to the desired thickness. The stack of handling wafer and thinned detector wafer is processed like a normal wafer to form the detector. Finally the handle wafer is removed using wet chemical etching.

In the case of the epitaxial material the wafers can also be processed on standard equipment in commercial detector facilities.

The epitaxial devices for this research are being processed at CIS, (Erfurt, Germany), whereas the SOI structures are produced as a joint venture between industry and the Semiconductor Laboratory of the Max-Planck-Institut. The research is being pursued via the fabrication of test devices produced on the following substrate types and thicknesses:

a) Epitaxial: 50 µm, 75 µm, 150 µm (all n-in-p)
b) SOI: 75 µm (n-in-n), 75 µm and 150 µm (n-in-p)

In both productions a set of microstrip detectors, with 7.6 mm long strips, with identical designs has been inserted. The inter-strip isolation techniques implemented are a homogenous p-spray and an optional moderated p-spray, where the profile of the p-spray implantation is modulated through an opening of the nitride layer [4]. The parameters of the microstrip devices are listed in Table 1.

Strip Pitch (μm)	n^+ implantation width (μm)	p-spray moderation width (μm)
50	30	10
50	30	None
80	30	10
80	30	None
50	24	10
50	30	6
50	36	6
80	20	None
80	20	24
80	30	24

Table 1 Design variations of the microstrip detectors in the epitaxial and SOI productions

In the SOI wafers, 10 pixel structures compatible with the FE-I3 ATLAS ASIC are included together with smaller pixel matrices (active area of 0.5 x 2.0 mm^2) designed for charge sharing studies. The pixel sensors differ from the standard ATLAS design with respect to a guard-ring structure, needed in the case of n-in-p devices, that is added on the front side.

The SOI wafers had a starting thickness of 300 μm, with a bulk resistivity of 360 Ωcm for the n-type and 5 kΩcm for the p-type silicon. The back-side implantation has been performed before the bonding to the handle wafer and the thinning of the active wafer. These two last steps have been carried out by industry (Soitec, France), where the thinning process has already been proven to work with diodes produced on n-type FZ silicon.

The two productions are at the moment at a similar stage where the thin thermal oxide and the nitride layers, needed for the p-spray implantation, are being grown.

To optimize the p-spray dose required to isolate the strips and the pixels in n-in-p and n-in-n devices a test has been performed with microstrip detectors of the same design as the ones implemented in the two productions of thin detectors. These sensors have been fabricated in a pre-production run by CIS on p-type FZ wafers, with <100> crystal orientation, a thickness of 300 μm and a resistivity of 10 kΩcm. The integrated dose of the p-spray implantation in the moderated region or for the homogenous p-spray has been calculated to be around 7.5 x 10^{11} cm^{-2}. The integrated p-spray dose in the non-moderated region is 4.2 x 10^{12} cm^{-2}. Two microstrip detectors, of 80 μm pitch, have been electrically characterized and afterwards they have undergone irradiation at the Karlsruhe X-Ray irradiation facility up to a dose of 1 MRad. The integrated dose levels for the SLHC are expected to exceed 100 MRad close to the collision region, while effects at the $Si\text{-}SiO_2$ interface have been shown to saturate at the 100 kRad level [5].

The inter-strip capacitance has been continuously monitored during the irradiation. It has been measured at a frequency of 1 MHz and with a bias voltage of 40 V. The results are shown in Fig 1. Depending on the strip isolation method, the saturation of C_{int} as a function of the dose is reached between 70 and 300 kRad. Fig 2 shows the capacitance and Fig 3 the inter-strip resistance, measured as a function of bias voltage before and after irradiation, after one week of annealing at room temperature. The figures show results for microstrip sensors with (a) moderated and (b) homogenous p-spray isolation. R_{int} decreases after a dose of 1 MRad from values around 30-40 GΩ to about 5-7 GΩ, still high enough to ensure isolation between the strips.

The IV curves, as shown in Fig.4, show a lower breakdown voltage after irradiation, contrary to what was reported previously (see for example [6]). Measurements performed with a probe-station equipped with a CCD camera (Hamamatsu Phemos 1000) have detected hot spots in the strip punch-through region. Further X-ray irradiations are foreseen to fully understand the cause of the sensors behaviour in terms of breakdown voltages.

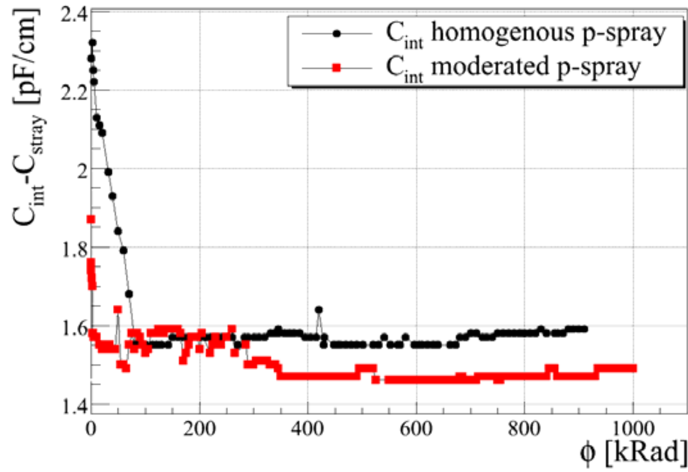

Fig 1 Inter-strip capacitance measured in two microstrip sensors during the X-ray irradiation.

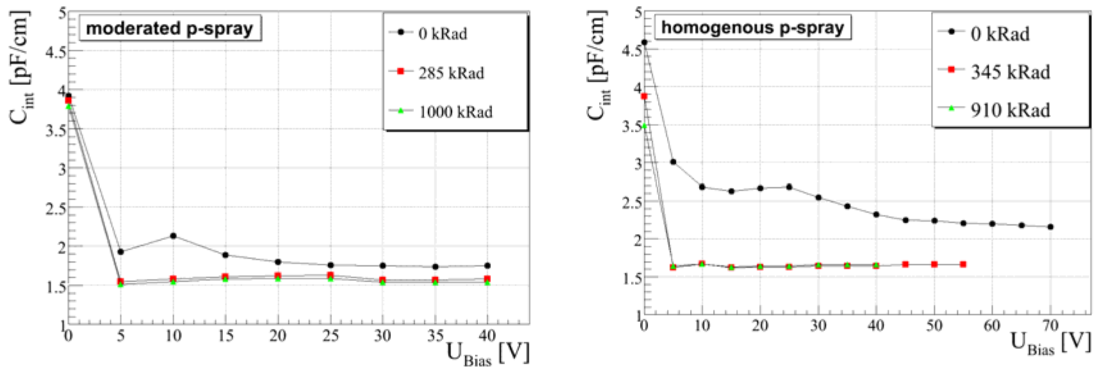

Fig 2 Capacitance measured as a function of bias voltage at different irradiation steps for microstrip sensors where the chosen isolation method is (a) moderated p-spray and (b) homogenous p-spray.

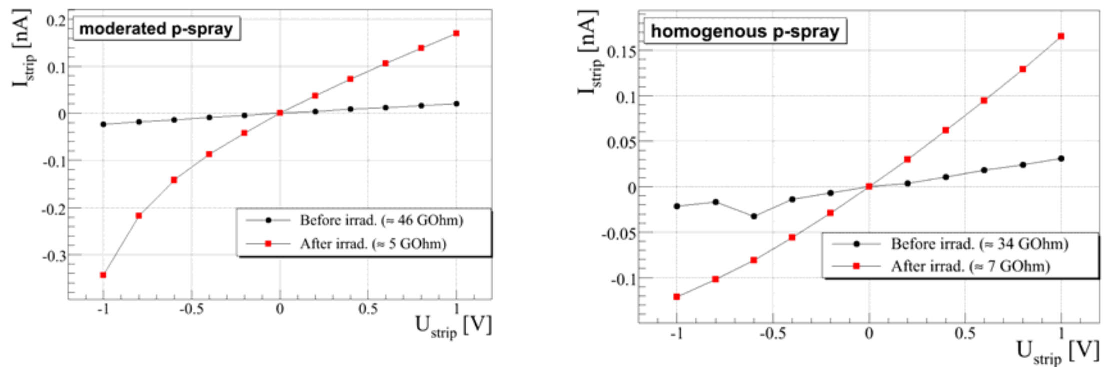

Fig 3 Inter-strip current measured before and after X-ray irradiation in the microstrip sensors where the chosen isolation method is (a) moderated p-spray and (b) homogenous p-spray.

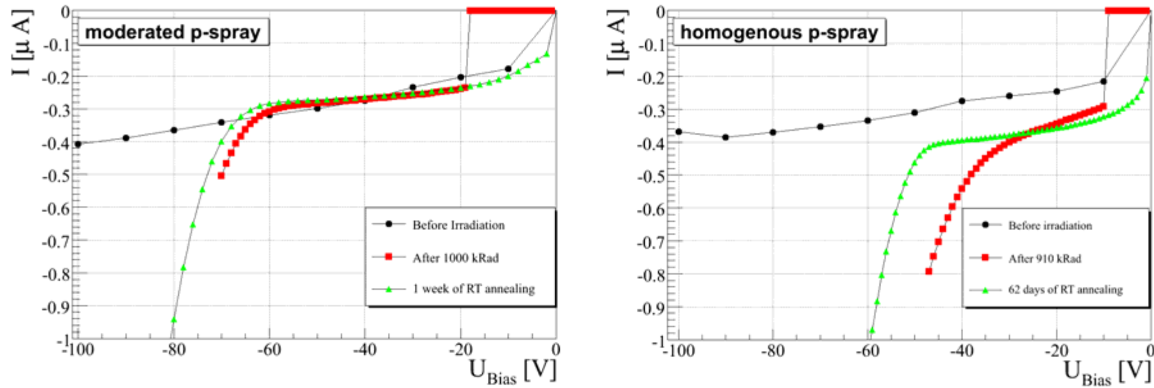

Fig 4 IV curves measured before and after irradiation in the microstrip sensors where the chosen isolation method is (a) moderated p-spray and (b) homogenous p-spray

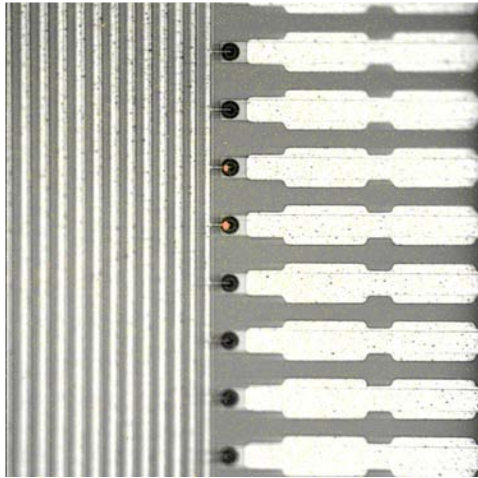

Fig 5 Measurements of the microstrip sensor with a homogenous p-spray after irradiation with the Hamamatsu PHEMOS 1000 system. Hot spots are visible in the strip punch-through region.

6.2 3D Detectors

The work on 3D detectors since the last status report has been split between the fabrication and extensive characterization of double-sided 3D detectors fabricated at CNM-IMB and FBK, and the completion of the characterization of the single-type column 3D detectors, (3D-stc), produced by FBK in 2005. This status report reflects this effort and discusses the characterization of the 3D-stc devices first followed by the work on the double-sided devices at the fabrication institutes and their characterization by RD50 collaborators.

6.2.1 FBK-irst Single-Type Column 3D Detectors

In 2005 FBK-irst, (then know as ITC-irst), proposed the 3D-stc detector concept [7] as a simplified 3D detector design and as a first stage in the production of full 3D detectors. All the columnar electrodes are of the same type (n^+) and are etched from the front side of a p-type wafer; p-stops or p-spray are used for surface isolation. On the back side a blank p^+ implant provides a uniform ohmic contact. The columns are empty and do not penetrate all through the substrate. Three batches of 3D-stc detectors with the same mask layout were fabricated at FBK-irst on high-resistivity p-type wafers [8] and [9].

Samples of pad and strip detectors from the three 3D-stc batches, produced at FBK-irst, were delivered to some RD50 collaborators to perform functional tests which were reported in the 2007 RD50 status report [10]. The charge collection tests of strip devices performed in the laboratory with a laser and a Sr-90 beta source at Freiburg in conjunction with Trento and FBK-irst, reported last year, have been presented at the IEEE NSS and published [11]. These results demonstrate the charge collection of single-type column 3D detectors with front-end electronics operating at LHC speed shaping times (20 ns). With this shaping time a ballistic deficit is observed in the collected charge due to the low field regions in the device. However, after irradiation by 26 MeV protons to an equivalent fluence of 9.1 x 10^{14} 1 MeV n_{eq} cm^{-2} the detectors are still operational and do not exhibit any degradation in collected charge once full lateral depletion is attained (2.14 fC, 14000 electrons after irradiation compared to 2.0 fC, 13000 electrons before irradiation). The full depletion voltage increased from 80 V to 450 V. Such an effect is due to the short collection distances compared to the effective charge drift distance of 200 μm after the irradiation dose. For comparison a 300 μm planar device irradiated to a similar fluence (1.6 x 10^{15} 1 MeV n_{eq} cm^{-2}) requires in excess of 700 V to obtain the same charge.

A non-irradiated single-type column short strip detector has also been tested in a high energy pion beams at CERN by the Glasgow, Freiburg, FBK-irst and Trento groups. The purpose of the beam measurements was to study with high position resolution the charge collection and hit detection efficiency with respect to the point of impact of the beam particles. The testbeam, in October 2007, was performed in collaboration ATLAS 3D pixel upgrade collaboration. The analysis of the 2007 testbeam in now finished and in the process of being published [12] and [13].

The 2007 testbeam used an un-irradiated single-type column 3D detector fabricated at FBK-IRST from a 300 μm thick p-type magnetic Czochralski wafer with an integrated de-coupling capacitor. The strips were formed from n^+-type 150 μm deep holes connected together with a p-spray inter-strip isolation. The strips were connected to an LHCb Beetle amplifier chip [14] mounted on an LHCb inner tracker hybrid [15]. The Beetle chip has a 40 MHz analogue output with a 22 ns shaping time. This allows the collected charge to be measured directly, additionally with the use of a delay between the trigger and the sample point the shape of the signal can be obtained. The measurements were carried out with a 180 GeV pion beam at the CERN SPS. To determining the pion tracks the Bonn ATLAS telescope [16] was used. It consists of four telescope modules each with a pair of crossed planar silicon strip detectors with a strip pitch of 50 μm. The device under test was positioned such that two telescope modules were either side of it. The readout is triggered by two scintillators, one on either side of the telescope, in coincidence, a third scintillator with a circular hole of 1.5 cm diameter served as a veto on tracks outside the sensitive area of the test devices. Since one of the telescope modules was not working properly the resolution of the point of incidence of a pion on the test sensor is expected to be larger than the nominal 5 μm.

Using analogue readout the full pulse shape formed by the Beetle front-end ASIC could be measured for different bias voltages. The average pulses from the hit strip were measured for 40 V, 60 V and 80 V bias and for a fully depleted reference planar detector of the same thickness (300 μm), which are illustrated in Fig 6. The 3D-stc sensor is depleted laterally between the columns at 40 V bias and for higher voltages depletes to its backside, like a planar device, until full depletion is reached between 60 V and 80 V. Since for lateral depletion only half the substrate thickness contributes to charge generation the pulse maximum is significantly lower at 40 V than at higher biases. At a bias of 40 V the lower electric field, and therefore slower drift of the charge carriers, results in the signal of the 3D-stc sensor peaking approximately 1.4 ns later than when fully depleted at 80 V. Fig 7 shows the signal behaviour of the strips adjacent to the hit strip at 40 V. Unless a particle traverses the detector in the centre between two strips, there is one of the two strips, (the hit strip), closer to the point of incidence than the other. The horizontal drift of the generated electrons to the closest column on the hit strip as well as of the holes to the low field region induce a fast signal of opposite polarity on the closest neighbouring strip. The following increase of the signal is caused by the slow vertical drift of the holes to the back plane. For lateral depletion the net signal integrated over the full pulse should be zero on the neighbour strips since no charge is collected. This lack of a charge sharing effect is inherent to the 3D design. For a 3D-stc detector, however, this is only true as long as the planar part underneath the columns does not contribute to the signal. The slight asymmetry for positive ADC values in Fig 7 indicates that the depleted zone has already grown a little bit below the

columns at 40 V bias. The impact of charge sharing can be expected to be stronger at higher bias voltages; that is, greater depletion in the planar part. However the signal amplitude on the adjacent strips was measured to be very low and not distinguished from the noise. Thus, unlike for planar detectors, the charge sharing effect can not contribute to an improvement of the intrinsic position resolution by strip clustering. On the other hand, for low signal-to-noise ratios, for example after irradiation, it is an advantage when the signal is not further diminished by charge sharing, especially if a binary readout with a high signal threshold is employed as in the current ATLAS Semiconductor Tracker.

Bias Voltage (V)	Noise	Collected charge	Charge collection efficiency (%)	SNR
40	1.42 ke$^-$ 0.25 fC	10.49 ± 0.06 ke$^-$ 1.67 ± 0.01 fC	48	7.4
60	1.21 ke$^-$ 0.19 fC	13.39 ± 0.06 ke$^-$ 2.13 ± 0.01 fC	61	11.1
80	1.17 ke$^-$ 0.19 fC	15.46 ± 0.06 ke$^-$ 2.46 ± 0.01 fC	70	13.2

Table 2 Noise, signal, charge collection efficiency and signal-to-noise for the 3D-stc for different bias voltages.

As the height of the signal is proportional to the collected charge, the ADC values of the peak were histogrammed and fitted with a convolution of a Landau function (signal formation) and Gaussian function (noise). A calibration factor, calculated from the planar reference detector, was applied to obtain the values for the collected charge given in Table 2. The low charge collection due to ballistic deficit because of the slow drift of the electrons and holes in the low field region between the columns was observed. Since all columns are of same doping type and polarity the field in this region remains low even for high bias voltages. Table 2 also contains the noise measured for the different bias voltages. The noise of the unirradiated detector is dominated by the capacitance, as demonstrated in laboratory tests ([11], [17]), which decreases steeply during lateral depletion between columns, followed by a slower decrease when the detector depletes to the backside. The value of the noise drops from 1.42 ke$^-$ (0.25 fC) at 40 V bias to 1.17 ke$^-$ (0.19 fC) at 80 V. With the opposing trends in the behaviour of noise and signal an increasing signal-to-noise ratio (SNR) was achieved for higher bias voltages. For the fully depleted sensor at 80 V the SNR is approximately 13.

Due to columnar holes in the substrate material and the field configuration, the hit efficiency of a 3D-stc sensor is expected to be non-homogeneous across the detector's surface. This behaviour is known from simulations [7] and has been verified with position resolved infrared laser measurements [17]. Efficiency measurements were performed for the detector biased at 40 V and with a signal cut of 1 fC which corresponds to a SNR of 4. Fig 8 illustrates the strip detector with three strips each with three columns and the repeated unit cell of the detector. In order to reduce the statistical errors, the periodic structure has been used to superimpose the hits from the selected area for all strips. The structures of the sensors detection efficiency is shown in the two-dimensional efficiency map given in Fig 9. An efficiency drop of more than 10 % can be observed at the centre of a column, as expected because when a particle passes through the hollow column no charge will be generated until it reaches the region underneath the columns, therefore producing a lower signal and consequentially lower detection efficiency. In addition to the dip at the columns a decrease of the efficiency towards the middle between two strips at a distance of 40 μm (along the y-axis) from the centre can be seen. A particle passing through the detector in that region will create charge over the whole depth of the depleted bulk but due to the low field, full signal will not be induced at the electrodes during the 22 ns shaping time. The 5 × 5 μm binning is finer than the actual track resolution leading to slightly washed out area around the column in the centre of the cell. Also, the sensor plane was not orthogonal to the beam direction during the measurements, so the column diameter of 10 μm is smeared along the x-axis. Compared to the efficiency drop in the middle between two strips (constant y), lines perpendicular to this (constant x) are barely visible since the strip surface electrode amplifies the field in that region. At the crossing of two null field lines in the midpoint between four columns the efficiency is especially low.

Finally the importance of the timing of the readout for the efficiency is considered. Accepting events within a large time interval at the pulse peak increases the statistics, however, a large number of off peak events are taken into account for which a generally lower signal has been sampled (Fig 6). If the signal is below the threshold the events are not registered as hits on the sensor leading to a reduced efficiency. Since in the LHC experiments the timing of the bunch crossing, and therefore of the event, is clocked with picosecond precision, it is always possible to measure the signal at the pulse peak and achieve the optimal efficiency with respect to time. The overall efficiency averaged over the whole sensor area, for a signal cut of 1 fC and within a time interval of 7 ns at the pulse peak, has been calculated to be (96.2 ± 0.1) % for the laterally depleted sensor at 40 V bias. This value is comparable to beta source measurements [11] with the same threshold.

The field configuration specific to the single-type column design leads to a reduced charge collection because of ballistic deficit and to a non-homogeneous detection efficiency across the detector. These problems should be overcome with the double-type column 3D design which features columnar electrodes of one type being processed from one surface of the detector and of the other type from the other side. These sensors benefit from the processing advantages of the 3D-stc design while at the same time the electrical field configuration is closer to the full 3D design. The lower efficiencies at the columns may be counteracted by tilting the columns at an angle towards the track of the impinging particle.

A production run of double-sided 3D detectors has taken place at FBK-IRST and the first double-type column 3D detectors were placed in a testbeam in summer 2008 and the analysis is progressing.

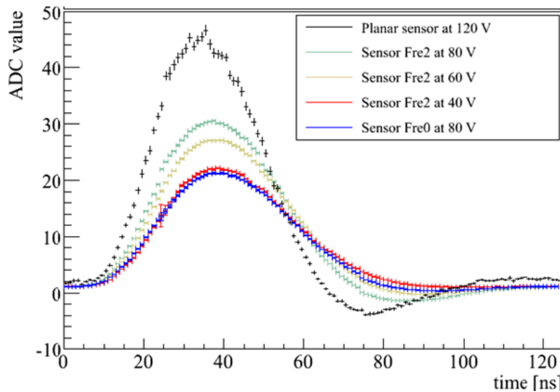

Fig 6 Collected charge of three unirradiated 3D-stc detectors measured for different bias voltages as a function of time.

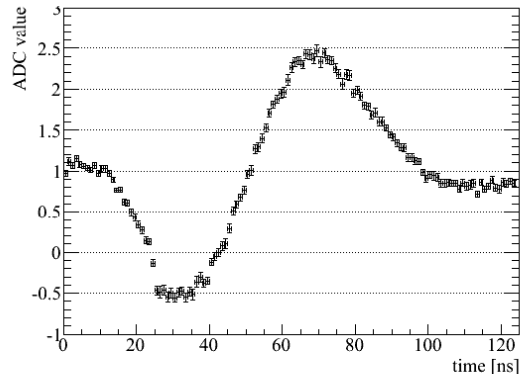

Fig 7 The average signal of the adjcent strip to the hit strip on the 3D-stc sensor, biased at 40 V, as a function of time.

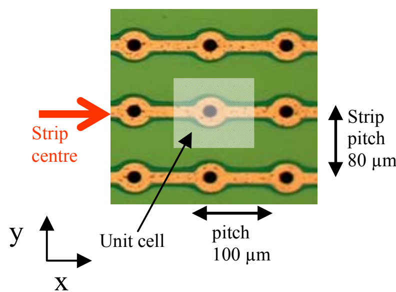

Fig 8 Diagram of the 3D-stc strip detector illustrating the unit cell.

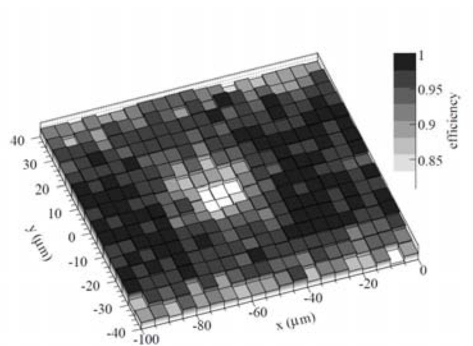

Fig 9 Two-dimensional efficiency map of the detector unit cells at 40 V bias.

6.2.2 CNM-IMB

CNM-IMB has produced two runs of “Double-Sided” 3D detector that have both n- and p-type columns, as in a full 3D detector [18], [19], illustrated in Fig 10. However, the holes of one doping type are etched from the front side of the wafer and used for readout; and the holes of the other type are etched from the back side and used for biasing, as illustrated in an SEM image of a cross-section of a real device shown in Fig 11. The double-sided processing avoids the difficulty of etching and doping the two different kinds of holes on the same side of the wafer. Furthermore, the columns do not pass through the full thickness of the substrate, which makes the devices more resistant to mechanical stress than full 3D detectors, and makes the use of a carrier wafer unnecessary, if active edges are not required. Another unique feature of the IMB-CNM-IMB process is the filling and doping process. After the columns are etched, the interior of the columns and the surface of the wafer are coated with 3 µm of polysilicon. The columns are then doped through the polysilicon, using diffusion from a solid source. On the back surface, this doped polysilicon layer remains and will connect all the bias columns together, whereas on the front surface the polysilicon must be selectively etched to separate the readout columns. Finally, the interior of the columns is passivated with silicon dioxide, using TEOS. In the first set of devices (2 wafers), the columns are 250 µm long and 10 µm in diameter, the substrate is 300 µm-thick n-type silicon, and the readout columns etched from the front surface are p-type, to avoid the need for electrode isolation. The second fabrication run consists of both n-type bulk with p-type readout (6 wafers), as before, and p-type bulk with n-type readout (8 wafers). The latter will collect electrons resulting in higher radiation tolerance and the ability to use ATLAS pixel electronics. The wafers include a verity of devices including; simple pads, short strips, Medipix2 pixel detectors and ATLAS FE-I3 pixel detectors.

The pervious status report concentrated on the simulated performance of the devices [20], [21] and [22] performed at the University of Glasgow with the finite-element simulation package ISE-TCAD. The key point is that throughout most of the device volume, where the 250 µm-long columns overlap, the electric field behaviour matches that of a full 3D detector. The double-sided structure only behaves differently around the very front and back surfaces of the detector, where the electric field becomes weaker, however full depletion is still reached at voltages lower than 10 V for typical doping concentrations. Charge deposited in these weaker-field region will be collected more slowly, and will suffer from higher charge trapping following radiation damage. After irradiation to SLHC levels (10^{16} 1 MeV n_{eq} cm^{-2}) the back surface of the sensor will not be depleted for voltages below 100 V, which will result in a loss of charge collection efficiency resulting in an active detector thickness slightly larger than the overlap region. For a typical 300 µm thick double-sided device with 250 µm deep columns (therefore 200 µm column overlap) an active thickness of 250 µm results, this is the same as a standard 3D detector.

The results presented here concentrate on the first production run as the second has only just been finished, however from initial measurements their electrical characteristics appear very similar. The results shown are divided into three sections; firstly a set electrical characterization of detectors to prove the electrical performance; secondly results from 3D detectors bumpbonded to Medipix2 pixel detectors, which have been tested with X-rays, to establish that the 3D devices can be successfully bump-bonded to readout chips and to test the detectors' performance before irradiation; finally, strip detectors connected to LHC-speed readout electronics have been irradiated and tested with MIPs to investigate their radiation hardness.

As demonstrated by simulation [20], the detector is expected to deplete in two stages. Initially, the depletion region will appear around the edge of each cylindrical readout column and grow laterally outwards with increasing bias until it reaches the adjacent bias columns. Due to the small lateral spacing between electrodes, this should only require about 2 V. At this point, most of the device volume (the 200 µm central region where the columns overlap, and the region around the surface) will be depleted. However, to deplete the region around the back surface of the device, the depletion region has to grow downwards from the tip of the readout column. In the simulation this requires a higher bias of around 8 V. Capacitance-voltage tests on a 3D pad detector test structure show this two-stage depletion behaviour [26]. The C-V curve initially drops very rapidly with bias, and then it shows a distinct kink at 2.4 V, beyond which the capacitance drops more slowly before reaching a minimum at about 9 V, as illustrated in Fig 12.

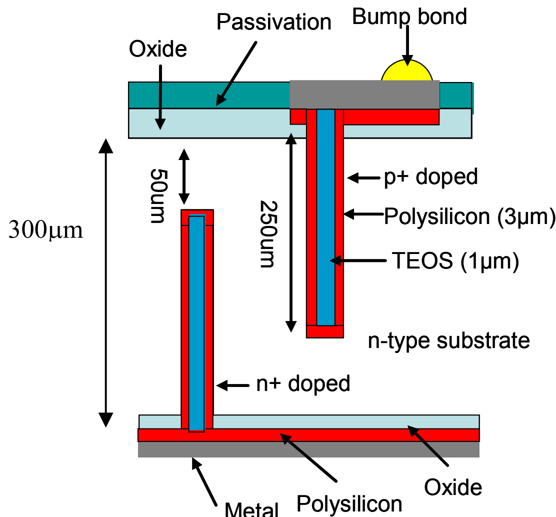

Fig 10 Diagram of the double-sided 3D structure produced at CNM-IMB.

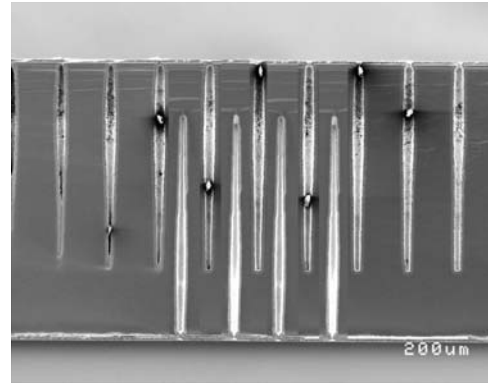

Fig 11 SEM picture of a cross section of the double-sided 3D detector showing columns etched from both sides.

The Medipix2 3D detectors consist of a 256 x 256 array of 55 µm square pixels, with a metallised pad next to each readout column which is used for bump-bonding the sensor to the readout chip, as illustrated in Fig 10. The Medipix2 chip is designed to detect X-rays, and works in a single-photon-counting mode [23], with a pair of adjustable thresholds per pixel. Three 3D detectors were bump-bonded to Medipix2 readout chips at VTT, and mounted on chipboards. These assemblies were read out using the Medipix2 USB interface [24]. As a test of the depletion behaviour, a Medipix2 3D detector was illuminated with a 60 kVp X-ray tube, and the count rate on the detector was measured as the bias was varied [25]. The results are shown in Fig 13. Since the Medipix2 detector has a relatively long peaking time, of order 100 ns [23], any ballistic deficit is expected to be small and hence the count rate should reflect the depleted volume of the device. The count rate is seen to increase extremely rapidly over the first 2 V or so, and saturates around 9 V. This is in good agreement with the simulated depletion behaviour and the measured C-V dependence, and demonstrates that the detector can operate at extremely low voltages.

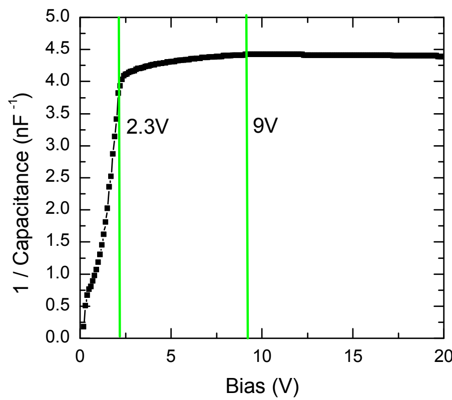

Fig 12 The capacitance voltage dependence of the double-sided 3D detector. The vertical lines mark the changes in the depletion process.

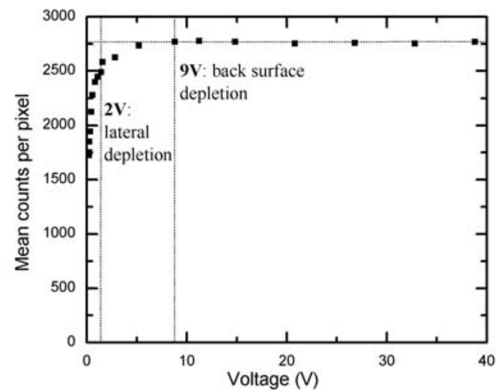

Fig 13 Count rate per pixel versus bias measured by a Medipix2 3D detector illuminated by a 60kVp X-ray tube, using a threshold energy of about 20keV. Reproduced from [25].

The Medipix2 3D detectors were tested with monochromatic X-rays on beamline B16 at Diamond Light Source [27]. The full experimental procedures and results from these tests are reported in [28]. Each hit on a Medipix2 detector is compared to a pair of thresholds, to determine whether the hit is accepted. So, an integral spectrum can be found by deactivating the upper threshold, and measuring the count rate on the detector as the lower threshold is varied, differentiating this produces the spectrum of the detector. A 3D Medipix2 detector and a standard 300 µm thick planar Medipix detector were used to make spectral measurements at Diamond with beam energies of 12, 15 and 20 keV. The beam was collimated to give a spot size smaller than the detector area. While taking the spectra, the 3D detector was biased to 22 V, and the planar detector to 100 V, to ensure that both were fully depleted. The results with the 15 keV beam are shown in Fig 14. Both detectors show a peak at the expected energy. The two detectors give very similar peak widths, indicating that their pixel noise and threshold dispersion are much the same. Both detectors also show lower-energy "hits", which occur when charge is shared between two or more pixels. It is clear that the 3D detector has substantially less charge sharing and a larger signal peak than the planar detector, despite the 3D device's lower bias voltage. When charge generated by an X-ray is shared between two pixels, then one pixel will see a hit above half the beam energy and the other will see a hit below. So, the relative numbers of charge-shared and non-charge shared photon hits can be found as indicated in Fig 14. Averaged over the tests at the three energies, 23.4% of hits on the 3D detector were shared, compared to 39.5% on the planar detector.

The Medipix2 pixel detector tests have demonstrated that these devices have extremely low operating voltages, and that the 3D structure reduces charge sharing between pixels as expected due to their internal electric field distribution. Tests of the 3D detectors bumpbonded to ATLAS pixel electronics will take place in 2009 with the new run of n-type column in p-type bulk 3D devices.

A set of 3D strip detectors with an array of p- and n-type columns with 80 µm spacing between columns of the same type which has p-type columns connected together in rows to form strips (at a pitch of 80 µm) were tested with the Beetle readout electronics and a Sr-90 beta source, as describe above for the 2007 testbeam. The strip detectors are relatively small, with 50 strips, each of which contains 50 readout columns, giving a strip length of 4mm; around the edge of the array, p-type columns are connected to form a 3D guard ring. Before connecting these devices to readout electronics, they were I-V tested, as described in [26], typical I-V characteristics gave a current of around 100 pA at 21 C and 50 V bias. Capacitance-Voltage tests performed on the strip detector showed a capacitance of 5 pF per strip; i.e. about 10 $pFcm^{-1}$. This is large compared to standard strip detectors— for example, ATLAS SCT strips are designed to have less than 2.2 $pFcm^{-1}$ capacitance. An additional AC coupled pitch adapter supplied by RD50 colleagues from the University of Helsinki was used between the detector and the front-end electronics to provide decoupling of the DC current. One of the strip detectors was irradiated to 5×10^{15} 1 MeV-n_{eq} cm^{-2}, using neutrons from the TRIGA Mark II reactor at the Jozef Stefan Institute in Ljubljana. The change in collected charge after irradiation was small and the collected charge was measured to be 12800 electrons. The spectrum, with the fit of a Landau convoluted with a Gaussian is shown in Fig 15.

The charge collected, after the above dose, from the 300 µm thick double-sided 3D detectors is comparable to previous results from the full 3D detectors fabricated at the Stanford Nanofabrication Centre, and tested at Manchester [29].

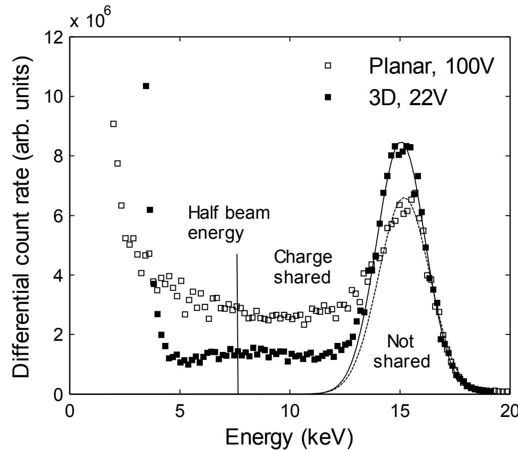

Fig 14 Spectral measurements from 3D and planar Medipix detectors tested with 15keV X-rays. Higher charge sharing can be seen on the planar detector.

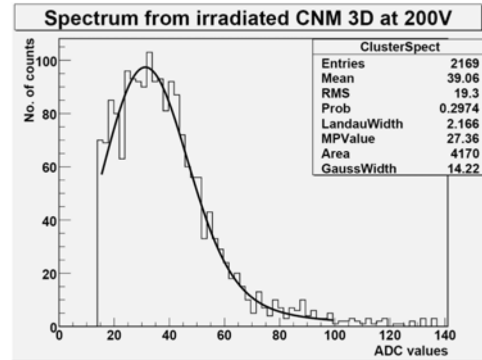

Fig 15. MIP spectrum measured from the 3D strip detector at 200V bias after irradiation to 5 x 10^{15} 1MeV-n_{eq} cm^{-2}. After calibration was applied, the most probable charge collection was found to be 12800 electrons.

6.2.3 2008 Testbeam

A second testbeam took place in the summer of 2008. This was performed by Freiburg and Glasgow with substantial assistance from the CMS collaboration, notably the Helsinki Institute of Physics. The testbeam used the CMS strip detector readout electronics, the APV25, to readout the telescope and the detectors under test. Two un-irradiated short strip double-sided 3D detectors were placed in the testbeam. One was produced at FBK-IRST and the second at CNM-IMB. The analysis of the 2008 testbeam is on going at Freiburg.

6.2.4 Development at IceMOS

The development at IceMOS was terminated during 2008 due to lack of progress at IceMOS. Initial devices were produced, which were full 3D detectors in design, which showed good electrical and capacitance performance. However the yield was very low due to some processing problems. A second batch of devices was never produced.

6.2.5 Simulation of 3D detectors at Valencia

Doubled–sided 3D detectors with a 300 µm thick p-type substrate (with a doping concentration of 7 x 10^{11} cm^{-3}) with 250 µm deep n^+ columns extending from the top of the sensor and a 250 µm p^+ column extending from the backplane were simulated using ISE-TCAD. The radius of the columns was 5 microns. The isolation method on the top surface was a p-stop ring around the n^+ column with a peak concentration of 1.18 x 10^{17} cm^{-3} which varies with depth. The isolation between n^+ columns is needed to avoid short-circuits between electrodes due to the electron inversion layer generated in the SiO_2-Si interface. The depletion voltage was simulated to be approximately 5 V. Simulations were performed to evaluate the p-stop isolation for 3 different geometries of the p-stop ring:

(a) Reference geometry: with a 10 µm internal radius for the p-stop ring.
(b) P-stop closer to n^+ column: with an internal radius of 5 µm.
(c) P-stop away from the n^+ column: the radius of the p-stop ring was 15 µm.

The ring thickness was 5 microns in all 3 cases. The simulation was only performed for an irradiation does for which the SiO_2 doping saturated with a charge concentration of 3 x 10^{12} cm^{-2} but the bulk doping concentration was almost unchanged. This is the worst case for surface isolation because at higher doses the electron inversion layer is in part compensated with the irradiation defects in the bulk.

Fig 16 shows the electric field distribution for the 3 cases described above. The highest electric field region is found for the p-stop ring away from the column. It occurs because with a wider space between the column and the p-stop ring, more potential lines fall down in the ring. A higher electric field can lead to an early breakdown. In addition, the density of electrons simulation (illustrated in Fig 17) shows for the closer p-stop ring that the p-stop is being neutralized. It is conclusive to consider the reference geometry as the best option.

A second set of simulations was performed with the optimum (reference) geometry but with the doping concentrations for the columns and the p-stop being those extracted from the simulation of the fabrication process: the n^+ column had a concentration of 1.71 x 10^{19} cm^{-3}, while for the p^+ column it was 6.01 x 10^{18} cm^{-3}. The p-stop peak concentration was 1.18 x 10^{17} cm^{-3} which varied with its depth. Charge concentration at the surface of 3 x 10^{12} cm^{-3} was modeled but no effect due to irradiation on the bulk was considered. In order to optimize the fabrication process, another two p-stop doses were also simulated: the first with half of the dose described above and the second with one order of magnitude less. The effect on the isolation is observed in the density of electrons at the detectors surface, shown in Fig 18. With the half of the dose, the n^+ columns are still isolated and this configuration shows a lower electric field than for the reference dose. However an order of magnitude less is not enough to isolate the columns.

The simulations have produced optimized p-stop geometry and doping profiles to result in the most advisable isolation structure in 3D doubled-sided p-type detector.

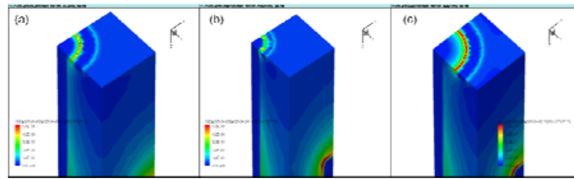

Fig 16. Electric Field Distribution (a) for the p-stop reference geometry, (b) the p-stop ring closer to the column and (c) the p-stop ring away from the column. The sensor is biased at -50 V.

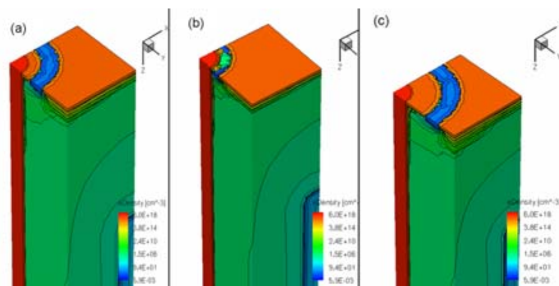

Fig 17. The density of electrons (a) for the p-stop reference geometry, (b) the p-stop ring closer to the column and (c) the p-stop ring away from the column. The sensor is biased at -50 V.

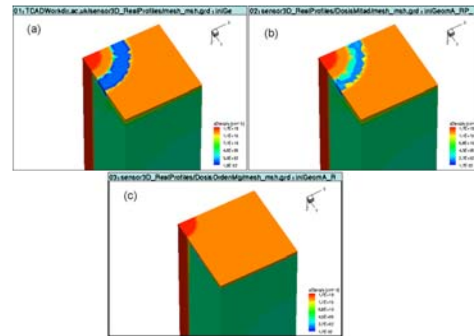

Fig 18. The density of electrons (a) with the p-stop main dose, (b) with the half of the main dose and (c) with one order of magnitude less. The sensor is biased at -50 V.

6.2.6 Modeling of 3D detectors at Ioffe

A simplified analytical model of cylindrical p-n junctions operation has been developed for 3D detectors at Ioffe [30]. In this model different configurations of 3D detectors are considered as the combinations of two elements: the p-n junction and the ohmic columns. This allows 3D detector constructions can be classified by the following features:

- the type of the column: J - junction type (p-n junction), or O - ohmic type (n^+-n or p^+-p contacts);
- the side of the wafer, front or back, which the columns of a specific type reach;
- the treatment of the backside: Osurf - ohmic surface, or SiO_2 - insulating surface passivated by SiO_2;
- the depth of the columns: columns that run through the entire depth of the wafer, or columns which terminate before reaching the other side of the wafer.

The sketches of the possible 3D detector configurations are presented in Fig 19 along with the corresponding abbreviations. For example, J&O/Osurf means that the junction and ohmic columns start from the front wafer surface while the ohmic contact covers the entire back side of the detector.

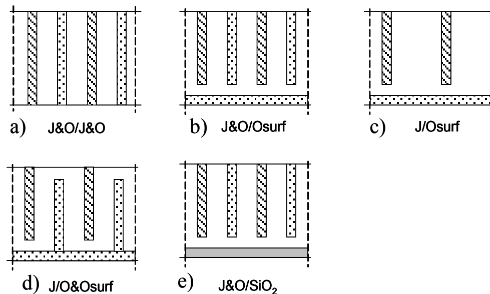

Fig 19. Possible configurations of 3D detectors. The oblique pattern shows a junction pore, the dotted pattern corresponds to an ohmic pore.

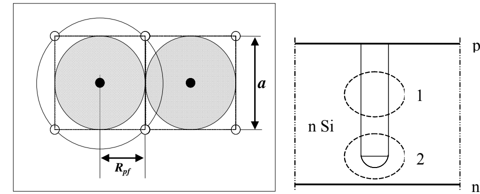

Fig 20. Two neighboring cells of the 3D detector (left) with each junction pore surrounded by four ohmic columns. The elements of the detector junction pore (right): 1- cylindrical, 2 - the pore dead tip region.

In the model two distinct sections of the p-n junction column are recognized: a cylindrical part of the column (1) and a semi-spherical tip (2). Two neighboring cells in the structure are depicted in Fig 20. Each cell includes a junction column (J) surrounded by four ohmic columns (O), and the parameter a is the pitch of the 2D surface array. Space charge regions (shown in Fig 20 as grey circles) extend around the columns and their radii increase with applied bias. The shown state between the neighboring space charge regions is a pinch-off.

The operational characteristics of 3D detectors which are important for 3D detector engineering are the pinch-off bias voltage V_{pf}, the full depletion voltage V_{fd}, and the maximal operational bias voltage V_{op}. The latter parameter is defined as a breakdown voltage for the gap between the tip of the junction column and the detector back side contact.

Solving the Poisson equation allows these parameters to be calculated for 3D detectors that match the design of ATLAS inner tracker silicon strip detectors with a junction column pitch of 80 μm ($R_{pf} = a/2 = 40$ μm). The radius of the cylindrical p-n junction column is 5 μm, and the structure has been processed on n-type silicon with N_{eff} of 4 x 10^{12} cm^{-3}. This resistivty corresponds to that of the Magnetic Czochralski n-type Si which is considered to be optimal for radiation hard detectors. The results give a pinch-off voltage, V_{pt}, of 7.7 V and a full depletion voltage, V_{fd}, of 18.3 V ($R_{fd} = 0.7a$ = 56 μm).

The maximal operational voltage of 3D detectors is limited by the breakdown which occurs in the points with a maximal electric field. Here the factors related to the design of the area surrounding the column end at the surface are neglected because this element of the detector is usually constructed

using a knowledge on planar junctions developed for operation up to a certain voltage range. Therefore a specific element of 3D detectors which can initiate the breakdown and limit the maximal operational bias range is the tip of the column that does not reach the surface. A spherical tip is considered as the optimal shape to minimize the electric field due to the focusing effect.

The breakdown of abrupt p-n junctions for cylindrical and spherical geometries was considered in [31], and it was shown that the breakdown voltage V_{br} can be defined in terms of the breakdown parameters for the planar junction and the ratio of the radius of the border of the p^+ region, r_0, to the radius of the depleted region, R_d. For standard 3D detectors processed on high resistivity silicon (resistivity ρ of 1-10 kΩcm and N_{eff} of 4 x 10^{11} cm^{-3} to 4 x 10^{12} cm^{-3}, respectively), the breakdown voltage is very high and out of the range of the operational voltage. Even when the breakdown voltage is reduced, by decreasing the column radius to 1 µm, the detector can still operate with a bias of 1000 V.

Irradiation of 3D detector (ATLAS design) will lead to dramatic changes in the operational parameters. Using the introduction rate β of the effective space charge concentration under neutron irradiation whose value has been determined to be 0.017 cm^{-1} by numerous studies on Si planar detectors, it is possible to calculate that if a detector is irradiated to a fluence of 1 x 10^{16} 1MeV n_{eq} cm^{-2}, which is the goal for SLHC Pixel upgrade, the specific parameters of this irradiated detector will be given by: N_{eff} = 1.7 x 10^{14} cm^{-3}, V_{pt} = 320 V and V_{fd} = 770 V. The maximal operational voltage related to the detector cylindrical column was calculated to be only 330 V, a value that is close to V_{pf}. The restriction for the operational voltage range evaluated for a spherical tip is even stricter and gives a breakdown voltage of 250 V, a value that is lower than V_{pf}.

Using this proposed systemization, it is possible to consider the potential of the different 3D detector constructions shown in Fig 19. The J&O/J&O construction (Fig 19 a) is the most predictable and the most suitable for operation in a harsh radiation environment because it provides a cylindrically symmetric electric field both before and after irradiation. This construction is free from the electric field focusing effect and is optimal for charge collection. Unfortunately, its construction is complicated since it requires double-sided fabrication technology. This brief analysis shows that a compromise between the operational properties of 3D detectors and their technology can be found in the J/O&Osurf design, which is the structure fabricated by CNM-IMB and FBK-IRST. Further study will concentrate on the comparison between the results of these calculations and the experimental characteristics of 3D detectors. Research optimizing of the design is planned by the joint activities of the Ioffe Institute and CNM-IMB.

6.3 References

[1] RD50 Status report 2006, CERN-LHCC-2007-005

[2] E. Fretwurst et al., Nucl. Instr. and Meth. A 552, Issues 1-2, 21 October 2005, Pages 7-19 "Proceedings of the 5th International Conference on Radiation Effects on Semiconductor Materials, Detectors and Devices"

[3] L. Andricek et al., IEEE Trans. Nucl. Sci. NS-51 (3) (2004) 1117.

[4] R. Richter et al., Nucl. Instr. And Meth. A 377, (1996), 412

[5] Ma and Dressendorfer, "Ionizing radiation in MOS devices and circuits", Wiley, New York, 1989.

[6] H. Sadrozinski et al., Nucl. Instr. And Meth. A 579 (2007), 769.

[7] C. Piemonte et. al., "Development of 3D detectors featuring columnar electrodes of the same doping type", Nuclear Instrum. Methods. A 541 (2005), 441.

[8] C. Piemonte et. al., Study of the signal formation in single-type-column 3D silicon detectors, Nuclear Instrum. Methods. A 579 (633) 2007

[9] S. Ronchin et. al., Fabrication of 3D detectors featuring columnar electrodes of the same doping type, Nuclear Instrum. Methods. A 573 (224) 2007

[10] RD50 Status report 2007, CERN-LHCC-2008-001.

[11] S. Kühn, G.-F. Dalla Betta, S. Eckert, K. Jakobs, U. Parzefall, A. Zoboli and N. Zorzi, "Short strips for the sLHC: a p-type silicon microstrip detector in 3D-technology", IEEE Trans. Nucl. Sci., vol. 55, no. 6, (2008).
[12] U. Parzefall, "3D detectors at PSD8", Nuclear Instrum. Methods. A need to check details
[13] G. Pahn, R. Bates, M. Boscardin, G.-F. Dalla Betta, S. Eckert, L. Eklund, C. Fleta, K. Jakobs, M. Köhler, S. Kühn, C. Parkes, U. Parzefall, D. Pennicard, T. Szumlak, A. Zoboli, N. Zorzi, "First beam test characterization of a 3D-stc silicon short strip detector", IEEE Trans. Nucl. Sci., to be published
[14] S. Loechner and M. Schmelling, The Beetle Reference Manual - chip version 1.3, 1.4 and 1.5, LHCb-2005-105.
[15] A. A. Alves et al., The LHCb Detector at the LHC, JINST **3** (2008) S08005.
[16] J. Treis et al., A modular PC based silicon microstrip beam telescope with high speed data acquisition, Nucl. Instrum. Methods A, vol. 490, pp. 116-127, 2002.
[17] S. Eckert et al., Short p-type silicon microstrip detectors in 3D-stc technology, Nucl. Instrum. Methods A, vol. 596, pp. 53-57, 2008.
[18] G. Pellegrini, F. Campabadal, M. Lozano, J.M. Rafi, M. Ullan, R. Bates, C. Fleta and D. Pennicard, "Double sided 3D detector technologies at CNM-IMB", Nuclear Science Symposium Conference Record, 2006. IEEE , vol. 2, pp. 1248–1252, Oct. 29 2006-Nov. 1 2006.
[19] G. Pellegrini, M. Lozano, M. Ullan, R. Bates, C. Fleta, D. Pennicard,"First double-sided 3-D detectors fabricated at CNM-IMB", Nucl. Instr.and Meth. A 592 (1–2) (2008) 38–43.
[20] D. Pennicard, G. Pellegrini, M. Lozano, R. Bates, C. Parkes, V. O'Shea and V. Wright, "Simulation results from double-sided 3-D detectors", IEEE Trans. Nucl. Sci., vol. 54, no. 4, pp.1435-1443, Aug. 2007.
[21] D. Pennicard, "Simulation results from double-sided and standard 3D detectors", 10th RD50 Workshop, Vilnius (Lithuania), 3–6 June 2007, available online at http://rd50.web.cern.ch/rd50/
[22] D. Pennicard, "Simulations of 3D detectors with radiation damage up to 10^{16} n_{eq}/cm^2", ATLAS 3D Sensors R&D meeting, CERN, 2 July 2007, available online at http://indico.cern.ch/conferenceDisplay.py?confId=17797
[23] X. Llopart, M. Campbell, R. Dinapoli, D. S. Segundo, E. Pernigotti, "Medipix2: A 64-k pixel readout chip with 55 µm square elements working in single photon counting mode", IEEE Trans. Nucl. Sci. 49 (5) (2002) 2279–2283.
[24] Z. Vykydal, J. Jakubek, S. Pospisil, "USB interface for Medipix2 pixel device enabling energy and position-sensitive detection of heavy charged particles", Nucl. Instr. and Meth. A 563 (1) (2006) 112–115.
[25] C. Fleta, D. Pennicard, R. Bates, V. O'Shea, C. Parkes, M. Lozano, G. Pellegrini, J. Marchal, and N. Tartoni, "X-ray detection with 3D Medipix2 devices", IWORID 2008 Conference Record. Submitted to Nucl. Instr. and Meth. A.
[26] D. Pennicard, G. Pellegrini, M. Lozano, C. Fleta, R. Bates, C. Parkes, "Design, simulation, production and initial characterisation of 3D silicon detectors," Nucl. Instr. and Meth. A, In Press, Corrected Proof, doi:10.1016/j.nima.2008.08.077
[27] Diamond Light Source, "B16 beamline plan", available at http://www.diamond.ac.uk/Beamlines/Beamlineplan/B16/default.htm, 2008.
[28] D. Pennicard, J. Marchal, C. Fleta, G. Pellegrini, M. Lozano, C. Parkes et al., "Synchrotron tests of a 3D medipix2 X-ray detector", submitted to Journal of Synchrotron Radiation, 2008.
[29] C. D. Via, E. Bolle, K. Einsweiler, M. Garcia-Sciveres, J. Hasi, C. Kenney et al., "3D active edge silicon sensors with different electrode configurations: Radiation hardness and noise performance", IEEE NSS Conference Record, Honolulu 2007
[30] V. Eremin, E.Verbitskaya, Analytical Approach for 3D Detectors Engineering, pres. at 2008 NSS-MIC, Oct 19-25, 2008, Dresden; NSS-MIC Conference Records (in press).
[31] S. M. Sze, Physics of semiconductor devices, second ed., Wiley, New York, 1981, pp. 99-108.

[32] T. Gronlund, Z. Li, G. Carini, M. Li, Full 3D simulations of BNL one-sided silicon 3D detectors and comparisons with other types of 3D detectors, Nucl. Instrum. and Meth. A 586 (2008) 180-189.

7 Full detector systems

The last two RD50 workshops (referenced below) have seen significant results reported by institutes involved in the full detector system research line. They have been reports on instruments available to the RD50 community, namely the beam test facility at the CERN H2 area and the ALIBAVA system for characterising the charge collection efficiency of silicon microstrip detectors with a system built around the 40MHz Beetle analogue chip. The system is fully commissioned and is suitable for taking data on highly irradiated detectors (Figure 2) [13]. The beam test facility uses a reference beam telescope and an efficient cooling system to provide precise impact points to the device under test (DUT) and efficient cooling (Figure 1). Data taken with several irradiated sensors have been shown [1, 5, 6].

Future pixel activities have been announced [8] and first results with planar pixels presented [9][10].

Several results of charge collection efficiency after very high doses of proton and neutron irradiations have been shown, bringing the CCE measurements with segmented planar silicon detectors over the remarkable limit of ~$2x10^{16}$ n_{eq} cm^{-2} [2, 3, 4, 11].

Also, important parameters to qualify the performances of irradiated detectors, like interstrip capacitance and resistance after irradiation have been measured and reported. These parameters are important for the radiation harder n-side readout detectors in order to determine if the inter-electrode isolation (whether p-spray, p-stop or a combination of the two) is sufficient to guarantee proper operations of the segmented detectors.

Extensive studies of n and p-type detectors processed on both FZ and MCz wafers have been reported. It has been shown that remarkable results have been obtained with n-side readout nMCz microstrip sensors, though further irradiations are required to demonstrate this advantage after much higher doses (the present higher dose investigated with segmented nMCz detectors is $1x10^{15}$ n_{eq} cm^{-2}.

Also the effect of thinning the detector down to 140mm has been further investigated. It has been shown [3] that the thinner sensors start to exhibit a significant advantage with respect to the thstandard thickness for doses above $1x10^{16}$ n_{eq} cm^{-2}.

7.1 A few selected results

Among many valuable results, here are reported a few highlights.

Figure 3 shows the correlation between the full depletion voltage (V_{FD}) measured with the C-V and with the charge collection methods [2]. A clear correlation is found, implying that the measurements of V_{FD} by C_V is a good indication of the expected charge collection (excluding trapping effects). The comparison has been performed after neutron irradiation doses up to $1x10^{15}$ n_{eq} cm^{-2}. A very good correlation is demonstrated

On the other hand, it has also been shown that the linear extrapolation to very high doses of parameters measured at more moderate fluences can lead sometimes to wrong estimates. Figure 4 shows, as an example, the expectations on the reverse current after very high doses of neutron irradiations and the actual measured values [13]. A lower reverse current, with respect to the expectations from the accepted parameterisation, is measured.

Also the collected charge is different from what expected by the direct measurement of the charge trapping probability. Figure 5 shows the charge collected at various bias voltages as a function of the n_{eq} dose (up to $3x10^{15}$ n_{eq} cm^{-2}) by n-in-p microstrip sensors irradiated with reactor neutrons. It can be noticed that the entire (or sometimes more) charge ionised by a mip is recovered if high enough bias can be applied to the sensors. A surprisingly high charge is collected also after very high doses of hadron irradiation (Figure 6 and 7). It can be noticed that the substantial amount of charge collected by planar detectors well justifies their use also for the pixel layers of the upgraded experiments in the SLHC. This consideration has supported the start of a more consistent pixel activity within RD50.

References

The following references are from the 12th RD50 - Workshop on Radiation hard semiconductor devices for very high luminosity colliders, Ljubljana, Slovenia, 2-4 June 2008. The agenda and the talks can be found at: http://rd50.web.cern.ch/rd50/12th-workshop/default.htm

[1] *Irradiated MCz sensors for a testbeam, presented* by Martin Frey
[2] *Charge collection measurements on MICRON RD50 strip detectors and diodes irradiated with protons, pions and neutrons* presented by Gregor Kramberger
[3] *New CCE results with microstrip detectors made on various substrates* presented by Gianluigi Casse
[4] *Measurement of charge collection in p-type microstrip sensors with SCT128 chip* presented by Igor Mandic

The following references are from the 13th RD50 - Workshop on Radiation hard semiconductor devices for very high luminosity colliders, CERN, Slovenia,10-12 November 2008. The agenda and the talks can be found at: http://indico.cern.ch/conferenceDisplay.py?confId=42494

[5] *Test beam results of heavily irradiated magnetic Czochralski silicon (MCz-Si) strip detectors* presented by Panja-Riina Luukka
[6] *Status of the ALIBAVA readout system* presented by Ricardo Marco
[7] *X-Ray irradiation on p-type micro-strip detectors with p-spray and moderated p-spray isolations* presented by Michael Beimforde
[8] *Production of n-in-n and n-in-p pixels on Fz and MCz silicon with CiS* presented by Anna Macchiolo
[9] *Pixel Sensor Measurements at CERN* presented by Heinz Pernegger
[10] *Signal height in irradiated Silicon Pixel Detectors* presented by John Acosta
[11] *Measurements of CCE/IV/annealing behaviour of microstrip detectors irradiated with reactor neutrons and protons to SLHC doses* presented by Anthony Affolder
[12] *Questions about extrapolation at SLHC doses of silicon parameter measured after lower fluences* presented by Gianluigi Casse
[13] Communication from Mercedes Miñano.

Several of these results have also been shown in several international conferences on detectors and instrumentations.

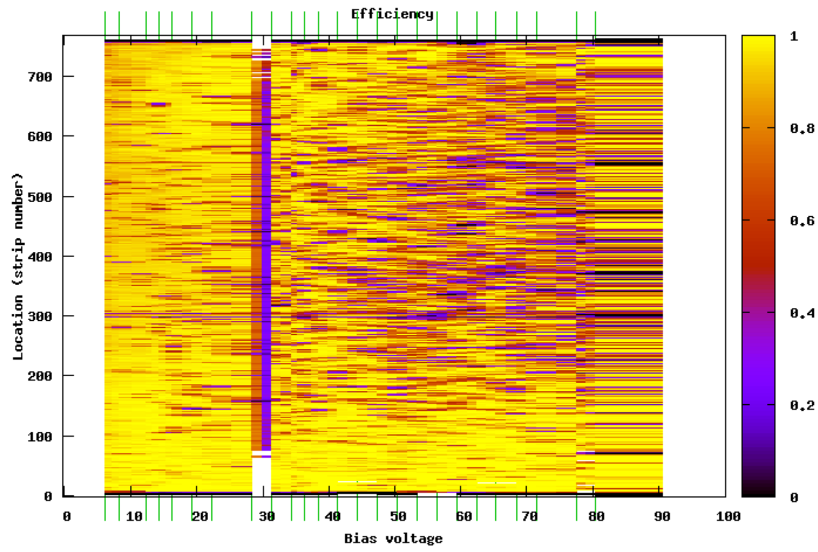

Figure 1. Efficiency of the non-irradiated Fz-Si detector as a function of operation voltage and strip number [5].

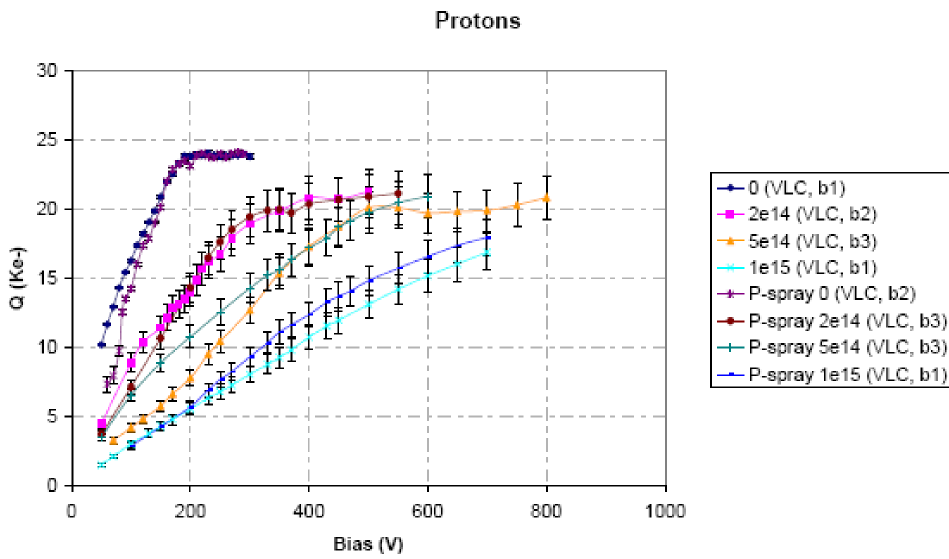

Figure 2. Collected charge as a function of the bias voltage for proton irradiated sensors measured with the ALIBAVA system [13].

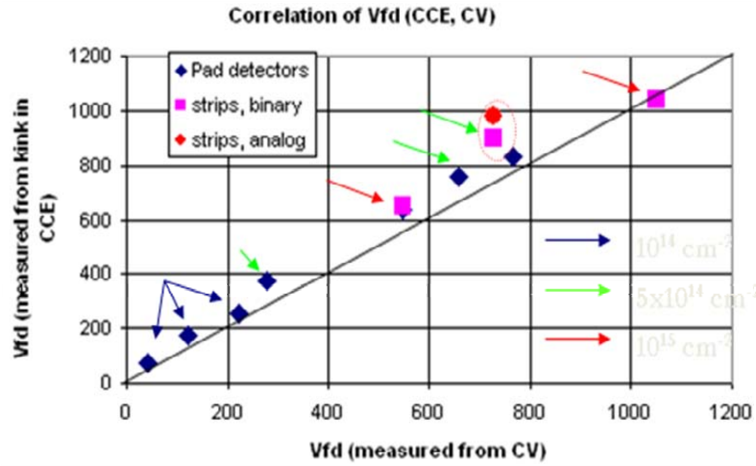

Figure 3. Correlation between the VFD measured with the CCE and the C-V methods with diodes irradiated up to 3×10^{15} neutron cm^{-2} [2].

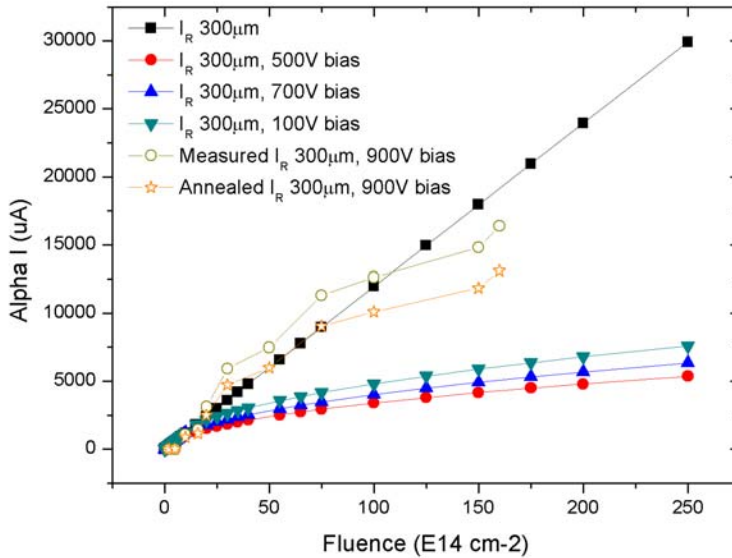

Figure 4. Reverse current as a function of fluence for irradiated p-type sensors, up to very high doses. The figure shows the difference between the expected and the measured values [12].

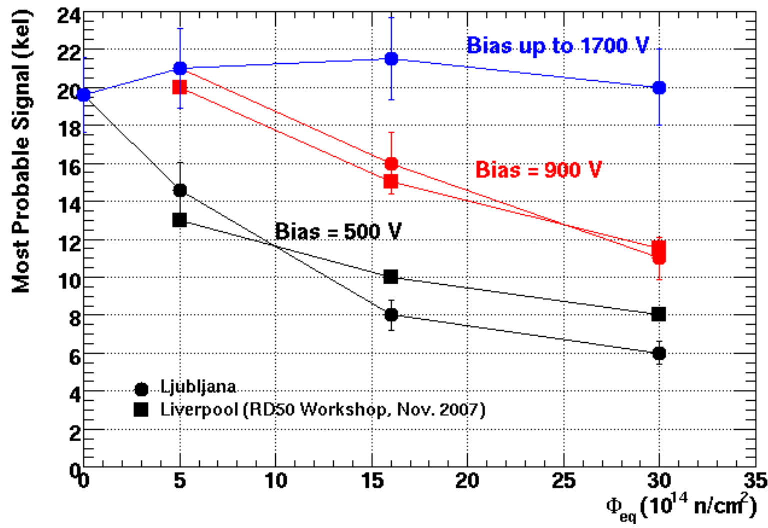

Figure 5. Charge collected at various bias voltages with p-type silicon microstrip detectors irradiated with neutrons (up to $3x10^{15}$ n_{eq} cm^{-2}) [4].

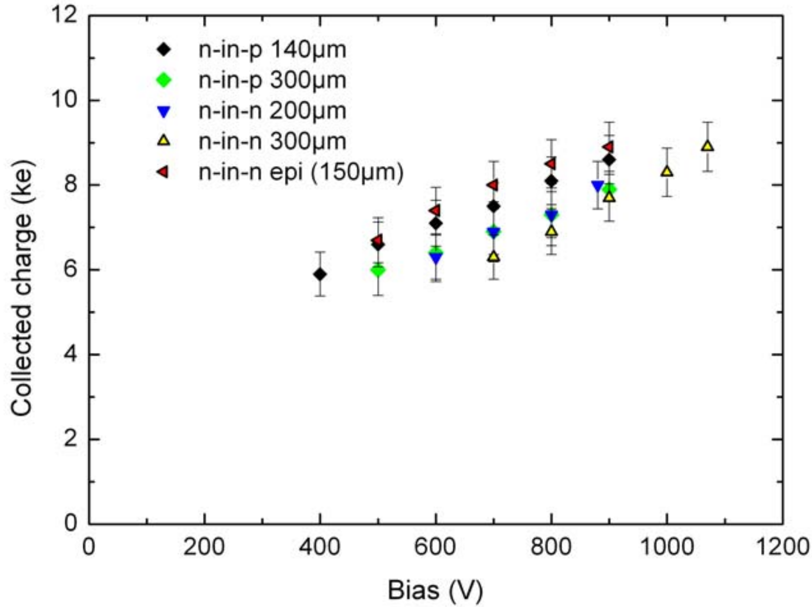

Figure 6. Collected charge as a function of the bias voltage (CC(V)) for various detectors irradiated with neutrons to $1x10^{16}$ n_{eq} cm^{-2} [3].

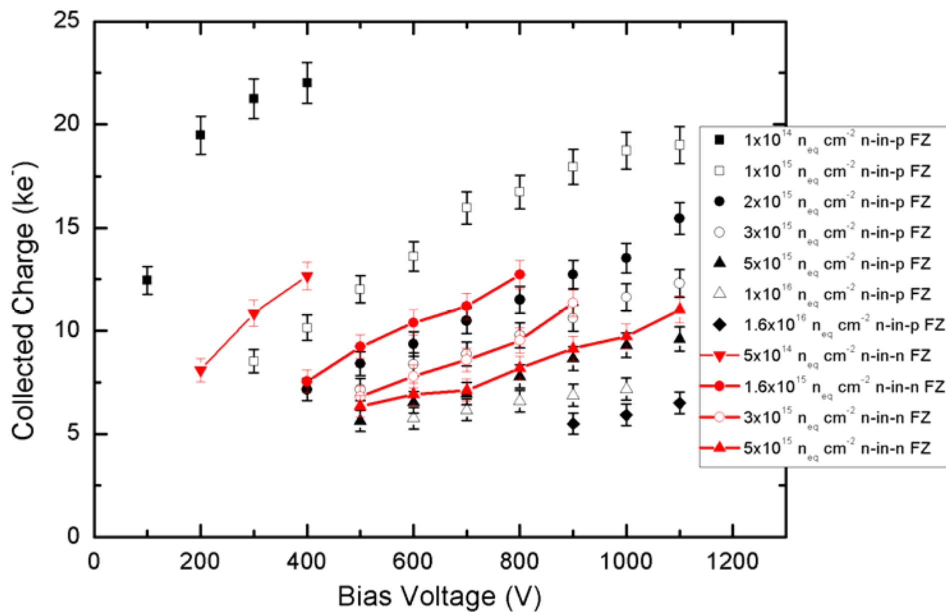

Figure 7. Collected charge as a function of the bias voltage (CC(V)) for p-type detectors irradiated with protons to various fluences up to 1.6×10^{16} n_{eq} cm^{-2} [11].

8 Resources

All participating institutes organize their own resources required for the research activities in their home laboratories. Integration in a CERN approved R&D project allows them to apply for national funding in terms of financial and manpower resources. The collaboration comprises several institutes, which have access to irradiation sources (reactors and accelerators, see [1]), as well as clean room and sensor processing facilities. A very wide range of highly specialized equipment for characterization of sensors and materials is also available (see [2]).

8.1 Common Fund

RD50 has a Common Fund to which each institute contributes every year a certain amount. The Common Fund is used for project related investments, like processing of common test structures or purchasing of special material and equipment. Furthermore it is used to cover the organization of collaboration workshops, common irradiation runs, or other specific activities of common interest.

8.2 Lab space at CERN

The RD50 collaboration was temporarily using existing infrastructure and equipment at CERN in 2008 and requests to continue to do so in 2009. As a member of the collaboration, the group PH-DT can provide access to available lab space in building 14 (characterization of irradiated detectors), in building 28 (lab space for general work) and in the PH Departmental Silicon Facility (hall 186, clean space). The collaboration would like to keep the RD50 visitor office in barrack 591 and use the CERN infrastructure to organize one workshop at CERN in 2009.

8.3 Technical support at CERN

A low level of support from PH-DT (wire bonding and sensor mounting) may be profitable. The expected work volume for 2009 is estimated to be very limited.

8.4 Support of the CERN RD50 members

It is requested that the RD50 members affiliated to CERN are further financially supported in their research activities through the CERN PH Department. The corresponding activities shall be coordinated by the PH-DT group assuring a balanced research program following on the one hand the RD50 research strategy and on the other hand the research interests of all LHC experiments towards radiation tolerant silicon detector upgrades for the SLHC.

For 2008/2009 the RD50 collaboration highly acknowledges the funding and support received through the PH Department work package WP4 “Radiation Hard Semiconductor Detectors” of the “CERN DG-Whitepaper project”.

[1] An extensive list of irradiation facilities open to RD50 can be found on the RD50 web page: http://www.cern.ch/rd50/

[2] R&D Proposal - DEVELOPMENT OF RADIATION HARD SEMICONDUCTORDEVICES FOR VERY HIGH LUMINOSITY COLLIDERS, LHCC 2002-003 / P6, 15.2.2002.